



Every Ray Counts!

*Enabling large-scale solar PV integration
by smart-grid applications combining
fine-resolution meteorology and grid
management*

Frank P.M. Kreuvel

Propositions

1. The clouds silver linings are too often overlooked; in life as well as when integrating solar energy into the electricity grid.
(this thesis)
2. Forecasting irradiance variability is required for large-scale solar energy integration by grid balancing.
(this thesis)
3. Research grants should be based on enthusiasm of the principal investigator.
4. Deep learning too often is an excuse for shallow understanding.
5. Making data on the electricity grid publicly available should be a top priority for grid operators.
6. Businesses should start projects with a review of the state-of-the-art instead of rushing a proof-of-concept.
7. Net-metering of solar energy has evolved from a necessary push in the right direction to a hinderance for large-scale solar energy integration.

Propositions belonging to the thesis, entitled

Every Ray Counts!

Enabling large-scale solar PV integration by smart-grid applications combining fine-resolution meteorology and grid management

Frank Kreuwel

Wageningen, 11 April 2023

Every Ray Counts!

Enabling large-scale solar PV integration by smart-grid applications combining fine-resolution meteorology and grid management

Frank P.M. Kreuwel

Thesis committee

Promotors

Dr C.C. van Heerwaarden
Assistant professor, Meteorology and Air Quality
Wageningen University & Research

Prof. Dr J. Vilà-Guerau de Arellano
Professor of Meteorology and Air Quality
Wageningen University & Research

Other members

Prof. Dr J. Kleissl, UC San Diego, USA
Prof. Dr M. Gibescu, University Utrecht
Dr A. ter Heijne, Wageningen University & Research
Dr J.F. Meirink, Royal Dutch Meteorological Institute, De Bilt

This research was conducted under the auspices of the Graduate School for Socio-Economic and Natural Sciences of the Environment (SENSE)

Every Ray Counts!

Enabling large-scale solar PV integration by smart-grid applications combining fine-resolution meteorology and grid management

Frank P.M. Kreuwel

Thesis

submitted in fulfilment of the requirements for the degree of doctor
at Wageningen University
by the authority of the Rector Magnificus
Prof. Dr A.P.J. Mol,
in the presence of the
Thesis Committee appointed by the Academic Board
to be defended in public
on Tuesday 11 April 2023
at 4 p.m. in the Omnia Auditorium.

Frank P.M. Kreuwel

Every Ray Counts!

Enabling large-scale solar PV integration by smart-grid applications combining fine-resolution meteorology and grid management

162 pages.

PhD thesis, Wageningen University, Wageningen, the Netherlands (2023)

With references, with summary in English

ISBN: 978-94-6447-521-0

DOI: <https://doi.org/10.18174/582807>

Summary

Solar energy, produced by photovoltaic (PV) systems, is a crucial resource in the transition towards a renewable-based society. The number of solar panels is rapidly increasing, driven both by commercial parties installing solar parks as well as homeowners placing them on their roofs. The energy produced by PV systems must be transported by the electricity grid. Since the lifespan of an electricity cable can exceed 80 years, much of the grid was installed long before the rise of solar energy and was not designed to cope with large-scale, decentralized feed-in of energy. This results in congestion and voltage problems on the grid and restricts the installation of new PV systems. Balancing local energy generation and consumption by system operators is a promising pathway to accommodate higher penetration levels of PV on the existing grid. This entails grid operators to predict on a daily basis where issues are going to occur, and take mitigating actions before that happens, such as curtailment of renewable generation or redispatch via market platforms. This active balancing of supply and demand is often referred to as a 'smart grid'. However, making use of smart grid technologies effectively requires two things. First, a detailed understanding of how solar irradiance, PV generation and grid issues are connected. Second, it requires forecasts of solar generation on high spatial and temporal resolution, which are accurate enough to ensure grid safety.

Inspired by this timely challenge, the central aim of this thesis is to enable optimal integration of solar energy into the electricity grid by smart-grid technologies. This is tackled in three stages. First, high-resolution datasets are combined and analysed in detail to better understand irradiance-induced grid issues. Second, weather predictions are tailored to forecast the level of detail required to foresee these grid

Summary

issues. And finally, these forecasts are applied in an operational setting to balance the grid in an in-situ case study. In connecting these three aspects, this PhD thesis aims to bridge the fields of high-resolution meteorology and solar photovoltaic grid integration. To tackle these objectives, the joint expertise of experts on meteorology and grid management is necessary. Therefore, this project was initiated as a collaboration between the Meteorology and Air Quality (MAQ) department of the Wageningen University and Research and the System Operations department of network operator Alliander N.V. During the project, I was actively involved in the radiation group of MAQ, while simultaneously being the lead of the Short Term Forecasting team of grid operator Alliander, allowing experts from both fields to contribute to the interdisciplinary challenges discussed in this work.

Chapter 3 analyses the variability and commonly observable extremes of irradiance and PV generation on timescales from seconds to hours. The high-frequency variability of PV generation is expected to be a main source of PV-induced issues on the grid. These fluctuations in PV generation are induced by fluctuations in irradiance, namely passage of clouds, openings in cloud decks and variations in the cloud optical depth. From a research perspective, irradiance has been studied in much more detail than generated solar energy. Therefore, this thesis starts by performing a detailed analysis to quantify PV fluctuations and their commonly observable extremes and relate them to those of irradiance. This analysis combines three datasets, originating from a pyranometer, two household-scale PV systems and a SME-scale PV system. These datasets are provided by the KNMI, Utrecht University and Alliander, respectively. It is confirmed that clouds can lead to *increased* irradiance. Surprisingly, we find that peaks in PV generation even exceed peaks in irradiance and can exceed typically used values in grid design by over 20%. We show that to accurately represent the worst-case conditions in terms of PV integration, a temporal resolution of irradiance in the order of seconds is required.

Chapter 4 presents a first-ever, smart meter based investigation of PV-induced voltage problems in the electricity grid. Traditionally concerning the low-voltage grid, operators considered themselves *blind but happy*; very few measurements are available, but the grids capacity is always more than enough (jargon: a *copper plate*). However, the rapid rise of rooftop-based PV systems is quickly turning this into *blind and unhappy*. A growing number of customers acts as a sensor of a PV induced problem, from which a measurement value is obtained when they call to file a complaint. Per 2015 (from a grid operator point of view: recently), a large-scale roll out of advanced metering infrastructure has begun (also known as the smart meter).

This allows a vast number of measurements related to grid quality to be obtained. **Chapter 4** presents on how this novel data source can help to shed light on PV induced grid issues. Spanning a 6-month period, more than 200.000 overvoltage events were gathered. These events are combined with ground-based irradiance measurements, satellite observations and power measurements at the substation to understand their occurrence. A sharp increase in event occurrence is observed in spring. Moreover, our findings indicate that the PV hosting capacity of the grid is reached throughout the service area of the grid operator simultaneously. We show that a combination of high PV generation and low energy consumption is a driver of PV-induced issues. This results in overvoltage occurrence on Sundays (not to be confused with sunny days), where energy consumption is low, to be more than double of that on weekdays.

Chapter 5 details a machine learning (ML) framework to forecast irradiance at a 1-minute resolution at a day-ahead lead-time in terms of its probability density function (PDF). State-of-the-art, operationally available, Numerical Weather Prediction (NWP) models provide irradiance forecasts at an hourly resolution. Chapters 3 and 4 highlight the importance of fluctuations at much shorter timescales (seconds to minutes). This chapter sets out to bridge what is currently available from the weather models and what is required for PV integration. This is achieved by post-processing hourly output from KNMI's Harmonie NWP model using supervised learning. A year of 1-minute resolution irradiance observations from 18 KNMI stations is used to train the forecasting model. We show that this method can predict key statistics of 1-minute irradiance. Moreover, results show that the same framework can be used to enrich global-scale reanalysis datasets. Finally, the results of this ML methodology are compared to the next generation of weather models based on Large Eddy Simulation (LES), on a case study of 4 days, with a horizontal grid spacing of 75 meters. Typically, the presence in clouds can only reduce irradiance in NWP and LES models. In reality however, cloud enhancement can cause irradiance to exceed radiation under clear-sky conditions. Since moments of high irradiance are particularly important for grid operators, being able to forecasts to occurrence of such moments is key. This chapter presents the methodology to achieve this under operationally acceptable computing requirements and shows the generalizability of its performance.

Chapter 6 evaluates a year-long case study of operational congestion management on a city area scale, where congestion occurs when there is an excess of solar generation. An open-source machine learning framework is provided to

Summary

systematically analyse the predictability of load on a contingency. Grid operators have only recently started to apply day-ahead congestion management to locally balance the grid. While accurate forecasts of the net-load are required to stay cost-effective and ensure grid-safety, the operational achievability of this accuracy must be proven. The net-load in this case study is a combination of energy consumption (primarily households and small, medium businesses) and solar- and wind generation. This ML framework is applied to attribute of inaccuracies in the net-load forecast to errors in the forecasted weather parameters related to wind- and solar energy generation. Overall, the largest part of the errors in the net-load forecast can be attributed to errors in the wind forecast. However, we show that when the load approaches the grid safety limits, errors in the solar forecasts have the biggest impact on the accuracy of the net-load forecast.

The results of this thesis, as summarized in **Chapter 7**, contribute to connecting the fields of meteorology and grid management. Specifically high-resolution irradiance forecasting and integration of solar PV by active grid balancing. These findings have led the grid operator involved in this work to adapt their worst-case scenarios of PV generation to include extreme values found under broken-cloud conditions. Moreover, a predictability analysis using the framework detailed in this work is performed for areas where congestion management is considered. Moving forward, we recognize the growing importance of weather forecasts in facilitating the energy transition. To bridge the temporal gap towards the next generation of high-resolution, cloud-resolving weather models, we suggest the providers of weather forecasts to include post-processed results in a comparable way to the current model output, using proven models from the academic forecasting community. Most importantly, we recommend formulating joint projects between the fields of meteorology and grid management, to facilitate the collaboration between experts of these fields, which is desperately required for an efficient transition to a renewable-based society.

Contents

1	Introduction	1
2	Integrating Disciplines	9
3	Analysis of high frequency photovoltaic solar energy fluctuations	17
4	Characterizing solar PV Grid Overvoltages by data blending Advanced Metering Infrastructure with Meteorology	37
5	Forecasting day-ahead 1-minute irradiance variability from Numerical Weather Predictions	59
6	Inaccuracy of Meteorological Forecasts in relation to Day-Ahead Congestion Management in the Distribution System	97
7	Conclusions and perspectives	117
8	Appendix	125

Chapter 1

Introduction

1.1 Motivation

Solar energy produced by photovoltaic (PV) systems is steadily growing in importance, with yearly yields increasing by 20% in 2021 (International Energy Agency, 2022). Two of the major challenges in large-scale deployment of PV systems to the current electrical grid are the intermittent power generation by PV systems and their decentralized distribution, causing increased operating costs and power quality issues (Bollen & Hassan, 2011). The intermittency in PV generation is directly related to fluctuation in irradiance. In turn, this is driven by variations in cloudiness, characterized by a wide range of spatial and temporal scales (Perez, et al., 2015). At the national level, real-time balancing of supply and demand is commonplace. However, household PV introduces these challenges at the level of a street, neighbourhood, or city. This requires a new generation of distribution grid management, where accurate forecasts of the net load on the distribution grid enable mitigation of mismatch between local supply and demand (Schittekatte & Meeus, 2020). Forecasting PV power accurately and reliably on timescales ranging from minutes to days thus heavily depends on weather forecasts. Problematically, weather models struggle to accurately predict the occurrence and properties of clouds on small scales. The capabilities required for distribution system operators (DSOs) to locally match supply and demand can be summarized as follows; understanding of irradiance-induced grid issues, tailoring of weather predictions to deliver the level of detail required and applying these forecasts in operation to balance the grid.

The aim of this research

To enable optimal integration of solar energy into the electricity grid by advanced understanding of local meteorology.

System operators recognize that in addition to reinforcement of the grid, they also need to make better use of the grids capacity by balancing local supply and demand (Schittekatte & Meeus, 2020). For the distribution grid, this balancing on a local level needs to occur at three distinct spatial scales (Figure 1.1, right). The smallest scale is the street scale (~20 households, ~0.1 x 0.1 km²), which concerns a single low-voltage cable. The intermediate scale is the neighbourhood scale (~150 households, ~0.5 x 0.5 km²), where the key challenges lie in serving several street scale areas using a single distribution transformer. The largest scale is the city area scale (~10.000 households, ~10 x 10 km²), where key challenges involve delivering load prognoses

to the national transmission grid operator and balancing supply and demand. The nature of these issues varies at each scale level. For instance, at street level, PV generation can lead to a grid voltage exceeding safety limit (overvoltage event), whereas on postcode area congestion can occur due to limited grid capacity. At each scale level, specific smart-grid technologies are being introduced which require energy forecasts on technology-specific timescales, such as automated distribution transformers (minutes to hours) (Karagiannopoulos, Roald, Aristidou, & Hug, 2017) or neighbourhood batteries (hours to days) (Westering & Hellendoorn, 2020).

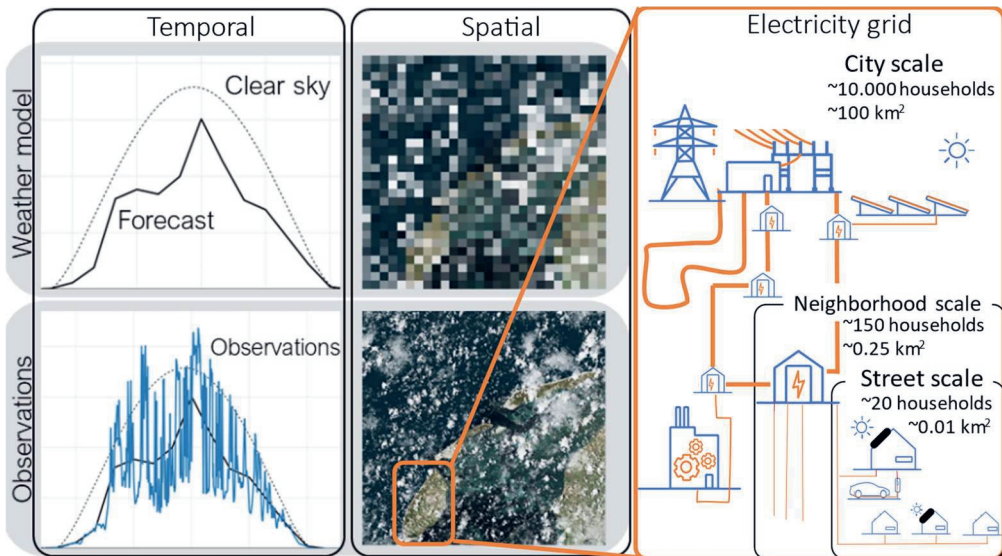


Figure 1.1: Left: Depiction of what state-of-the-art weather models provide (top) and what is observed with respect to irradiance time series (left) and spatial distribution of clouds (middle). The time series of observations shows rapid fluctuations, with peaks exceeding clear-sky values. This is a result of small clouds causing rapid transitions from shade to sun, which cannot be resolved by the current weather models. Right: Overview of three spatial scales on which Distribution System Operators need to balance the grid; city, neighbourhood, and street scale. The island of Texel, outlined in the bottom middle image, corresponds to the city scale.

From a forecast-application point of view (which is that of the grid operator); using forecasts on a daily basis is a novel affair, for which the exact requirements imposed by these technologies still need to be discovered using operational case studies. Simultaneously, from the forecast-provider point of view (which is that of the weather modeler), the operationally available, state-of-the art weather models deliver output at an hourly resolution and $2.5 \times 2.5 \text{ km}^2$, which is both spatially and temporally too coarse to accurately represent the dynamics on the grid (Figure 1.1,

left and middle). The disciplines of meteorology and grid management, specifically weather forecasting and system operations, traditionally have been separated; students go to different faculties, different universities even and high-impact journals from one discipline are often not available to the other. The large-scale integration of weather-driven energy generation resources into the electricity grid requires the combination of these fields, for which this thesis aims to provide a starting point.

1.2 Main objectives

The challenge of bridging what weather models can provide and what grid operators need to enable large-scale integration of PV into the grid, leads to the following objectives:

1. Quantifying high-frequency variability of irradiance and PV generation in relation to grid integration across spatial scales,
2. Providing a detailed analysis of PV-driven overvoltage events in the grid,
3. Tailoring weather forecasts to meet solar energy grid integration requirements,
4. Assessing impact of inaccurate weather forecasts during operational congestion management.

Within the scope of this thesis is to integrate the results into the daily operations of the DSO involved in this project. A screenshot of the short-term forecasting system at the DSO is given in Figure 1.2.

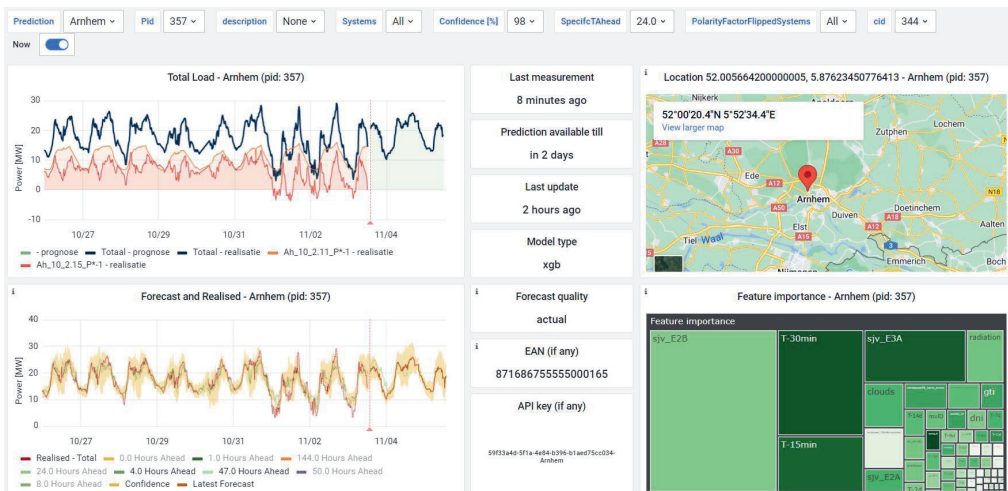


Figure 1.2: Screenshot of the forecasting dashboard at the DSO Alliander for a given substation. It shows the load of the past 7 days and forecast of next 48 hours (left), including confidence estimate (bottom left). Key performance indicators are given in the middle. Additionally, the geographic location (top right) and an overview of the relative importance of predictive features is shown (bottom right).

1.3 Societal Impact

The proposal for the project leading up to this PhD thesis was written in 2017. It started as follows: “Household PV generation is expected to increase in the next years to levels where the current electrical grid cannot accommodate the energy flows (Patero et al., 2017). This is already the case in Germany, where levels of PV penetration are much higher compared to the Netherlands. There, PV generation has led to a sharp increase in the differences of grid operating costs between regions ranging from 4.2 to 8.88 ct/kWh (Agora Energiewende, 2015). Similar issues are currently being observed with increasing frequency in the Netherlands.”

At the time of writing, it is 2022. This allows us to evaluate the claims of urgency made 5 years ago. A selection of headlines from Dutch media, depicted in Figure 1.3, shows that the urgency has only increased. Additionally, recent developments on the geopolitical and political level, such as Russia’s invasion of Ukraine, and stop of gas extraction in Groningen (NL), have sped up the desire for large-scale renewable generation even further (Ari, et al., 2022) (Hunta, Nascimento, Nascimento, Vieira, & Romero, 2022). All eyes are on the system operators to facilitate this transition.



Figure 1.3: A selection of Dutch news headlines relating to issues of grid capacity in relation to PV integration. From top to bottom: “Electricity grid is full and we will notice: waiting for solar panels and one in three streets under construction”. “Reinforcement electricity grid will take years: looking for smart solutions in the mean time”. “200 installed solar panels Schoolholm are waiting already for half a year to be connected to the grid”. “Solar panels turn off for 75.000 owners under the full sun”.

1.4 Layout of this thesis

This PhD research aims to bridge the fields of high-resolution meteorology and solar PV grid integration, both in terms of knowledge, as well as in terms of collaboration. To provide experts of one field an introduction to common knowledge from the other field, a high-level introduction to key concepts is given in **chapter 2**. The scope of this PhD project is refined to do the following;

The high-frequency variability of PV generation is expected to be a main source of PV-induced issues on the grid. These fluctuations are induced by fluctuations in irradiance. From a research perspective, irradiance has been studied in much more detail than generated solar energy. Therefore, this thesis starts by performing a detailed analysis to quantify PV fluctuations and their commonly observable extremes and relate them to those of irradiance. High-resolution measurements from a pyranometer, two household PV systems and one SMB PV system are combined for this analysis, which is presented in **chapter 3**. Findings of this analysis are key in defining the further research chapters of this thesis.

In 2015 the large-scale roll out of advanced metering infrastructure began, placing smart meters at almost every customer connection. This allows a vast number of measurements related to grid quality to be obtained. In **chapter 4** an analysis is presented on how this novel data source can help to shed light on PV induced grid issues. Spanning a 6-month period, more than 200.000 overvoltage events were gathered. These events are combined with ground-based irradiance measurements, satellite observations and power measurements at the substation. Chapter 4 how issues observed in the actual electricity grid relate to the variability of irradiance and PV generation characterized in chapter 3.

From here on, the focus of the chapters shifts from data science to machine learning. State-of-the-art, operationally available weather models provide irradiance forecasts at an hourly resolution. Chapters 3 and 4 highlight the importance of fluctuations at much shorter timescales (seconds to minutes). **Chapter 5** presents a methodology to forecast irradiance at 1-minute resolution at day-ahead lead-times, in terms of its probability density function. This is achieved by post-processing hourly output from KNMI's Harmonie NWP model using machine learning. The generalizability of the model throughout the Netherlands is shown, as well as its applicability to global-scale reanalysis models. Finally, a comparison to the next generation of weather models, based on 50m resolution Large Eddy Simulation, is performed.

Grid operators have only recently started to adopt day-ahead congestion management to locally balance the grid. While accurate forecasts of the net-load are required to stay cost-effective and ensure grid-safety, the operational achievability of this accuracy must be proven. **Chapter 6** presents an open-source machine learning framework to systematically analyse the predictability of load on a contingency. This framework is applied to a year-long case study where congestion management was applied to balance the grid on the city area scale. This allows the attribution of inaccuracies in the net-load forecast to errors in the forecasted weather parameters related to wind- and solar energy generation. Additionally, the impact of temporary unavailability of data during operations is analysed.

Finally, **chapter 7** summarizes the main findings of this work and discusses new avenues for future research. Concrete recommendations are made to aid the ambition of integrating more solar energy into the grid, using advanced understanding of local meteorology.

Chapter 2

Integrating Disciplines

The content chapters of this thesis are aimed at domain experts of meteorology and grid management. To provide a common basis to domain-specific key concepts, a high-level introduction is given here.

2.1 Clouds causing irradiance variability

Solar radiation varies across seasons due to the Earth’s rotation around the sun (summer, winter), between day and night due to the Earth’s rotation around its axis, and during the day due variations in cloudiness. Focussing on clouds, these are governed by meteorological processes ranging in scales from 1000’s of kilometres (Lau & Crane, 1997) to several kilometres (Brooks, Doswell, & Maddox, 1992). Respectively, the synoptic scale, such as a low-pressure area north of the UK causing clouds in North-West Europe (Figure 2.1, left) and mesoscale, such as a sea breeze bringing moist air over the warm land surface triggering the formation of cumulus clouds by convection (Figure 2.1, right). Here, the rising of warm, moist air leads to condensation of air moisture into cloud droplets. On timescales of seconds to tens of minutes, which are most relevant for solar energy grid integration, variability in irradiance is driven by the passage of clouds, openings in cloud decks and variations in the cloud optical thickness (Lohmann, 2018).

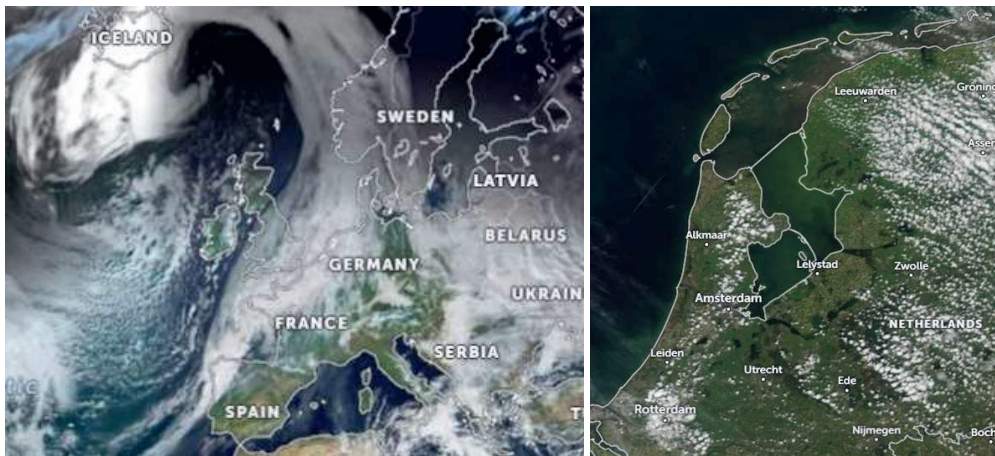


Figure 2.1: Left: Synoptic-scale weather system resulting in clouds over the Netherlands. Snapshot on November 27th 2022 by EUMETSAT. Right: Formation of convective cumulus clouds resulting from a sea breeze bringing moist air over a warm land surface. Snapshot on July 23rd 2022 by Aqua Modis.

Clouds cast shadows on the Earth’s surface by blocking direct sunlight. Counterintuitively however, the presence of clouds can also locally enhanced

irradiance by reflections from and scattering by cloud droplets (Gueymard, 2017), as depicted in Figure 2.2. Unfortunately, variability of irradiance does not directly translate to variability of solar energy generation. Observations of irradiance are typically performed using pyranometers with sensors in the order of cm^2 . Since solar PV systems are (much) larger, the peaks and dips of irradiance average out in PV generation (Lohmann, 2018). Moreover, studies on irradiance typically concern the horizontal plane (global horizontal irradiance, GHI), whereas PV systems are commonly tilted and irradiance variability on the inclined plane is known to be greater than on the horizontal due to a larger fraction of direct irradiance (Suri, Huld et al. 2007). Therefore, when aiming to understand variability of solar energy generation, a bridge needs to be made from the existing body of knowledge on irradiance variability.

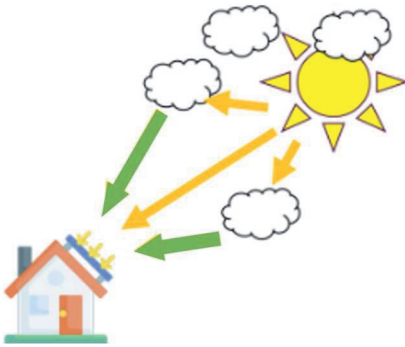


Figure 2.2: Reflections and scattering by cloud droplets can lead to increased irradiance at the Earth's surface. Arrows indicate paths of direct (orange) and diffuse (green) irradiance.

2.2 PV-grid integration

Solar panels turn irradiance into electricity. If rooftop-installed solar energy systems generate more energy than locally consumed, the excess is fed into the electricity grid, increasing the voltage. When voltage at the end-user exceeds 253 Volts (in the EU), it is considered to be an 'overvoltage'. Overvoltages can lead to unsafe situations and failure or even destruction of appliances for customers within the residential and commercial fields (David, Elphick, & Crawford, 2017). The effect of overvoltage has been described from a general power system point of view (Bollen & Hassan, 2011) (Jenkins, Allan, Crossley, & Strbac, 2000) as well as it has been considered for radial low-voltage grids specifically (Haque & Wolfs, 2016). When the feed-in increases, voltages increase directly. Short peaks of irradiance, resulting in

short peaks of PV generation therefore have a direct impact on overvoltage occurrence. Additionally, excess PV feed-in can lead to grid congestion, characterized by too high currents through components. Grid losses due to resistance (or impedance for AC current) scale quadratically with current and causes components to warm up. When currents are too high for too long, components can burn through. In the Dutch distribution grid, the transformer at the substation is often the limiting component when evaluating the PV hosting capacity of the grid. While many other issues on the grid can be caused by PV generation (Freris & Infeld, 2020), managing congestion together with overvoltages are the most important for the scope of this thesis.

2.3 Weather forecasting

Different methods exist to forecast the weather, of which the accuracy depends on the lead time and spatial scale. An overview of how these methods compare when forecasting irradiance is given in Figure 2.3. Total sky imagers (TSI) can be used to predict for the next 15 minutes, satellite images for the next hours, after which numerical weather prediction models provide the largest forecasting power. Since this thesis considers day-ahead lead times, NWP models are considered into more detail. As a basis, global scale weather models run for the entire globe, taking observations from satellites, airplanes, buoys and measuring stations as inputs and simulating how the weather will evolve. Due to the amount of computation required, these models have a 'coarse' resolution which corresponds to 31 km in the Netherlands, for the European weather model ECMWF (ECMWF, 2015). National weather institutes, such as the KNMI, take the output of these global scale weather models as boundary conditions for their simulations on higher resolutions, called mesoscale models (purple in Figure 2.3). For the Netherlands, the Harmonie-Arome mesoscale weather model (Bengtsson, et al., 2017) delivers operational forecasts at a 1h resolution, with a horizontal resolution of 2.5 km. Due to its higher resolution, it can resolve more of the processes, e.g. regarding cloud formation and transport, which leads to a more accurate forecast. Still, individual clouds are much smaller than 2.5 km. A future next step in weather forecasting can be Large Eddy Simulations (LES), which operate at much higher horizontal resolutions (Schalkwijk, Jonker, Siebesma, & Bosveld, 2015) (Heinze, et al., 2016) (van Heerwaarden, et al., 2017). Here, the detail level is so high that individual clouds are resolved. However, due to the high computation power required, these models are not available for operational forecasting at large scale. Therefore it is not included in Figure 2.3. However, LES can

run for local case studies, as performed in chapter 5 of this work, to indicate the potential for the next generation of operationally available weather models.

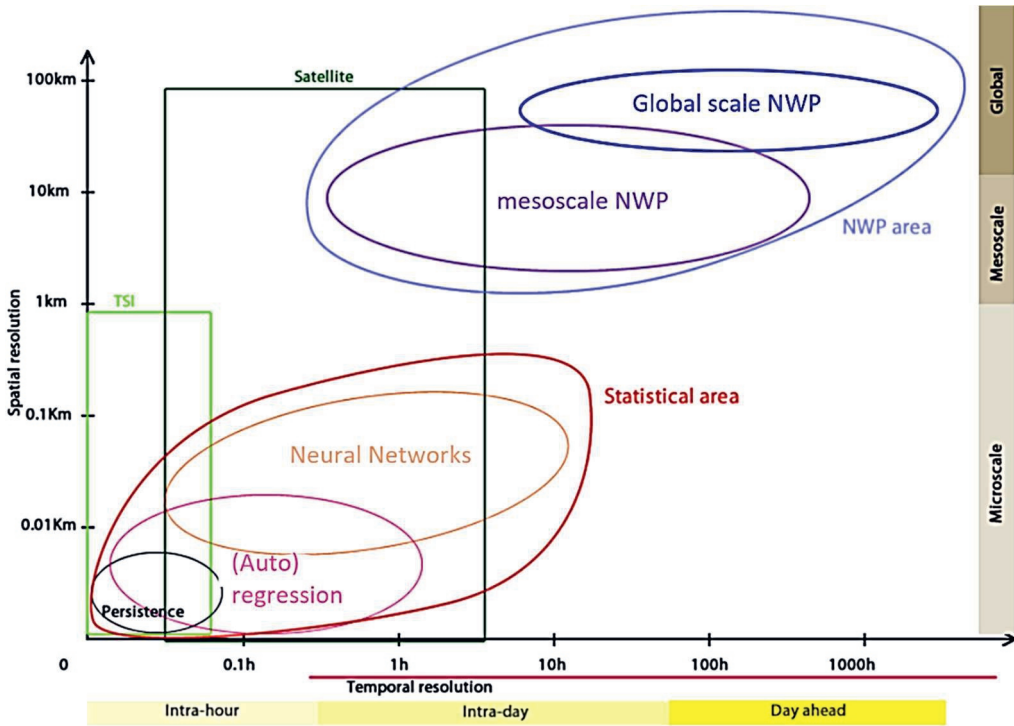


Figure 2.3: Overview of how different irradiance forecasting techniques compare to each other as a function of lead time and spatial scale (Diagne, David, Lauret, Boland, & Schmutz, 2013).

2.4 Supervised machine learning

Weather forecasts are not perfect. In addition to improving the quality of the input data, and physical relations within weather models, statistical and machine learning methods can be used to improve the accuracy of any given weather forecasting method (Pelland, Galanis, & Kallos, 2013). Similarly, these techniques can be used to combine forecasts from different sources into a more accurate prediction (Voyant, et al., 2017). On a high level, this post-processing is performed in three steps. First, a dataset is constructed which contains measurements of the target variable (e.g. irradiance), as well as the forecasted variable as provided by one or multiple forecasts, and other *predictive features*, such as other model outputs (e.g. temperature, pressure, humidity) or day of the year. Next, a model is trained on this

dataset, to learn the relation between the target variable and all predictive features. Here the model can for example learn that satellite forecasts are more important during the first few hours, after which the NWP models gradually take over. Or that satellite-derived forecasts typically underestimate irradiance when high cloud cover is predicted. Finally, during operations, the trained model is fed only the predictive features, and returns a prediction. Such a set-up, in which a known target variable is used to train a model is called *supervised learning*. Many different machine learning model architectures exist, each with its own advantages or aimed at a specific application (Mahesh, 2020). In this thesis, decision-tree based models are used (Swain & Hauska, 1977). These have the advantage of requiring only a limited amount of data and computation time for training, while also providing a relatively high level of interpretability. An example of a simple decision tree is given in Figure 2.4, which predicts if moment of irradiance enhancement (see paragraph 2.1) is to be expected, based on the predicted hourly average global horizontal irradiance (GHI) and cloud cover. The models used in this thesis leverage many of these trees together for every single prediction. Such a combination of decision trees is referred to as a *forest*.

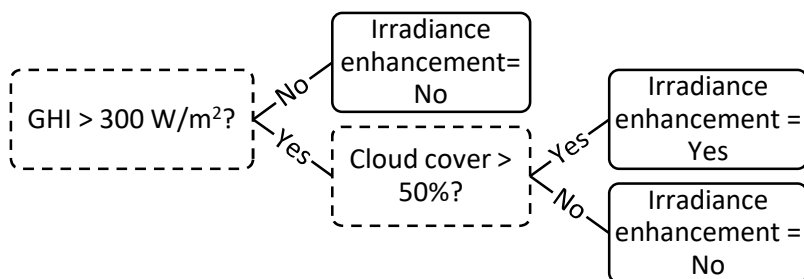


Figure 2.4: Example of a decision tree to predict if irradiance enhancement is to be expected, based on hourly average global horizontal irradiance and cloud cover.

Chapter 3

Analysis of high frequency photovoltaic solar energy fluctuations

This chapter is based on:

Frank P.M. Kreuwel, Wouter H. Knap, Lennard R. Visser, Wilfried G.J.H.M. van Sark, Jordi Vilà-Guerau de Arellano, Chiel C. van Heerwaarden (2020). Analysis of high frequency photovoltaic solar energy fluctuations. *Solar Energy*, 206, <https://doi.org/10.1016/j.solener.2020.05.093>

Abstract

Characterizing short-term variability of generated solar power is important for the integration of photovoltaic (PV) systems into the electrical grid. Using different kinds of high frequency, in-situ observations of both irradiance and generated PV power, we quantify insights on temporal averaging effects on the highest observed peaks and ramp rates, which closely relate to grid stability. We use measurements obtained at three specific spatial scales; a single point pyranometer, two household PV systems and a PV system typical for small medium businesses. We show that the 15-minute time resolution typically used for grid calculations significantly underestimates key dynamics at high temporal resolutions, such as ramp rates and maximum power output, at the local grid level. We find that absolute power peaks in the order of seconds are up to 18% higher compared to a 15-minute resolution for irradiance and up to 22% higher for a household PV system. For the largest PV system, the increase is limited to 11%. Furthermore, we find that the highest peaks solely occur under mixed-cloud conditions. Additionally, we show that the time interval-dependency of the largest power ramps is similar for all systems under research, ranging from ~20% at a 5-second interval to stabilizing at 70-80% between 5 and 10 minutes, which we can explain based on meteorological arguments.

3.1 Introduction

The worldwide installed capacity of photovoltaic (PV) solar energy systems is anticipated to multiply over tenfold in the next decade, from 486 GWp in 2018 (IRENA 2019) up to between 3 and 10 TWP in 2030 (Haegel, Margolis et al. 2017). As penetration levels of photovoltaics increase, weather-induced variability in power output of PV systems has a greater impact on the electricity grid. This can negatively impact utility grid stability by affecting grid voltage and frequency (Tan and Kirschen 2007), requiring additional regulation (Stetz, Appen et al. 2015). Because energy generation from renewable resources is highly unpredictable, grid operators design their grids for extreme power outputs such as in the case of clear sky condition.

At present, operational calculations used for grid design are limited to a temporal resolution in the order of 5 to 15 minutes (Sande, Danes et al. 2017). However, variability of solar energy due to cloud shading occurs at very short timescales, in the order of 1 second (Lohmann and Monahan 2018). Considering the typically used, coarser timescales the frequency and amplitude of high-frequency power fluctuations is flattened due to time averaging. Additionally, at short timescales cloud enhancement can lead to irradiance exceeding clear-sky conditions (Gueymard 2017), resulting in an increased PV power output, possibly causing grid voltages to exceed safety limits (Mills, et al. 2011) (Shah, et al. 2015), depending on inverter clipping or pre-set curtailment levels (Tonkoski and Lopes 2011).

High-frequency fluctuations of PV power output are mainly driven by fluctuations of irradiance. While the variability of irradiance (Kleissl and Lave 2013, Lohmann, Monahan et al. 2016, Lohmann 2018) as well as the power fluctuations of large solar parks (Perez and Hoff 2010, Marcos, Marroyo et al. 2011, Haaren, Morjaria et al. 2014) has been well studied, the effect on relatively small but abundant household PV systems remains poorly understood. It is anticipated that in the near future a significant part of the installed PV capacity will originate from these relatively smaller PV systems, typical for rooftops of homes and businesses (Šúri, Huld et al. 2017, 2019).

Up to this moment, research aimed at understanding the power variability of these type of PV systems has been limited to coarse temporal resolutions in the order of 10 minutes or relied on estimating PV output power from derived irradiance observations (Widén, Wäckelgård et al. 2010, Hansen, Stein et al. 2012, Hansen, Clifford et al. 2012, Anvari., Lohmann et al. 2016). Moreover, studies on irradiance

typically concern the horizontal plane, whereas PV systems are commonly tilted and irradiance variability on the inclined plane is known to be greater than on the horizontal due to a larger fraction of direct irradiance (Suri, Huld et al. 2007).

Additionally, the efficiency of solar panels depends on the temperature of the solar cells in the panels (Skoplaki and Palyvos 2009), whereas irradiance measurements do not have this temperature dependency. Due to the thermal capacity of the solar panels, broken-cloud conditions compared to clear-sky conditions can temporarily lead to lower cell temperatures resulting in a higher conversion and thus a higher output power (Jones and Underwood 2001). As Jones and Underwood found, the thermal response of a typical panel is in the order of 7 minutes, which is much larger than the timescales on which high-frequency fluctuations dominate. Although the effect of irradiance on the temperature of PV modules has been described in literature (Armstrong and Hurley 2010, Tsai and Tsai 2012, Lobera and Valkealahti 2013), this has not been connected to high-yield extremes observed at PV systems.

To enable large-scale integration of distributed and small-scale PV systems in the electricity grid and contain the risks of power output peaks and possibly power outages, a better understanding is required of the variability of generated solar power by a single or fleet of such systems and how this can be connected to existing meteorological knowledge of weather-induced irradiance fluctuations.

In this paper we present direct measurements of high frequency fluctuations in power output of PV systems and radiation observations. We show that these high frequency fluctuations have a profound impact on power output peaks in the electricity grid. We discuss how the physical behaviour of these PV systems poses significant challenges for power grid design. Moreover, we relate the behaviour of the household PV systems to the better understood weather-induced variability of irradiance and larger PV systems, typical for small to medium enterprises (SMEs).

Aiming to deliver insights ready for use by the utility sector, we examine commonly observable extreme values of two parameters as a function of time averaging interval, i.e., the maximum power and the maximum ramp rate. These parameters are closely linked to two aspects of grid stability: peak voltage limits and power-line flicker.

The rest of this chapter is organized as follows. Section 3.2 presents the definitions used throughout this work, and a description of the measurement set ups. In section 3.3, we present and analyse the effect of time-averaging high-frequency

observations for the systems under investigation. Finally, the work is concluded, and the impact of the findings presented in this work is discussed in section 3.4.

3.2 Method

3.2.1 Definitions

To quantify the impact of high frequency fluctuations on power peaks, we consider two variables in detail: the maximum instantaneous power P_{max} and maximum instantaneous ramp rate ΔP_{max} at a specific time resolution τ . To not let the results be impacted by a single high-value event, we analyse the 99.7th percentile of a given parameter as the maximum value ($R_{99.7}$, corresponding to 3σ), as we regard this to represent the commonly observable extreme. The expressions of these high frequency indicators read:

$$P_{max}(\tau) \equiv R_{99.7}(P(\tau)), \quad (3.1)$$

$$\Delta P_{max}(\tau) = R_{99.7}(P(\tau + 1) - P(\tau)), \quad (3.2)$$

where time averaged power $P(\tau)$ over time interval τ is defined by:

$$P(\tau) = \frac{\int_{\tau} P(t) dt}{\tau}. \quad (3.3)$$

To compare maximum power peaks and ramp rates between systems, we normalize each of the four datasets to the observed maximum power at a 15-minute time interval as this interval is the default time resolution of the energy industry:

$$P_{obs} \equiv P_{max}(15 \text{ min}). \quad (3.4)$$

3.3 Measurement Set ups

In this research we combine high-resolution measurement data from four set-ups: global horizontal irradiance, two household PV systems and an SME PV system measured with response times of 5, 2, 2 and 1 seconds, respectively. The set ups are located within a 40 km radius near the centre of the Netherlands.

The measurements of all systems were obtained between July 8th and September 1st. The households PV systems were measured in 2015 whereas irradiance and the SME PV system were measured in 2018. Year-to-year variations of irradiance can be

significant (Tonkoski and Lopes 2011), therefore this work is limited to comparisons of statistical parameters on timescales where the impact of year-to-year variations on the results is small. Furthermore, these statistical parameters do not require the systems to be on the same location.

3.3.1.1 BSRN irradiance measurement

Global horizontal irradiance is measured using a class A thermopile CMP22 Kipp & Zonen Pyranometer, classification to ISO 9060:2018 Spectrally Flat Class A (Kipp&Zonen 2019). The set-up is part of the Baseline Surface Radiation Network (BSRN) (Driemel, et al. 2018). For the BSRN station we consider here the data is stored at 1 Hz. High temporal resolution storage is not required by BSRN, the central BSRN database stores 1 min values, but is highly recommended for e.g. PV applications. Since the 95% response time of the device is 5 seconds, this is used as the highest temporal resolution. Calibration of the device can be directly linked to the World Radiometric Reference (World Meteorological Organization 2016). The system is located in Cabauw, the Netherlands (51°58'13"N, 4°55'35"E) and maintained by the Royal Netherlands Meteorological Institute (Knap 2015). Using Eq. 4, we find a P_{obs} of 0.87 kW, per m² of sensor surface.

3.3.1.2 Household PV systems

Two rooftop PV systems, comprised of c-Si panels, are connected with power measurement data loggers (Upp Energy 2013), as part of a larger PV system network (Elsinga and van Sark 2017). The power data is recorded at a resolution of 0.7 W and stored at 0.5 Hz. A summary of the technical details is given in Table 1. The two systems are oriented due south at an inclination of 47° and 40° and show a P_{obs} of 2.0 kW and 2.9 kW respectively. The inverter of the 2.9 kW household system has a rated AC power of 2.6 kW, thereby limiting the maximum output power of the system, even without cloud enhancement. The 2.9 kW system will be referred to as the 'inverter limited' system. With a capacity of 2.3 kW the inverter of the second PV system does not limit the power production. Both systems are located in the city of Utrecht, the Netherlands (52°05'N 5°06'E).

3.3.1.3 SME PV system

The SME PV system is comprised of 442 c-Si solar panels with a nominal capacity of 245 Wp, arranged in a 17 x 26 panel grid, divided into 6 subsections with a 3-phase inverter each. A summary of the technical details is given in Table 1, where the inverter rated AC power is the sum of the individual inverters. A remote terminal unit

measures the generated current per phase at 1 Hz using three LEM RT 500 Rogowski coils (LEM 2014) on the low-voltage cable at the secondary substation located approximately 60 meters from the PV system. The generated current is nearly identical for the three phases, as all inverters feed into each of the phases. Therefore, the generated power is calculated for one of the measured phases for which also the voltage is measured directly. In this research we will only refer to the generated power on the single phase, with P_{obs} of 27 kW. The system is located above a parking lot on an industrial area near the city of Duiven, the Netherlands (51°58'N, 5°59'E).

Table 3.1: Overview of the electrical installation details.

System	Household	Inv_limit	SME
City	Utrecht	Utrecht	Duiven
Orientation [°]	180	180	180
Inclination [°]	47	40	8
P_{obs} [kW]	2.0	2.9	27 single phase
Inverter rated power [kW]	3.0	3.0	99 three phases
Panel type	Hanwha Black Diamond Mono	Hanwha Black Diamond Mono	Sunpower Monocrystalline Silicon
Inverter type	Power One PVI-3.0-OUTD-S	Samil Power 3400 TLD	4x Growatt 20k UE 1x Growatt 12k UE 1x Growatt 7k UE

3.3.2 Data preparation

All time series were prepared following the same procedure. First, each dataset was resampled to exactly match its recording frequency. This is done by taking the average if multiple values were recorded in one interval, or linearly interpolating missing values, up to a limit of 5 subsequent missing values. Time intervals with a greater sparsity of observations are omitted from further analyses. Second, days with less than 95% of the expected data points between 08:00 and 16:00 UTC were omitted. In total, 56 days of the irradiance and inverter limited PV system were suitable, 54 days of the SME PV system and 39 days of the other household PV system.

3.3.3 Classification scheme

The weather conditions found on a certain day, e.g. overcast, clear sky or mixed, influence the maximum power output and ramp rate observed on that day. Moreover, due to cloud enhancement temporary extreme power output can be observed compared to clear sky conditions (Gueymard 2017). To allow for comparison of these results for different types of days, we categorize each day according to an adaptation of an earlier proposed classification based on Daily Clearness Index (DCI) and Variability Index (VI) (Stein, Hansen and Reno 2012). Instead of DCI, which requires a parametrization of clear-sky irradiance, we consider the surface integral (S) of the irradiance or PV energy yield, which represents the total energy. Secondly, we normalize VI to the day with the highest observed variability for each dataset: VI_n .

We then define four classes of days as follows:

- Highly variable: The 10 days with highest VI_n
- High yield: $VI_n < 0.2$ & $S > 2/3 * \max(S) + 1/3 * \min(S)$
- Low yield: $VI_n < 0.2$ & $S < 1/3 * \max(S) + 2/3 * \min(S)$
- Mixed conditions: All other days, they are included in our analysis

3.4 Results

3.4.1 Fluctuations in detail

Differences between data with high and low temporal resolution are most significant when fluctuations occur, e.g. during cloud to clear-sky transit periods. Figure 3.1 shows the solar power yield of the SME system for July 8th 2018 measured at a 1-second time resolution and time-averaged to 15-minute intervals. The inset shows a period of approximately 50 minutes in detail. This is a mostly clear day with a few morning hours of partially clouded conditions, ranging between 0 to 3 oktas as determined by an automated KNMI weather station located at 13 km (KNMI 2013).

According to the classification scheme described before, this is labelled as a 'mixed conditions' day. It is clear that on a 15-minute interval the absolute value of the

highest peaks as well as the amplitude, rate and number of power ramps are lower than on the 1-second interval.

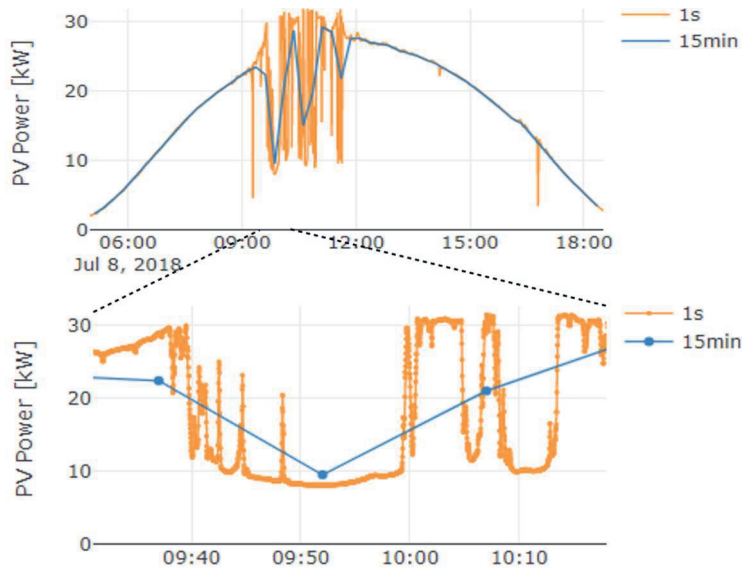


Figure 3.1: (a) Example of diurnal cycle of generated PV power of the SME PV system, showing the time-averaging effect of data with a temporal resolution of 1s and 15min, respectively; (b) Detail overview of a 32min period. The 1s data shows switching between a maximum and minimum state, which is clearly different from the 15-minute data.

For the inverter limited household PV system distinct plateaus of high values in the high-resolution yield data are observed at 3.2 and 3.0 kW. A time window with two of these steps in detail is shown in Figure 3.2. These steps occur after the output power of the solar panels has exceeded the rated power of the inverter. This under-dimensioning of the inverter is commonplace for both household and commercial PV systems, most frequently due to economic reasons. We consider these steps to be an artifact since the DC output power of the solar panels exceed the DC rated power of the inverter and not to be caused by meteorological effects. We do include these observations further in our analysis since they impact the effective peak and ramp rate of the system. The combination of downward steps with plateaus of constant high yield are not observed in the other datasets where the inverter rated power is greater than the installed capacity of the solar panels.

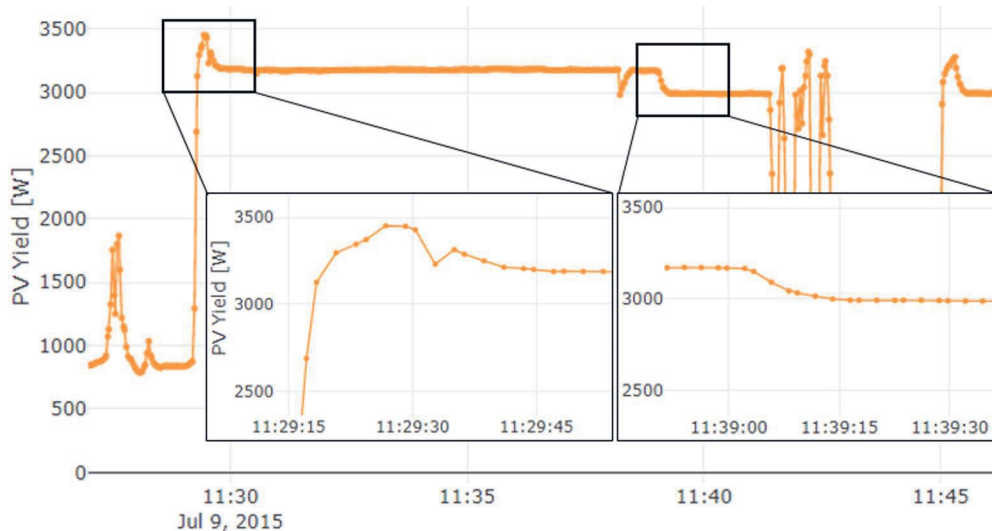


Figure 3.2: Detail view of the inverter limited household PV system yield showing distinct step levels. The time between the two subsequent steps is approximately 10 minutes.

3.4.2 Classification

When designing the grid, operators typically perform grid calculations for a selection of extreme cases. In the case of solar energy, days with clear-sky conditions are often assumed to represent the extreme case characterized by the highest values of generated PV power. However, we will quantify to which extent high-frequency fluctuations, not present under clear-sky conditions, can lead to higher stress on the grid in terms of peak power and ramp rate. In order to show this, we categorize each day of each dataset according to the classification scheme used in section 3.3.3.

An overview of the days and classes for the SME PV dataset is shown in Figure 3.3, while the other datasets showed similar results. This classification result compares well to previous studies (Stein, Hansen et al. 2012, 2013), where the shape is referred to as an ‘arrowhead’; due to the absence of days in the region with low variability index and medium surface integral. This is what one would expect; if a day has medium yield, both clear-sky and clouded conditions would have had to occur, meaning variability would have to be non-zero. Moreover, we find that the highest peaks only occur on days with partial and high variability of cloudiness.

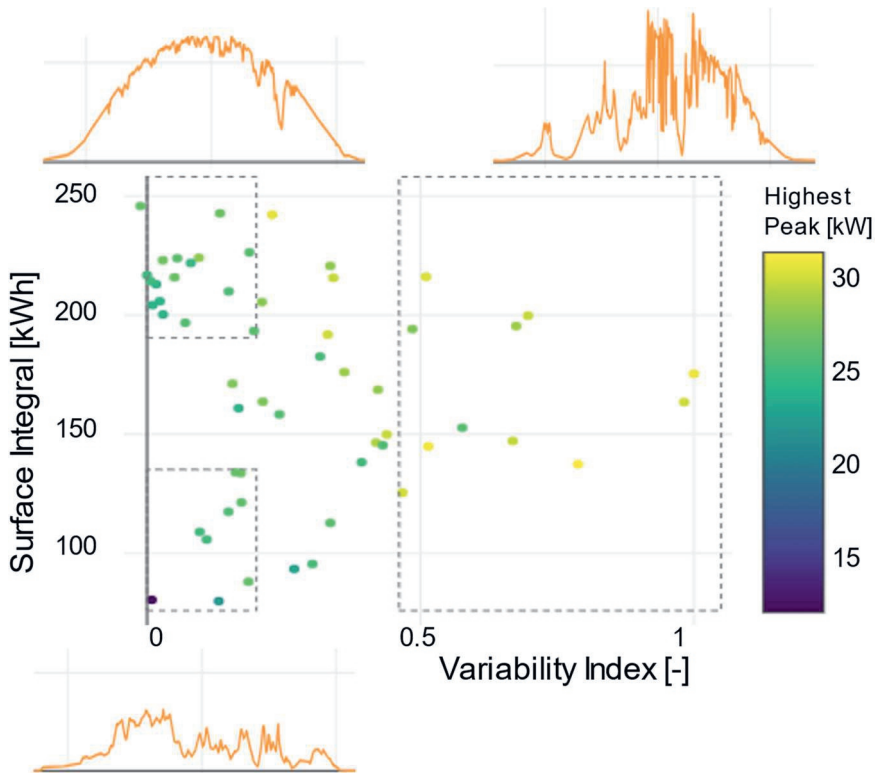


Figure 3.3: Classification into 'high yield', 'low yield', 'highly variable' (respectively top left, bottom left, right) of the SME PV system. The colour indicates the highest observed power output on the specific day. As a reference, irradiance profiles are depicted for the three mentioned classes.

3.4.3 Probability density

To assess the differences between measurements of the classes, excluding the mixed condition days, and investigate the effect of temporal averaging, we construct the probability density distribution of the raw, high-frequency observations and compare this to the distribution of the 15-minute averages of the same data. In addition to meteorological effects, the diurnal cycle of the sun leads to variability in solar energy. To focus on the meteorological effects, we only consider the time window between 11:00 and 13:00 UTC, which corresponds to the period around solar noon.

In addition to the probability density, kernel density estimates are shown using a Gaussian kernel (Elsinga and van Sark 2017).

3.4.3.1 Irradiance

The probability density function (PDF) of the raw BSRN irradiance measurements at Cabauw and the 15-minute averages is shown in Figure 3.4. The measurements clearly show that the highest values of irradiance are observed on days which are categorized as ‘highly variable’, and not on the days with the highest total yield. On days with high variability, irradiance values exceeding 1200 W/m^2 can be observed, as opposed to approximately 1000 W/m^2 on high yield days. This behaviour corresponds to earlier work regarding cloud enhancement (Parzen 1962, Gueymard 2017), where even more extreme cloud enhancement effects were reported. Additionally, we find that for highly variable days, the probability density distribution is strongly bimodal while it is unimodal for the high yield and low yield days. This bimodal distribution on highly variable days corresponds to previous research regarding irradiance (Yordanov, Midgard et al. 2012, Lohmann 2018). An accurate distribution of irradiance is important for solar PV, since many factors in converting irradiance to PV energy are non-linear, e.g. the efficiency of the inverter or resistance losses.

Considering the 15-minute averages, we find that even though the high yield and low yield days strongly correspond to the high-resolution observations, the PDF of the highly variable days shows a large discrepancy. Both the effect of cloud enhancement and the bimodality of the distribution are undetectable in the 15-minute time averaged data, complementing previous work on hourly averaged data (Skartveit and J.A. 1992).

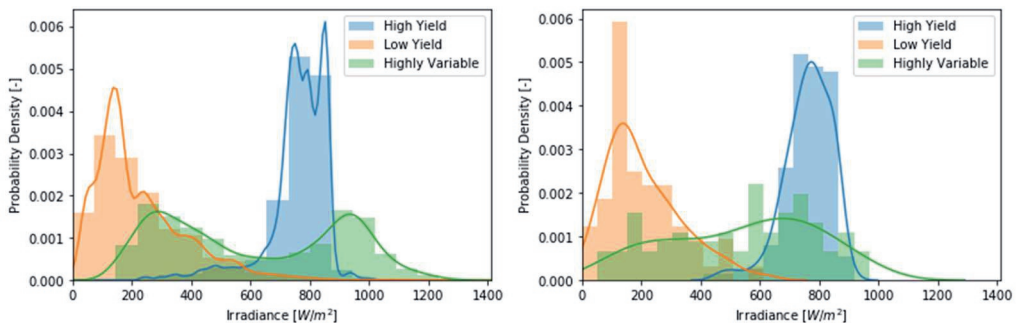


Figure 3.4: Probability density (areas) and kernel density estimates (curves) of the measured irradiance at the Cabauw BSRN site at 5-second resolution (left) and 15-minute averages (right). Similar results are obtained for PV measurements.

3.4.3.2 System comparison

For all PV systems in this study, we observe that the probability density distributions show great similarity to that of irradiance. The highest measured values occur solely on highly variable days, which is again due to enhancement of the irradiance due to the cloud radiation. For this class of days, we observe a bimodal distribution of solar power yield at high temporal resolution (Figure 3.5). Like irradiance, this bimodality is completely lost when averaging the observations to a 15-minute interval, see Figure A1 in appendix.

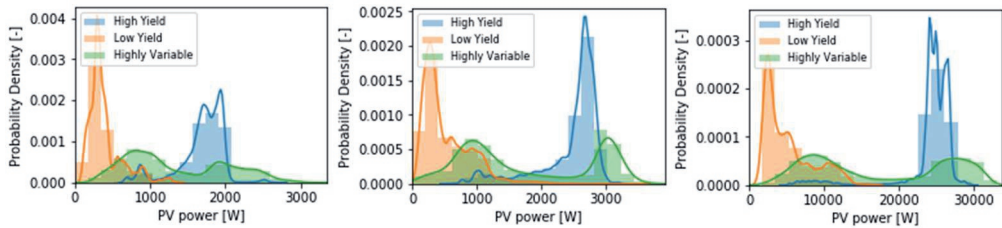


Figure 3.5: Probability density distributions of the high-frequency measurements of the PV household (left), PV household with limiting inverter (centre) and SME PV system (right).

Moreover, we find that for the inverter-limited system many observations correspond to the rated AC capacity of 2.6 kW. However, especially on highly variable days, the energy output can exceed the capacity significantly.

When considering systems of larger dimensions, a certain level of spatial averaging is to be expected, where the total system is comprised of smaller areas with varying irradiance conditions (Skartveit and J.A. 1992). Notably, even for the largest system under investigation we find the PDF on highly variable days to be bimodal, which agrees with the observation that even for the largest system, the dimensions of clouds are much greater than the size of the system. To a limited extent, spatial averaging effects can be observed when considering the peak of high yield on highly variable days; this is much wider for the non-limiting household PV system compared to the SME PV system.

If we relate this to grid impact calculations, we can state that 15-minute averages flatten the extreme values and the probability of ‘medium yield’ is exaggerated. Additionally, the probability density distribution of PV energy yield closely corresponds to that of irradiance.

3.4.3.3 Possible temperature effect

For the PV household system, we observe the largest difference between the highest values measured at highly variable days compared to high yield days, even larger than observed for the irradiance data. To some extent this could be caused by the higher sampling frequency of the PV measurements compared to the irradiance measurements. However, in section 3.4.4 we show that this effect persists when the same time averaging interval is used.

We hypothesize that in addition to the cloud reflection enhancement, an inverse temperature effect occurs on highly variable days compared to high yield days. The decreasing efficiency of solar cells with increasing cell temperature is well-understood (Haaren, Morjaria et al. 2014). Shading induced by transient clouds could lead to a lower effective cell temperature resulting in a higher energy output, as the response time of the temperature of the panel is much larger than the ramp rate of irradiance and PV systems themselves are virtually inertia less. The thermal response time of a typical PV panel is reported to be in the order of 7 minutes (Skoplaki and Palyvos 2009).

The other PV systems do not show this additional increase in yield. Possibly due to the under dimensioning of the inverter (PV limited system) or spatial averaging effects (PV SME system).

3.4.4 Averaging effect on peak power

For each of the systems under research, we have determined the peak power observed at a specific time averaging window, normalized to the peak power observed at the time average at 15 minutes. The results are depicted in Figure 3.6.

We find that for the PV household system, the peaks at the 2-second timescale are 22% higher compared to the 15-minute average. Notably, this is significantly larger than the increase observed for irradiance: 18% at 5-second interval. For the SME system, we find that at temporal resolutions of 10 seconds or smaller, the increase stabilizes at approximately 11%. We would expect that spatial averaging would lead to smaller increases for larger system sizes. However, this is not observed for the household PV system in Figure 3.5. As mentioned before, we conjecture that the additional increase of the household system compared to the increase in irradiance is due to temperature effects. For the inverter-limited PV system, the increase is

relatively small (12%). We assume this to be determined by characteristics of the specific inverter such as rated power and efficiency curves.

In the range between 5 seconds to 1 minute we still observe significantly higher peak power compared to the 15-minute averages, for all systems under investigation. This suggests that these are the typical timescales of cloud dynamics for which irradiance enhancement can be observed. However, the SME PV system, is insensitive to the increase for time resolutions higher than 10 seconds, indicating that irradiance enhancement is bound in space in a region typically smaller than the surface area of the SME PV system, which is in the order of 100 m².

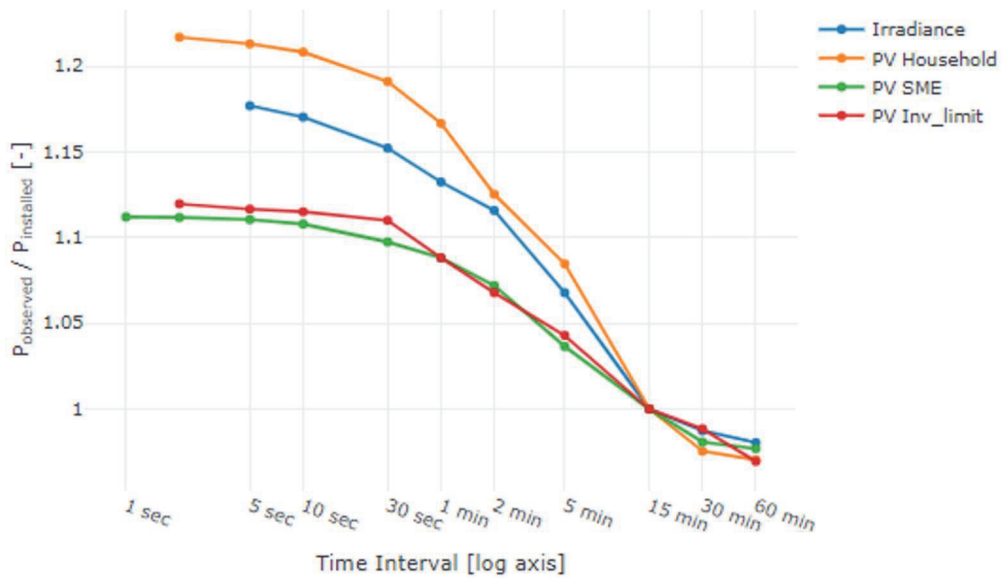


Figure 3.6: Overview of peak yield versus time-averaging interval for the four systems under investigation. Surprisingly, the largest effect of temporal averaging is found for the PV household system.

3.4.5 Averaging effect on ramp rate

Figure 3.7 shows the power difference between sequential time steps (power ramps) as a function of time averaging interval, normalized to the observed peak power at the 15-minute average, e.g. the same normalization is used as for Figure 3.6. All systems under research show a remarkably similar, sigmoid-like increase of normalized ramp rate with increasing time interval, from ~20% at a 5-second interval to stabilizing between 70 to 80% of the observed capacity somewhere between 5

and 15 minutes. Since even under completely clouded conditions the PV system still produces energy due to a non-zero diffuse irradiance component, the stabilization at high time scales occurs for a value smaller than 1.

The observed similarity between the behaviour of the systems is counterintuitive to what one might expect in the context of spatial averaging. A large difference in surface area exists between the systems under investigation; the surface area of the household PV systems is in the order of 2,000 times the surface area of the pyranometer, and the SME system even in the order of 77,000. This suggests that the ramp rate is not only determined by the transit time of the cloud edge over the system, but also by the large-scale spatial gradient of the cloud optical depth near the cloud edge. This gradient limits the ramp rate for small systems, where the transit time is in the order of seconds. Additionally, the electrical connection of the PV system may play an important role, since a shaded module can decrease the power of the connected string by more than the peak capacity of the module (Jones and Underwood 2001).

The ramp rate of the inverter-limited system slightly exceeds the other systems under research. We can provide a possible explanation: since the peak output power of the system is limited by the inverter, the observed maximum output power is small compared to the nominal installed capacity of the solar panels. Increases and decreases in output power can therefore be relatively greater than is the case for the non-limited PV household system. Additionally, the high ramp rate shown in Figure 3.7 indicates that the ramp rate is not the limiting factor for the relative small increase in peak power for the inverter limited system shown in Figure 3.6.

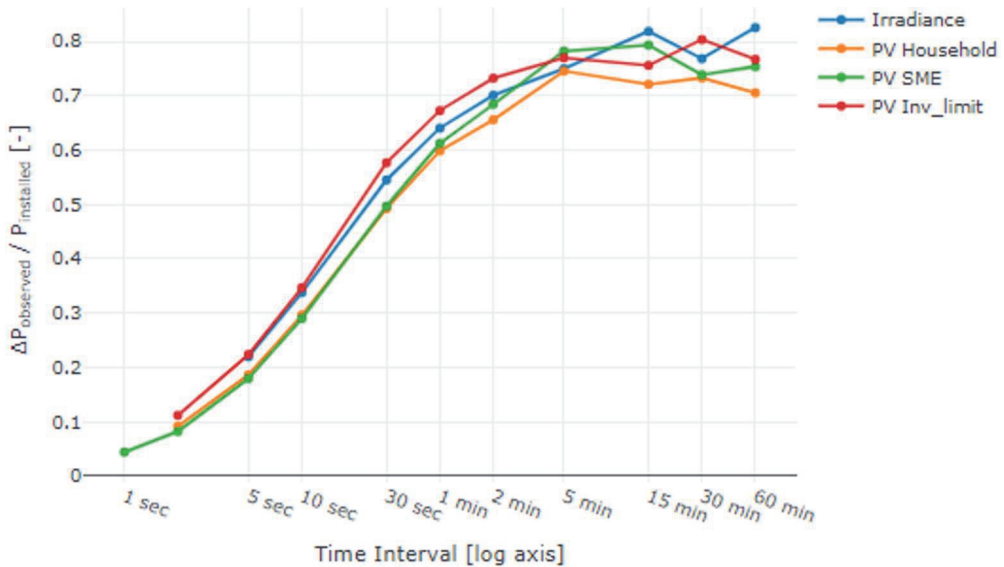


Figure 3.7: Overview of highest power ramps between sequential observations for increasing time-averaging interval, relative to the observed maximum peak power at 15min time-averaging interval.

3.5 Discussion and conclusion

We show that for both irradiance and PV systems typical for small and medium-sized enterprises, 15-minute time averages poorly represent behaviour at high temporal resolutions. At small timescales, all systems under research show at highly variable days a bimodal probability density distribution of irradiance or PV power that vanishes under 15-minute averaging. As noted in the introduction, increased PV power output and ramp rates increase the risk of grid voltages exceeding safety limits and threaten the stability of the electricity grid at the local level.

Our findings indicate that the highest PV power measurements do not occur under clear-sky conditions, but under mixed clouds and that this information is completely filtered out at the typically used 15-minute interval. The largest peak power at high time resolution is found for the household PV system at 22% higher than the 15-minute average. This is even larger than observable for irradiance (18%). We conjecture based on results shown in Figure 3.6 that in addition to cloud enhancement, temperature related efficiency effects lead to the largest peak power observations of PV systems under mixed-cloud conditions. For the largest system,

and the system where the inverter limits the output power, we find maximum power output increases of 11% and 12% respectively.

Notably, normalized ramp rates are very similar for all systems under research, ranging from ~20% at a 5-second interval to stabilizing at 70~80% between 5 and 10 minutes. Suggesting large-scale effects such as the gradient of optical thickness near the cloud edge to be dominant over the cloud-transit time over the system.

While it might be unfeasible to calculate the grid load for an entire year using a time step in the order of seconds, the results of this work are relevant to improve the business rules currently used to assess the PV hosting capacity of the electricity grid.

For grid operators, it is commonplace to perform detailed power quality calculations for a selection of 'worst case scenarios'. At present, the 'worst case' for PV is frequently assumed to be the maximum power output under clear sky conditions. However, we observed that the maximum power output of a PV system is up to 22% higher under mixed-cloud conditions compared to clear sky conditions. Additionally, the largest ramp rates are also found under mixed-cloud conditions. Therefore, we strongly recommend including these situations as well.

Moreover, since the largest fluctuations in power output occur at small time scales and the associated energy yield is very small, readily available power electronics could be included in the design of inverters to mitigate these grid-disturbing effects while only minimally impacting the return on investment of the PV system owner.

In this work we studied temporal averaging effects on power output characteristics of single systems. In practice, grid stability is not threatened by single, smaller systems, but by fleets of systems at distinct grid levels, e.g. low voltage cable (street), secondary substation (neighbourhood) and substation (city). While spatial averaging effects have been studied for irradiance, averaging of fluctuations of generated solar power have yet to be quantified directly. As we have shown in this work, power peaks of household PV systems can exceed those observed for irradiance. Possibly due to secondary effects such as an inverse relation between temperature and efficiency, which occur for PV systems but are not present for irradiance. While at present irradiance is frequently studied, future research is required to determine the combined spatio-temporal averaging effects on distributed PV system power output, given the non-trivial relation between irradiance and PV output power.

This work quantifies the commonly observable extremes of output power and ramp rates at very high temporal resolution, in relation to grid stability at the local level. Whether a short-lived extreme of PV power causes a grid safety or stability problem depends on many factors such as the properties of the grid components and the instantaneous load profile. Future research could use the relations described in this work to quantify the increased risk in grid instability.

Appendix

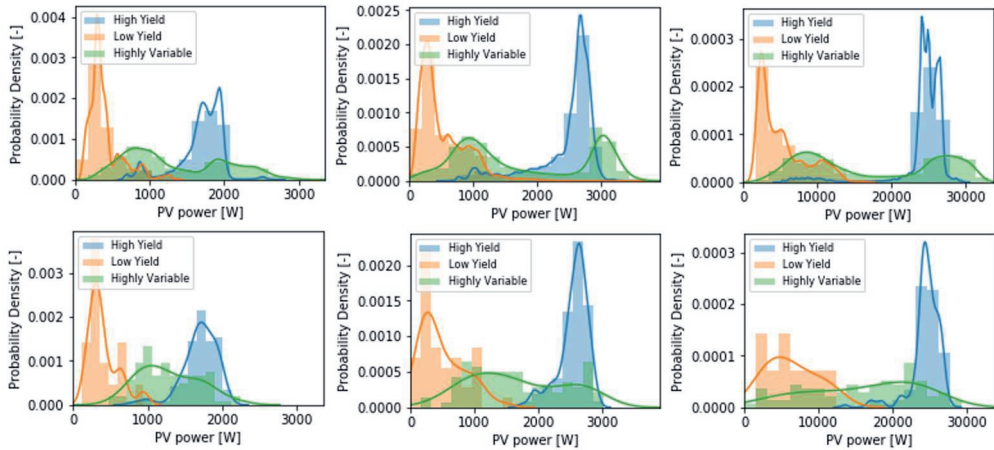


Figure A.1: Probability density (area) and kernel density estimate (line) of PV household (left), PV inverter limited (centre) and SME PV (right) at high frequency (top) and 15-minute average (bottom). All systems show a bimodal distribution at highly variable days at high-frequency, but this bimodality is lost when considering the 15-minute averages.

Chapter 4

Characterizing solar PV Grid Overvoltages by data blending Advanced Metering Infrastructure with Meteorology

This chapter is based on:

Frank P.M. Kreuwel, Wouter B. Mol, Jordi Vilà-Guerau de Arellano, Chiel C. van Heerwaarden (2021),

Characterizing solar PV grid overvoltages by data blending advanced metering infrastructure with meteorology, *Solar Energy*, 227, <https://doi.org/10.1016/j.solener.2021.09.009>

Abstract

If rooftop-installed solar energy systems generate more energy than locally consumed, the excess is fed into the electricity grid, increasing the voltage. Rising penetration levels of solar photovoltaic (PV) systems increase voltage levels, thereby threatening power quality. The extent to which solar PV cause grid issues in actual, nation-wide distribution grids, and how these issues correlate with cloud conditions and irradiance variability has yet to be quantified. This work provides a spatial and temporal characterization of overvoltage events linked to solar PV, using novel data sources. The analysis is based on over 200,000 events from advanced metering infrastructure (AMI) spanning 1/3rd of the Netherlands, combined with satellite observations and 1-minute irradiance measurements. As a result, we find that the typical duration of overvoltage events is in the order of 5 minutes and frequently-reporting meters are geographically dispersed. While overvoltages are driven by high PV generation, we do not find evidence that local, short-term irradiance peaks result in additional events as compared to clear sky conditions. However, we do find that median overvoltage event occurrence on Sundays is more than 2.1 times that of weekdays, which can be related to low energy consumption. Our findings indicate PV hosting capacity to be reached throughout the service area simultaneously, and surprisingly show no reduction in event duration by inverter- or grid control. Notably, while a sharp increase in occurrence is observed, overvoltage events are still scarce in absolute terms, with only 0.1% of the AMI reporting more than 10 events in spring-summer 2020.

4.1 Introduction

The penetration level of household photovoltaics (PV) is increasing. This in turn increases the occurrence of overvoltages, when photovoltaic (PV) feed-in minus local energy consumption exceeds grid constraints. This effect has been described from a general power system point of view (Bollen & Hassan, 2011) (Jenkins, Allan, Crossley, & Strbac, 2000), considered for radial low-voltage grids specifically (Haque & Wolfs, 2016) and mitigating control strategies have been proposed (Vergara, Salazar, Mai, Nguyen, & Slootweg, 2020). Studying and understanding the dynamics of these issues is require two major challenges to be tackled. Up to recently, distribution system operators (DSO's) have few to no measurements available in the low-voltage network for assessing the power quality (Abur & Expósito, 2004) (Zarco & Expósito, 2000) and are only informed of issues when end-users file a complaint with their grid operator. This lack of measurements from actual grids poses a challenge to the academic community as well, frequently limiting the scope of research to idealized, lab-condition grids, or labour-intensive small-scale case studies (Cobben, Gaiddon, & Laukamp, 2008). The large-scale deployment of advanced metering infrastructure (AMI, or 'smart meters') provides detailed data at an unprecedented scale (U.S. International Trade Commission, 2014), thereby creating opportunities to study and understand low voltage grid issues assiduously. Secondly, PV related power quality issues are driven by regional meteorology (i.e. clouds) of which observations at high spatial and temporal resolution are scarce (Driemel, et al., 2018).

Extensive research has been performed on several aspects related to PV grid integration challenges (Alboaouh & Mohagheghi, 2020). However, those works focus on each aspect independently. For instance, studies on the variability of irradiance (Lohmann, 2018) and events of overirradiance due to cloud enhancement (Gueymard, 2017) provide insights in the relevant temporal and spatial resolution of high irradiance events and under what weather conditions those can occur. Importantly, highest values of irradiance are found under broken-cloud conditions. Subsequently, fluctuations of generated solar PV energy for household PV systems (Kreuwel, et al., 2020) as well as utility scale PV plants (Haaren, Morjaria, & Fthenakis, 2014) (Marcos, Marroyo, Lorenzo, D. Alvira, & Izco, 2011) have been studied in great detail for several cases. These indicate that largest peaks in PV generation also occur on timescales in the order of seconds to minutes, depending on the spatial extent of the PV system. Finally, work has been performed to assess the impact of those fluctuations on grid quality, using small scale case studies of

feeder lines (Sharma, Aziz, Haque, & Kauschke, 2020) and simulated distribution grids (Cohen & Callaway, 2016) (Luo & Shi, 2020). Investigating the interdisciplinary relation between highly local meteorology and grid issues in actual grids on a large scale has yet to be performed.

The rise of distributed renewable energy causes low voltage grid dynamics to become strongly impacted by highly local meteorological conditions, in particular rapid perturbation due to the passage of clouds, openings in cloud decks and variations in the cloud optical depth. As such, it intertwines the fields of grid management and meteorology. Unlocking the full potential of large-scale smart-meter data has the potential to bridge the gap between these domains, thereby playing a key role in the energy transition. Our approach is to analyse widespread AMI overvoltage events using satellite observations as well as local, high frequency irradiance measurements. This combination allows for unprecedented analysis of distribution grid dynamics due to highly local radiation disturbances. Due to strict privacy regulations (General Data Protection Regulation (European Union, 2016)), large scale collection of AMI data is limited to anonymized overvoltage events, not allowing retrieval of more detailed time series of voltages or net power exchange at the end user connection.

In this work, we firstly study the characteristics of overvoltage events originating from AMI spanning a third of the Netherlands. We examine the typical duration of overvoltage events and compare this to that of high-irradiance events. Secondly, we investigate the distribution of overvoltage events per day and its evolution during a diurnal cycle. Thirdly we examine on a case study-basis the distribution of correlated clusters of overvoltage events in combination with satellite images. Lastly, we analyse in detail at overvoltage events in the vicinity of high-resolution irradiance measurements, quantifying the relation between cloud conditions and occurrence of overvoltage events. Since high frequency irradiance measurements are highly local, statistical parameters relating to variability and cloudiness are derived which are suitable for analysis outside the direct vicinity of the sensor (Stein, Hansen, & Reno, 2012).

We anticipate our study to be a starting point for more detailed studies on grid issues caused by the spatial and temporal variability of solar PV energy. For example, to link event occurrence to specific grid topology and asset specifications. The scope of this work is to analyse and describe the overvoltage issues which can currently be observed and how these relate to irradiance and cloudiness. We will not define a

statistical model for these events since the occurrence of a single overvoltage event is driven by many highly local factors for which data is, at least at present, not available at the national scale. For a detailed study on the effect of cloud enhancement on peaks in solar PV generation, the reader is referred to previous work (Kreuwel, et al., 2020).

The rest of this chapter is organized as follows. Section 4.2 describes the data sources and definitions used throughout this work. In section 4.3, characteristics of overvoltage events are analysed and their relation to local weather conditions is assessed. Finally, the work is concluded, and the impact of the findings presented in this work is discussed in Section 4.4.

4.2 Data and Methods

This work combines four distinct data sources, which are described in section 4.2.1. Figure 4.1 provides an overview of the spatial extent and relative location of each data source.

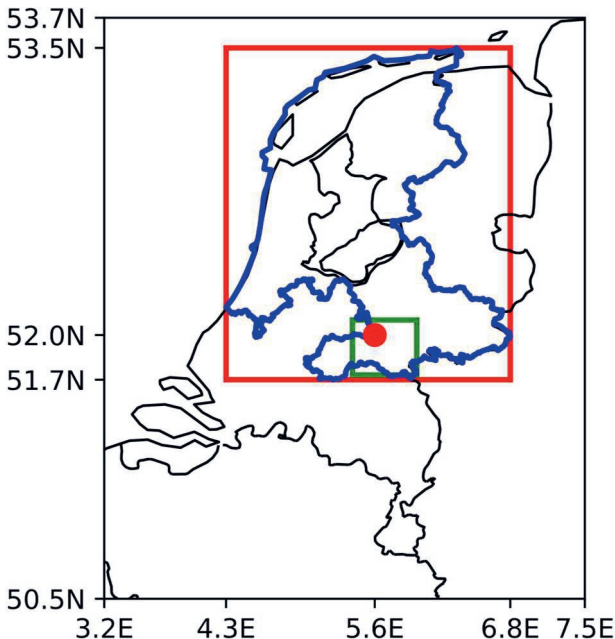


Figure 4.1: Overview of the spatial extent and position of each data source in relation to the other. Outer box (red): Terra and EUMETSAT coverage, curved outline (blue): region with overvoltage event monitoring, inner box (green): local case study, marker (red): irradiance observations.

4.2.1 Data

4.2.1.1 Overvoltage events

DSO Liander provided overvoltages events generated by their AMI consisting of approximately 2.5 million smart meters, of which the service area is approximately 1/3rd of the Netherlands (Alliander, N.V., 2020). The start of an overvoltage event is defined by the voltage at the connection point of the end user exceeding the nominal voltage by at least 10% for at least 1 minute. For the area of study, the nominal voltage is 230 V. The event ends when the voltage is again within 10% of the nominal voltage for at least 1 minute. The minimal duration of an overvoltage event is therefore 1 minute. A schematic representation of an overvoltage event is depicted in Figure 4.2.

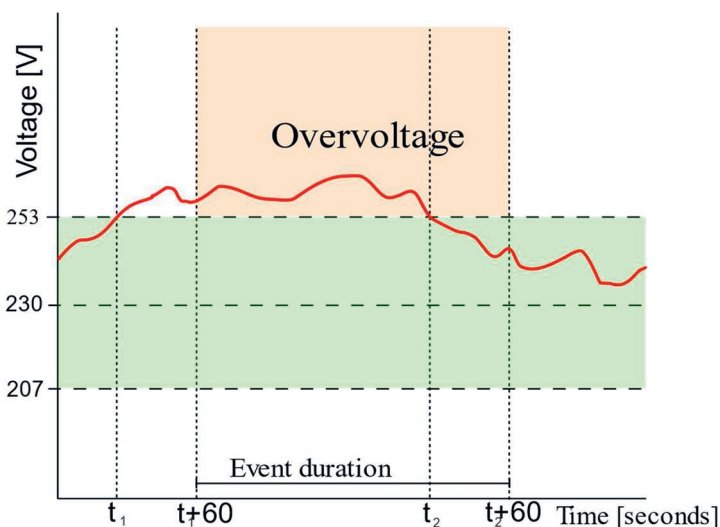


Figure 4.2: Schematical representation of an overvoltage event, defined as the period where the voltage at the end user exceeds 253V for at least 60 seconds.

In the period between the 3rd of February up to and including the 2nd of August 2020, a total of 203,866 overvoltage events, originating from 3,645 individual low voltage meters was received, representing approximately 0.1% of the smart meter population. The period of observations covers the general increase in solar energy production during spring, warm temperatures in summer which decrease PV efficiency and an almost complete variety of weather and specifically cloud conditions. Since strict privacy regulations govern the use of AMI-data, each meter was anonymized to a unique but non-traceable id and location information was

stored at a postal code level. Since the fraction of meters reporting events is very low, it is important to note that the quality of the meters is strictly ensured by national and European directives (Directive 2004/22/EC), (Netbeheer Nederland, 2021) ruling out that overvoltage events are significantly impacted by faulty observations.

4.2.1.2 Irradiance

Global horizontal irradiance (GHI) was measured on a 1-minute time resolution at an automated weather station near Veenkampen, the Netherlands (51.98°N, 5.62°E), using a CMP11 Kipp & Zonen pyranometer, conforming to ISO 9060 spectrally flat Class A. The fine temporal resolution enables accurate assessment of high-irradiance event duration, which allows for a comparison to overvoltage event duration.

Irradiance measurements are relevant only up to a limited distance from the observation site. Moreover, irradiance observations at 1-minute resolution are scarce for the area for which overvoltages are available, while previous work has shown that such high temporal resolution is required to capture peaks relevant for PV integration (Kreuwel, et al., 2020). Therefore, generalizable statistics of irradiance observations are used for the entire overvoltage dataset (section 4.3.1) while timeseries of irradiance observations will only be used to analyse a local-scale case study (section 4.3.4). The authors note that a high-quality observation site participating in the Baseline Surface Radiation Network exists at approximately 50 km from the weather station used in this work. However, for that region no AMI data was available since it was outside of the DSO service area.

4.2.1.3 Satellite observations

Remote sensing is used to assess cloud cover and cloud dynamics for locations of interest further away from the irradiance observations site. The MODIS instrument aboard the Terra satellite (Barnes, Xiong, & Salomonson, 2003) is used to observe cloud cover. The orbit of this satellite is timed so it passes the equator from north to south around noon, viewing the entire Earth's surface every 1 to 2 days. This allows for high resolution, static images of cloudiness.

Derived cloud products of EUMETSAT using the cloud physical properties algorithm (Roebeling, Feijt, & Stammes, 2006) are used to derive cloud dynamics for locations of interest. Cloud cover was extracted at a temporal resolution of 15 minutes, based on distance-weighted average of cloud mask. This geostationary satellite operates with an effective spatial resolution of 3x3km.

4.2.1.4 Net grid load

Due to GDPR restrictions, no load measurements at end user connection can be retrieved from AMI. However, at the substation level, measurements are available of the net grid load for the city of Wageningen (NL), representing approximately 18,000 households and 3,000 businesses. Active power measurements of the 50/10 kV transformer at a 5-minute resolution are retrieved through the supervisory control and data acquisition (SCADA) system of the DSO. While no direct measurements of the net load at the local, low-voltage level is available, the measurements at the substation give an indication of the load on lower grid levels.

4.2.2 Methodology

4.2.2.1 AMI pre-processing

In addition to solar PV, other types of electricity generation, such as wind or combined heat power, can increase the voltage levels of the grid, potentially leading to overvoltages. However, for the distribution grid in scope of this research, these types of generation are seldomly connected to the grid at the household-level. There are household-size wind generation installations installed at the low-voltage grid, however, the installed capacity of solar PV connected at the low-voltage grid greatly exceeds that of wind power. We will therefore disregard wind power as a significant source of overvoltages in this study.

To remove events not linked to PV feed-in, the following filtering was applied, where the number of events removed per step is included in parenthesis. First, overvoltage events with a duration of over 2 hours were removed (1199). In section 4.3.1 we will show that periods of high irradiance persist in the order of minutes, therefore we consider these extremely long events to not be primarily caused by PV feed-in. Second, the number of events was counted for every 5-minute interval. Four periods were found with suspiciously high number of overvoltage events. These are considered to be caused by large-scale grid issues, such as failing control logic of a substation voltage transformer and are therefore removed from the analysis (3067). As a last filtering step, events origination from meters with 10 or fewer events in total were excluded (6189) since observations from these locations were to carry statistical importance. As a result, 193,411 events originating from 1409 meters were used in the study. We do not filter on weather conditions or time of day, as to give an indication of overvoltage events that remain in the dataset after filtering which are not linked to solar PV.

4.2.2.2 Characterization of event duration

To help understand to what extent overvoltages are directly related to high values of solar energy production, we compare the distribution of the duration of overvoltage events to the duration of global horizontal irradiance exceeding certain thresholds. Hereby a linear relation between global horizontal irradiance and PV energy production is assumed. This assumption is valid since on the one hand, the timescales of overvoltage events are much greater than the response time of inverters, which is in the order of 25 milliseconds (Matsukawa, et al., 2003) while on the other hand still being small enough for other processes, e.g. changes in angle of incidence of solar radiation or thermal response of PV panels to have only a marginal effect. We examine the cumulative fraction of events as a function of event duration.

4.2.2.3 Spatial extent of linked events

To analyse the spatial extent of a cluster of overvoltage events, events are aggregated per numerical postal code level. This level corresponds to approximately 10 km² and 3,500 households (Centraal Bureau voor de Statistiek, 2018). We find that a large fraction of events is reported by a small fraction of meters, which we will distinguish as ‘frequently reporting meters’. Secondly, we analyse at the spatial distribution of both the frequently reporting meters and the entire meter population, to assess if certain domains of the service area of the DSO are overrepresented. To investigate this further, we perform a case study on three selected days within a one-week period, where the total event count ranges from low to high and assess geospatial differences in the occurrence of event-clusters.

4.2.2.4 Local case study on variability

To quantify the relationship between irradiance variability and cloud-conditions on the occurrence of overvoltage events, a detailed study is performed on a smaller region, of approximately 30x30km. Since irradiance conditions are highly local, a selection is made on overvoltage events origination from smart meters near the site of irradiance observations (section 4.2.1.2). This area is indicated by the green inner box in Figure 4.1.

In total, 62 smart meters were available from postal codes close that of the irradiance observation site which generated 4575 overvoltage events. First, a case study is performed on a 10-day period of different meteorological conditions to assess in detail the effect of cloudy, mixed-clouds and clear sky conditions on the occurrence of overvoltage events. Secondly, to determine if variability of irradiance

has a statistically significant effect on the number of overvoltage events, a quantitative analysis is performed on the entire time-domain. For this analysis, each day is classified based on its Daily Clearness Index (DCI) and Variability Index (VI) as described in previous work (Stein, Hansen, & Reno, 2012). The original, 1-minute resolution of the irradiance measurements is used to quantify DCI and VI.

4.3 Results

4.3.1 Event duration

The distribution of overvoltage event duration is examined. We find that 67% of the events last at most 5 minutes, and 92% last at most 15 minutes. The fractional cumulative sum of events as a function of event duration is compared to that of high irradiance events, as depicted in Figure 4.3.

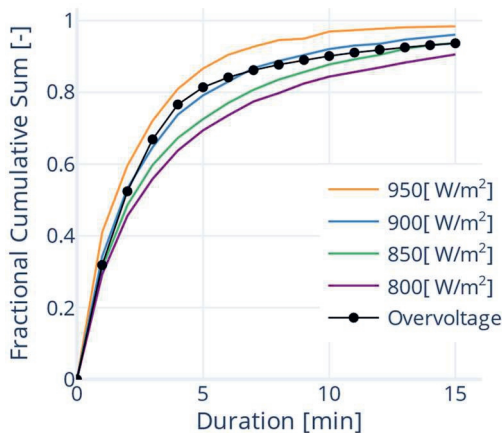


Figure 4.3: Distribution of event duration of overvoltage events (black, dotted) and events of high irradiance. The legend shows the threshold used for the irradiance events.

There is a strong agreement between the distributions of both overvoltage events and high irradiance events, with the overvoltage distribution matching closely the irradiance events for thresholds of 900 W/m², slightly flattening off to that of 850 W/m². The resemblance of the distributions is quite surprising. We had expected the duration of overvoltage events to be typically shorter than that of high irradiance events, due to overvoltage events being terminated by feedback loops of grid-control or active power curtailment by the inverter. However, the observed similarity suggests that these potential limiters of overvoltage event duration are not in effect,

at least not at timescales between 1 and 15 minutes. We will elaborate on the implications of this result in the discussion. Notably, a similar distribution has been found for cloud size density, which is well-described by a power law for smaller cloud sizes (Neggers, Jonker, & Siebesma, 2003), even though the relation between cloud size, high irradiance and overvoltage events is far from linear. In the next section we will investigate how the number of overvoltage events increases from spring to summer, and their geographical spread.

4.3.2 Temporal distribution

An analysis is performed on the temporal distribution of overvoltage events. Events are grouped to a total per 15-minute interval based on the event start-time, where we denote that the typical event duration is smaller than this time resolution. Figure 4.4 shows the increasing trend since the start of the year (x-axis) and the distribution of events during a diurnal cycle (y-axis). The distribution of overvoltage events follows that of the seasonal and daily solar cycle, as one would expect assuming solar PV energy being the main driver of overvoltage events. On a weekly basis, we find a strong increase, starting from approximately 1500 overvoltage events per week in spring, towards a more-or-less steady level of 9000 weekly events in summer. At the time-per-day level we see a close resemblance to a typical irradiance profile.

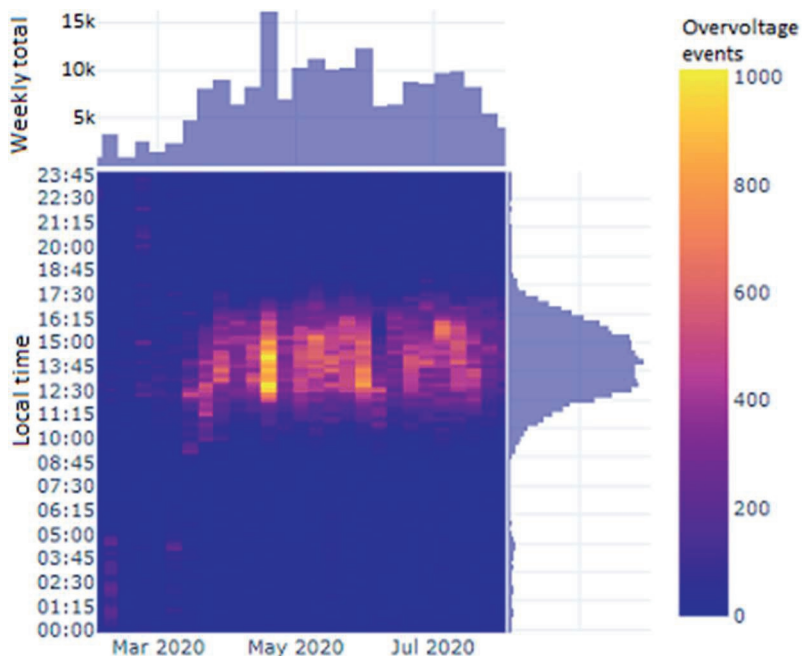


Figure 4.4: Temporal distribution of overvoltage events depicted as a density heatmap. The x-axis and marginal are grouped per week, while the y-axis is grouped per 15 minutes. The colour of the heatmap indicates the total number of events.

For some time-periods, especially during the first weeks of study, overvoltage events can be observed during night times. We conjecture that these events are not caused by solar PV, but by other sources. These events were not removed by the filtering process described under section 4.2.1, as to give an indication of non-PV related overvoltage events remaining in the dataset.

We investigate the distribution of total events registered per smart meter. The number of events per smart meter, and the geographical spread of events is depicted in Figure 4.5. We find that 61% of the events originate from 16% of the smart meters included in this work. This over-representation could be caused by a particular weak section of the grid. However, Figure 4.5 shows that frequent-reporting meters and the not-frequent-reporting meters are evenly distributed throughout the DSO service area.

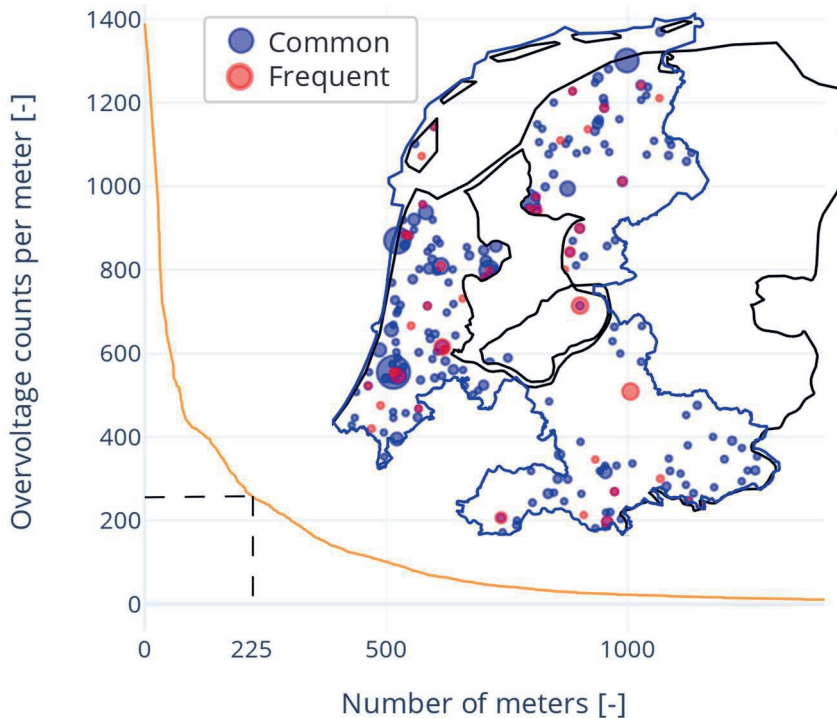


Figure 4.5: The distribution of overvoltage events per meter is skewed. The dotted line indicates the threshold where 16% of the smart meters account for 61% of the total overvoltage events. The map (inset) shows that both frequently reporting meters (red) and the not-frequently reporting meters (blue) are distributed throughout the DSO service area. The size of the markers gives an indication of the number of smart meters per postal code.

4.3.3 Spatial distribution

To assess the possible correlation of neighbouring cluster of events, a case study is performed on three days within the same week with few, moderate and many overvoltage events. Figure 4.6 shows the distribution of event clusters for each day, on top of observations from the Terra Modis satellite (Barnes, Xiong, & Salomonson, 2003). The selected days are 19th (left, 693 events), 17th (middle, 2242 events) and 23rd (right, 4016 events) of May 2020. These days feature commonly occurring meteorological conditions for this time of year in the Netherlands. Moist maritime air is transported inland, where the late-spring sun heats the surface enough to cause shallow convection and the formation of low clouds, which develops further downwind into cloud streets (Etling & Brown, 1993). This can evolve into stratocumulus due to a capping inversion associated with a high-pressure system, as

visible for May 17th. The prevailing wind direction for the respective days was WNW, W, WSW going left to right, as reported by the KNMI for location 'de Bilt', near the centre of the Netherlands (KNMI, 2009).

The condition, strength and PV hosting capacity of the electricity grid differs throughout the network. Before starting the analysis, we hypothesized that on days with few overvoltage events, the events would originate from the weakest sections of the grid, where impedance of feeder lines and the number of end customers is relatively high. On days with a higher number of overvoltage events, we would expect that in addition to the weakest sections, less weak sections of the grid would report overvoltage events as well. The circles in Figure 4.6 denote some areas of specific interest, where clusters only appear on some days, but not on others. Interestingly, the circle on the left indicates a cluster which only occurs on the day with the smallest total number of events. The occurrence of this cluster cannot be explained based on distinct cloud conditions derived from static satellite imagery. Similarly, for days with moderate and high number of events clusters are visible which only occur on that one specific day. These findings indicate that local effects, e.g., in energy consumption or production, strongly influence the occurrence of overvoltage events, and that it is not necessarily the case that specific weak grid sections experience overvoltage first.



Figure 4.6: Clusters of overvoltage events are shown for three days, on which the total number of events range from few (left, 693 events, 19-05-2020) to medium (middle, 2242 events, 17-05-2020) to many (right, 4016 events, 23-05-2020). The circles indicate regions where clusters occur only on specific days. The cloud observations originate from the Terra Modis satellite.

While the Terra Modis satellite provides information on cloud cover at an extremely high spatial resolution, the single observation in time is unable to capture cloud dynamics. A complementarity analysis is given by the derived cloud products of EUMETSAT using the cloud physical properties algorithm (Roebeling, Feijt, & Stammes, 2006). Cloud cover was extracted for the three areas of interest at a temporal resolution of 15 minutes, based on distance-weighted average of cloud mask. Figure 4.7 shows the cloud dynamics for May 17th, as well as the overvoltage events of the southern area of interest. For comparison, the overvoltage events are grouped as a total per 15 minutes. The other areas of interest reported no overvoltage events, even though the cloud cover was constantly low. While the cloud cover shows a large evolution during the day, moving from almost completely clouded to near clear sky, these dynamics are not reflected in the reported overvoltage events.

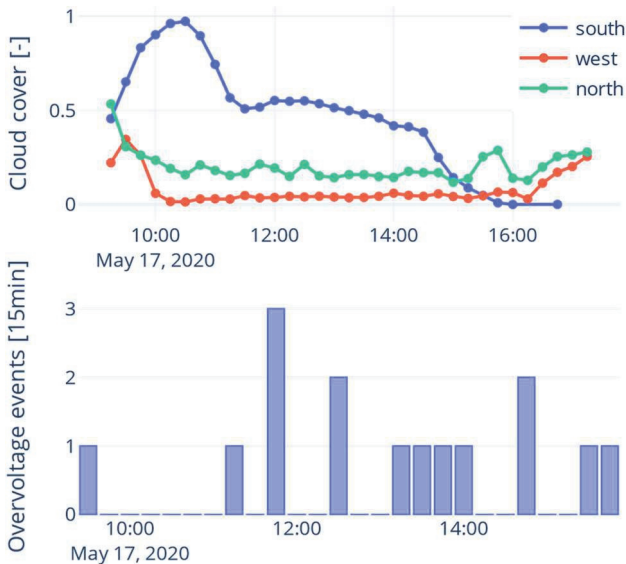


Figure 4.7: Evolution of cloud cover (top) for the three areas of specific interest and total overvoltage events per 15 minutes for the southern area of interest (bottom), for 2020-05-17. Derived cloud cover originates from EUMETSAT observations.

4.3.4 Impact of variability

To further quantify the impact of highly local effects, overvoltage events are selected which originate from AMI near the irradiance measurement site, as described in section 4.2.2.4. Figure 4.8 shows the diurnal cycle of irradiance at 1-minute

Chapter 4

resolution and overvoltage events at 15-minute resolution for a period of 11 consecutive days spanning 19th -29th of March. This period features a wide variety of cloud conditions within a short time span, such as clouds (March 19th and 20th), broken clouds (29th) and clear sky (21st to 28th). For context, Terra Modis satellite observations are included at the top. The bottom part of the figure depicts the net grid load of a substation in the case study region, as described in section 4.2.1.4. The load of the substation is an indication of the net grid load on lower voltage levels. As expected, almost no overvoltage events are measured under clouded conditions. However, even though the irradiance observations are nearly indistinguishable under clear sky conditions, there is a large spread in total overvoltage events per day, with 23rd to 27th of March showing a substantially smaller number of overvoltage events. Coincidentally, the four days with many overvoltage events are all weekend-days (March 21, 22, 28, 29), indicated in Figure 4.8 in grey.

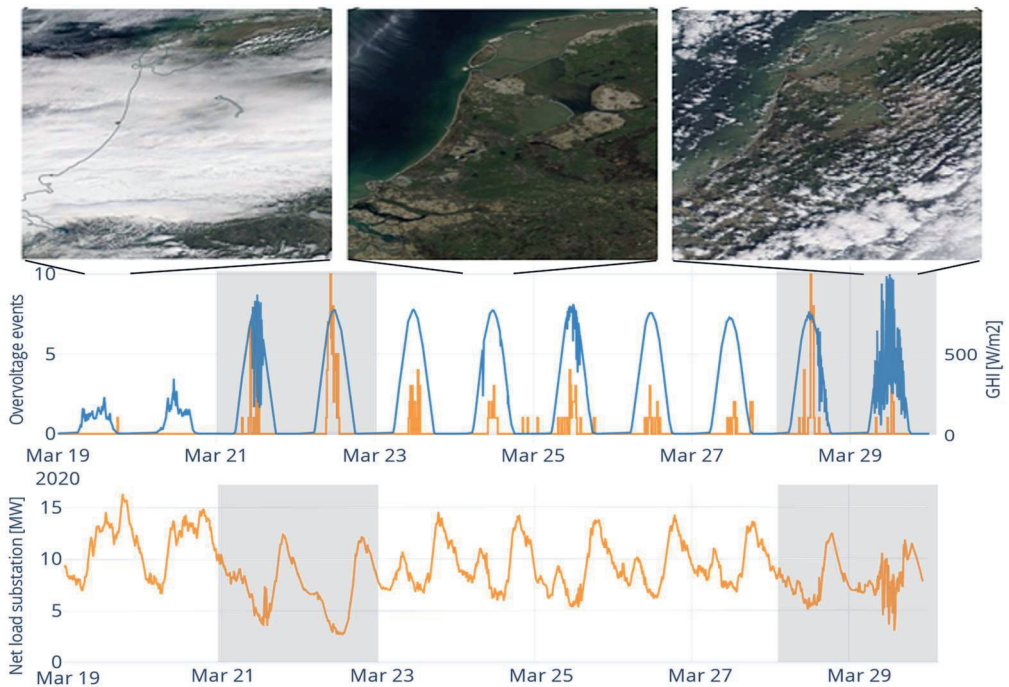


Figure 4.8: Depiction of 11 days of the local case study on overvoltage events. Top: Terra Modis satellite observations indicate cloud conditions for three selected days, corresponding to overcast (left), clear sky (centre), and broken-cloud conditions (right). Middle: overvoltage occurrence (orange, left y-axis, 15-minute bins) in relation to global horizontal irradiance (blue, right y-axis) at 1-minute resolution. Weekends are shaded grey. Bottom: Net load on the level of a substation in the local case study region.

A statistical analysis is performed on smart meters near Veenkampen for the entire data acquisition period to evaluate significance of irradiance variability on the one hand, and day of week on the other. Effects of cloud enhancement, where partial cloud cover leads to irradiance exceeding clear sky irradiance, can be observed on 21st and 29th of March in Figure 4.8. Using the methodology referenced in section 4.2.2.4, each day of the entire dataset is categorized as ‘clouded’, ‘variable’, ‘clear’, or ‘mixed’ according to their DCI and VI, based on the irradiance observations at a 1-minute resolution. Figure 4.9 shows the distribution of daily aggregated overvoltage events per type of irradiance, where the number of events increases as the total irradiance per day increases. We note that the spread in events per day is considerable. Additionally, we calculate the median overvoltage events as a function of day of the week, for which the result is shown in Figure 4.10. Notably, the median overvoltage event count on Sundays is 2.1 that of weekdays. From Figure 4.8 it is clear that on weekend-days around noon, the net load at the substation level reaches its minimum. This corresponds to a combination of high PV generation and low energy consumption. At this aggregation, the load is positive, indicating net energy consumption. However, on the local, low-voltage level, this can correspond to high amounts of net feed-in of PV energy.

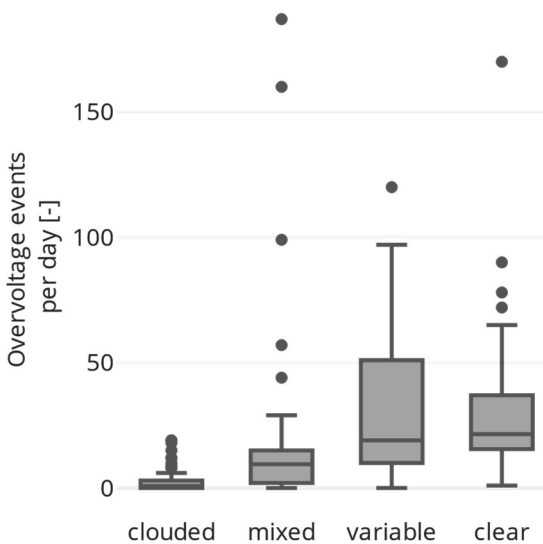


Figure 4.9: Distribution of overvoltage events aggregated per day, as a function of irradiance category. Whiskers mark the closest points to points within 1.5 times the interquartile range, while the vertical line in the box indicates the median.

Using Student's t-test (Student, 1908), we study if the difference in the mean overvoltage events per day for each category, given the event distribution, is statistically significant. We find that the distributions on 'variable' versus 'clear' days do not differ with statistical significance. However, for the difference between overvoltage events on Sundays compared to weekdays, we find a p -value of 0.016 indicating statistical significance.

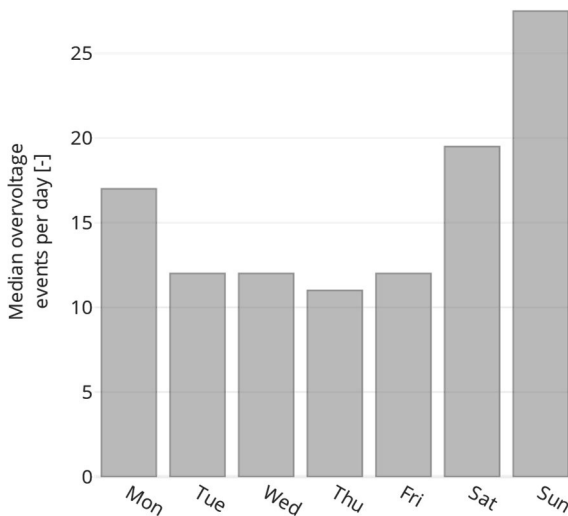


Figure 4.10: Median of daily overvoltage events per day of week. On Sunday, a significantly higher number of overvoltage events is observed.

4.4 Discussion and conclusion

4.4.1 Discussion

This study presents a characterization of solar PV induced overvoltage events reported by AMI, in relation to clouds and irradiance variability. Previous work showed the dominant timescales for peaks in PV generation to be in the order of seconds to minutes, for household PV systems (Kreuwel, et al., 2020) as well as utility-scale PV parks (Haaren, Morjaria, & Fthenakis, 2014) (Marcos, Marroyo, Lorenzo, D. Alvira, & Izco, 2011). In this work, we showed the dominant timescales for overvoltage events to also be in the order of minutes. Surprisingly, we did not observe a decrease in overvoltage event duration as an effect of voltage control, such as active power control by droop curves in end-user inverters (Vasquez, Mastromauro, Guerrero, & Liserre, 2009) (De Brabandere, Woyte, Belmans, & Nijs,

2004) or onload tap changers at substation transformers. We would like to point out that this is only investigated under the condition that an overvoltage event occurs in the first place. In all likelihood, many potential events are already mitigated on within the 1-minute duration threshold, or some form of voltage control has acted before the voltage threshold at the end user is exceeded.

Our results show that while high irradiance is required for an overvoltage event to occur, the variability or height of irradiance peaks is not. The impact of ‘Sunday versus weekday’ exceeds that of ‘clear sky versus broken clouds’, as described in section 4.3.4. Based on open-data standard consumption profiles provided by the Dutch energy sector (NEDU, 2020), we find that mainly industrial energy consumption diminishes on Sundays, whereas household energy consumption only slightly decreases. As discussed in the introduction, previous work shows that broken clouds lead to the largest peaks in irradiance (Gueymard, 2017) and PV energy generation (Kreuwel, et al., 2020). However, we find the impact of low energy consumption exceeds that of irradiance peaks in causing overvoltage events, at least for the area considered in this study and current penetration level of household solar PV systems. We conjecture that when the number of PV systems increases and the hosting capacity of the grid is reached, the impact of irradiance variability on overvoltage incidence could surpass that of low energy consumption.

The scope of this work does not include detailed analysis into the context and origin of individual overvoltage events, such as grid topology, asset information and end-user energy consumption. The reason for this decision is the strict conditions under which AMI data can be used, specifically in relation to the GDPR (European Union, 2016). While many novel and important results have been presented based in this work, a lower level of aggregation of overvoltage events would allow for more detailed studies, for instance into the impact of end-user behaviour and specific grid parameters on overvoltage event incidence. In particular, the large-scale analysis of overvoltage events in relation to clouds and cloud dynamics presented in this work could greatly benefit from the addition of such specific information. Potentially, this would allow definitive explanation of the occurrence and absence of clusters of overvoltage events on particular days, thereby aiding in the challenge of integration high levels of solar PV into the grid. Despite the good intentions of the GDPR, its current interpretation limits scientific and societal progress.

While the number of events shows a strongly increasing trend, the fraction of smart meters reporting overvoltages is still well below 0.1%. Additionally, many other

processes apart from solar PV can trigger an overvoltage event, such as other types of decentralized energy generation, failing control-logics or non-compliance of end-users. However, the relation with irradiance is strong to such an extent that a detailed statistical characterization is already possible as shown in this work.

4.4.2 Outlook

The framework provided in this work can help to assess overvoltage events on both a large and a local scale. Information on typical event duration and spatial extent can aid grid operators in improving their AMI data acquisition routines. For example, at present only events are triggered when voltages are exceeded beyond regulatory levels. After interviewing subject matter experts at DSO Liander, we recommend including additional triggers at lower voltage levels, e.g. 6-8% of the nominal voltage. This would make it possible to identify grid section where PV penetration levels start to reach the hosting capacity even before end users experience any issues. Thereby enabling data driven preventive maintenance and grid reinforcements, resulting in an increased hosting capacity of the grid. Additionally, we recommend repeating the analysis discussed in this work with an updated dataset next year to further investigate the relation between irradiance, PV penetration levels and overvoltage event occurrence.

Interviews with subject matter experts at the DSO indicate that when a power quality issue is reported by a customer, voltage profiles from neighbouring smart meters of a limited duration are requested, which differ from overvoltage events. This work gives a starting point on how overvoltage events can help to understand and proactively mitigate PV related issues.

4.4.3 Conclusion

This work provides a thorough characterization of overvoltage events in the distribution grid due to solar PV on a nation-wide scale, using novel data sources. Using high resolution irradiance observations in a local case study, we find that median overvoltage event incidence on Sundays compared to weekdays is 2.1 times higher, while no distinction could be found between highly variable irradiance during broken clouds or constant irradiance during clear sky conditions. This suggests that, while overvoltages are caused by high PV generation, overvoltage event incidence is increased more strongly by low energy consumption than by short peaks of high

feed-in. We find that a small number of smart meters is responsible for many events, but that these do not indicate any particular weak grid segments. This indicates that the PV hosting capacity of the electricity grid is reached simultaneously throughout the service area of the DSO. When grouping events into clusters at a postal-code level, we find no clear relation in event incidence between separate clusters, not even in conjunction with static or dynamic satellite observations. On weekly to monthly timescales, a strong increase in overvoltage events is found during spring which flattens out towards the summer, from approximately 1.500 weekly events up to 9.000 with a peak exceeding 16.000, on an AMI population of 2.5 million.

Chapter 5

Forecasting day-ahead 1-minute irradiance variability from Numerical Weather Predictions

This chapter is based on:

Frank P.M. Kreuwel, Wouter Knap, Maurice Schmeits, Jordi Vilà-Guerau de Arellano, Chiel C. van Heerwaarden (2022). Forecasting day-ahead 1-minute irradiance variability from Numerical Weather Predictions. Under review.

Abstract

Accurate forecasts of solar irradiance are required for the large-scale integration of solar photovoltaic (PV) systems. Fluctuations of energy generation in the order of minutes can lead to issues on the electricity grid, therefore reliable forecasts of minute-to-minute irradiance variability are required. However, state of the art numerical weather predictions (NWP) deliver forecasts at a much coarser temporal resolution, e.g. hourly, missing crucial information on meteorological variability such as clouds. In this work we present a methodology to forecast minute-to-minute irradiance variability in terms of its probability density function (PDF) based on hourly NWP results, by applying statistical postprocessing using machine learning. The algorithm is tested using the 2.5x2.5 km² HARMONIE-AROME (HA) mesoscale model as input, with 1-minute irradiance observations for 18 meteorological stations throughout the Netherlands used as a ground truth. The applicability of the algorithm to 31x31 km² global-scale models is investigated using ERA5 reanalysis data, which yields comparable accuracies. We find that almost half of the inaccuracy of the postprocessed result is due to errors in the radiation forecast of the NWP model used as input. Finally, the proposed post-processing algorithm is compared to the next generation weather models based on high resolution Large Eddy Simulation (LES), at 75 m horizontal grid spacing, on a case study spanning four days. While LES underestimates values of high irradiance due to lack of 3D radiative effects, it enables detailed analysis of cloud and irradiance dynamics at high spatial and temporal resolution unreachable by statistical postprocessing.

5.1 Introduction

Solar photovoltaic (PV) energy plays a crucial role in societies' transition to renewable energy. Utility-scale PV plants as well as distributed, rooftop-installed systems are being installed at a rapid pace, being the largest growing source of renewable energy in 2021 (IRENA, 2021). Energy supply and demand on the electricity grid must be always balanced. Solar irradiance at ground level, however, is intermittent and highly variable (Lohmann, 2018). Alarmingly, the currently installed capacity of PV power is leading to issues on the electricity grid (Goyle, 2012). These issues limit the pace of the energy transition significantly.

Variations in solar PV energy are dominated by changes in weather conditions (Perez, et al., 2015). In the cloud cycle these are characterized by formation, dissipation and transport (Lamer & Kollias, 2015). Numerical weather prediction (NWP) model forecasts are used for operational planning by utilities and distribution system operators (DSO). However, the output of limited-area NWP forecasts is available on a temporal and spatial resolution typically in the order of 1 hour and several kilometres, respectively. This means that clouds are resolved poorly and inaccurately, and information of intra-hour irradiance variability is not available. Providing accurate forecasts of the distribution of irradiance within the temporal resolution of NWP models would lead to a new tool for utilities and DSOs to improve operation, planning and resilience of the electricity grid. This effectively increases its hosting capacity and allows for more PV systems to be connected to the grid with less reinforcements.

Different approaches to forecast irradiance variability at high temporal resolution have been the topic of recent research. Most of this work, however, focuses on short lead times, usually within one hour. These use one or more sources of real-time observations of irradiance (Lorenzo, Holmgren, & Cronin, 2015), clouds, either from ground-based observations (Marquez & Coimbra, 2013) or remote sensing (Miller, Rogers, Haynes, Sengupta, & Heiding, 2018), or generated PV power (Nie, Sun, Chen, Orsini, & Brandt, 2020) to forecast irradiance or PV power variability. For an extended overview of the methods and techniques which have been studied, the reader is referred to recent review articles (Chu, Li, Coimbra, Feng, & Wang, 2021) (Ahmed, Sreeram, & Mishra, 2020).

On intra-day and day-ahead scales, post-processing of NWP output provides additional forecasting power (Ahmed, Sreeram, & Mishra, 2020) (Bakker, Whan,

Knap, & Schmeits, 2019). For this forecasting horizon, studies considering intra-hour variability of irradiance are scarce. However, studies are available which investigate the relation between cloud properties and variability (Riihimaki, Li, Hou, & Berg, 2021) or provide methods to estimate variability on reanalysis data or simulations with coarse temporal output. These methods typically involve two steps. First a parametrization of intra-hour irradiance is defined. This can for example be the standard deviation of ramp rates at different time-intervals (Riihimaki, Li, Hou, & Berg, 2021) or parameters describing a bimodal probability density function (PDF) for irradiance at high temporal resolution (Gristey, Feingold, Glenn, Schmidt, & Chen, 2020). Second, the relation between the parametrization and hourly NWP output is investigated, referred to as model output statistics (MOS) (Glahn & Lowry, 1972), typically using regression or machine learning (ML) techniques.

In this study, we propose an algorithm to deliver day-ahead forecasts of 1-minute irradiance variability based on statistical post-processing (SPP) of day-ahead NWP forecasts. 1-Min irradiance observations, spanning 1 year for 17 sites throughout the Netherlands and 2 years for 1 site, are used to parameterize irradiance variability in hourly bins. These parameters both describe the PDF of 1-min irradiance, as well as key variability indicators such as the 95th percentile value of the irradiance PDF. Predictive features from NWP output at hourly resolution are used to train a ML algorithm, so it can convert hourly NWP output into 1-min irradiance variability. The performance of the algorithm is analysed on a test set unseen by the ML model. Results are shown to be geographically generalizable using output from a 2.5x2.5 km² meso-scale model and to be applicable to reanalysis data produced by a 31x31 km² global-scale model. As a reference for the next-generation of weather models, the results are compared to a high-resolution, cloud-resolving Large Eddy Simulation (LES) model at 75x75 m². This method captures the key statistics of 1-minute irradiance variability, instead of attempting to deliver a timeseries of 1-min irradiance directly, which is not predictable. To put it in plain language; not which exact minute the irradiance is high or low, but what the distribution of low and high 1-min irradiance is within a given hour.

The novelty of this work lies in the usage of operationally available NWP output at a day-ahead horizon to predict irradiance variability on a 1-min level. To the best of the authors' knowledge, no previous research has been published achieving this goal. The validity and robustness of the proposed methodology are demonstrated in the following steps. First, the accuracy of the model, when trained on a single location, is examined systematically. Second, the applicability of the algorithm on global-scale

NWP output is investigated. Third, an analysis is performed to quantify to what extent errors in the ML output can be attributed to errors in the NWP forecasts. Fourth, the geographic generalizability of the algorithm is investigated by training the ML model on data of a single location and testing its performance on other sites for which observational data is available. Fifth, while ML techniques are often considered to be black box models, in this work the importance of the features is evaluated on both the level of individual predictions (local) as well as taking all predictions into account (global). Sixth and lastly, the performance of the post-processing method is compared to that of a high-resolution LES model for a case study of four days, to study how new fine-resolution numerical weather models can improve the efficiency and reliability of solar energy forecasts.

The chapter is organized as follows. Section 5.2 describes the data and methodology. Results of the proposed algorithm, as well as comparisons using different input data are presented in section 5.3. Finally, in section 5.4 we discuss the findings in the context of solar PV integration and provide our concluding remarks.

5.2 Data and Methods

This section is structured as follows. First the irradiance observations and Harmonie forecasts are described. Then, the proposed algorithm to statistically postprocess the Harmonie forecasts and predict the intra-hour variability of irradiance on a day-ahead basis is introduced in detail. Finally, the ERA5 data and LES simulation are discussed, which allows the results of the proposed algorithm to be put in a multi-scale context, ranging from the resolution of global NWP models to cloud-scale resolved.

5.2.1 Irradiance observations

Global Horizontal Irradiance (GHI) observations for 18 locations throughout the Netherlands are used in this study. All sites are part of the KNMI network of automatic weather stations, for which the calibration can be directly linked to the World Radiometric Reference (World Meteorological Organization, 2016).

The system located in Cabauw (51°58'13"N, 4°55'35"E) is part of the Baseline Surface Radiation Network (BSRN) (Driemel, et al., 2018). For the Cabauw site (Knap, 2022), GHI is measured at 1Hz using a class A thermopile CMP22 Kipp & Zonen

Pyranometer, classification to ISO 9060:2018 Spectrally Flat Class A (Kipp&Zonen 2019). Data has been used for this location from 2016-04-23 to 2018-02-28.

At the other 17 locations, measurements are obtained using unventilated Kipp&Zonen CM11 pyranometers and sampled every 12s (Mathijssen, Bijma, & Knap, 2018). For these locations, data has been used for the period between 2016-04-01 and 2017-04-05. In the analysis presented in this work, 1-minute averages of all observations are used. An overview of the geographic location of all stations is shown in section 5.2.2, Figure 5.1.

5.2.2 Mesoscale NWP model

The Harmonie-Arome (HA) mesoscale weather model (Bengtsson, et al., 2017) delivers operational forecasts at a 1h resolution, with a horizontal resolution of 2.5 km, which will be used as a feature source in the postprocessing and forecasting algorithm proposed in this work. HA uses lateral boundary conditions from the ECMWF model (ECMWF, 2015). Details on the initialization scheme are given by Bengtsson et al. (2017). The HA model is well-tested, optimized for clouds and under continuous development (de Rooy, et al., 2021). The HA data set consists of atmospheric temperature, humidity, cloud cover at different heights and irradiance, as summarized in Table 5.1. For the analyses throughout this work, hourly outputs are used at grid points closest to the irradiance observations for lead times 24-48h ahead. This time horizon is selected to best resemble the lead times of day-ahead forecasts operationally available. The HA output consists of 65 vertical layers, with lowest level at 12 m and model top at ca 10 hPa. As a pre-processing step, features with a *layers* subscript are aggregated to four groups: low (0-2 km), middle (2-6 km), upper (6 km-TOA) and total (0 km-TOA), where TOA indicates top of the atmosphere. Further details of this step are described in previous work (Bakker, Whan, Knap, & Schmeits, 2019). The parameters originating from HA are indicated by a * in Table 5.1.

Additional features are derived from the time and location of the observations. These consist of the coordinates of the measurement location, minimum Euclidean distance to sea or lake, the cosine of the solar zenith angle, and lastly the sine and cosine components of day of year (Khorasanizadeh, Mohammadi, & Jalilvand, 2014).

Forecasting day ahead 1-minute irradiance variability

Table 5.1: Summary of the features available for the ML algorithm. A * denotes the parameter originates from the HA NWP-model. The subscript indicates if the parameter is available for multiple layers throughout the atmosphere, or at the surface.

T_{layers}^*	Temperature
RH_{layers}^*	Relative humidity
GHI_{surface}^*	Global horizontal irradiance
DIR_{surface}^*	Direct radiation
NCS_{surface}^*	Net clear sky (global) radiation
CC_{layers}^*	Cloud cover
CW_{layers}^*	Cloud water
PW_{layers}^*	Precipitable water
DIST	Distance to sea or lake
$DOY_{\text{sin/cos}}$	Sine or cosine of day of the year (e.g. 1 st of February = 32)
$\text{Cos}(z)$	Cosine of solar zenith angle

Forecasts in general are imperfect. For NWP models, the irradiance forecast in particular is known to be inaccurate relatively frequently. The R^2 score of the hourly mean GHI forecast as delivered by HA, for the locations of the irradiance observations, is shown in Figure 5.1. A difference in performance is found ranging from 0.82 to 0.88. This difference can be linked to different predominant weather conditions. For example, on a typical day a sea breeze moves from south-west in the morning to north-west in the afternoon, providing an inflow of moist air (Arrillaga, et al., 2018). Since most convective clouds form above land, stations near the west coast experience less clouds compared to inland stations. And due to the formation of clouds being difficult to forecast, this results in a larger error in the NWP forecasts for inland stations. The impact of errors in NWP output on the errors of the intra-hour variability forecast will be discussed in section 5.3.3.

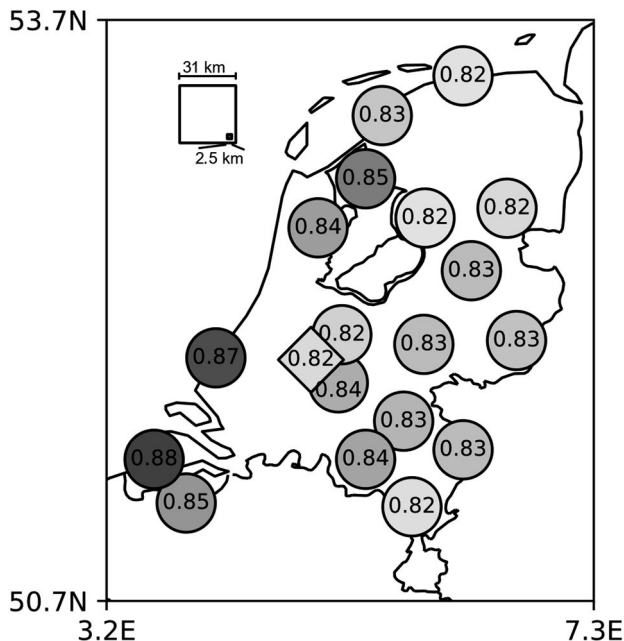


Figure 5.1: R^2 score of hourly average GHI forecast delivered by HA for the locations of the irradiance observations. The BSRN site is indicated by the diamond. In the top left, the two squares indicate the horizontal grid spacing of the global-scale (31 km) and meso-scale (2.5 km) NWP models.

5.2.3 Global scale NWP model

The ERA5 reanalysis model results (Hersbach, The ERA5 global reanalysis, 2020) provide a detailed record of global atmospheric and land surface variables, with hourly output at a horizontal resolution of 0.25 degrees, which amounts to ~ 31 km in the area of research. Data is retrieved (Hersbach, et al., 2018) for the station of Cabauw (as described in 5.2.1), for the same period as the irradiance observations. Parameters were selected to match those available by the HA model as closely as possible and include: 10 m u and v component of wind, 10 m instantaneous wind gust, 2 m dewpoint temperature, 2 m temperature, cloud base height, total/upper/middle/lower cloud cover, mean sea level pressure, mean surface direct and downward short-wave radiation flux, and vertical integrals of kinetic energy, total energy and temperature.

Compared to the mesoscale HA model described in 5.2.2, the ERA5 model results come with three remarks. First, the spatial resolution is 12.4 times coarser. This requires deep convection to be parametrized in ERA5 as opposed to resolved in HA.

Second, since ERA5 is based on assimilation of observations (reanalysis), the outcome can be used as a 'perfect forecast' of the ECMWF model, but not used operationally to estimate the irradiance variability for day-ahead lead times. However, by definition, global-scale models are running for the whole globe compared to limited domain meso-scale models.

The ERA5 model results are used to test the suitability of the proposed methodology to estimate intra-hour irradiance variability based on global-scale model output. If reanalysis data were to provide suitable data to estimate intra-hour irradiance variability, application of the proposed method could be much more widespread compared to using meso-scale model output.

5.2.4 Large Eddy Simulation

A series of large-eddy simulations is performed in which the detail level is so high that individual clouds are resolved, using MicroHH (van Heerwaarden, et al., 2017). Here, the equations of motions are solved under the anelastic approximation. In the configuration in this study, it uses a second-order finite volume discretization combined with 5th order interpolations for the fluxes combined with a 3rd order time-integration scheme. At the surface a no-slip boundary is enforced and at the top free-slip. Lateral boundaries are periodic. For the experiments presented here, MicroHH has been run with its full set of physics including a land-surface model, moist thermodynamics, 2-moment microphysics (Seifert & Beheng, 2006) and the RTE+RRTMGP (Pincus, Mlawer, & Delamere, 2019) radiative transfer solver. The simulation runs at a horizontal resolution of 75 m. All data required to reproduce these simulations can be retrieved from online storage (Kreuwel & van Heerwaarden, Data of manuscript "Forecasting day-ahead 1-minute irradiance variability from Numerical Weather Predictions" submitted to Solar Energy, 2022).

The LES simulation uses forcings of the ERA5 reanalysis dataset (Hersbach, The ERA5 global reanalysis, 2020). ERA5 is used for initial conditions, and during the run of the simulation prognostic values are nudged towards the ERA5 hourly data to prevent drift. To compare the LES results to the statistical post processing method in a meaningful way, four consecutive days are selected for which both the observations show high variability in surface irradiance and the error of the HA GHI forecast is small: 2016-07-13 to 2016-07-16. Due to the use of reanalysis data, this simulation is best considered to be a pseudo-forecast rather than a real forecast. It provides a

best-case reference of which level of accuracy in irradiance variability can be achieved by high-resolution modelling.

To mimic station observations, time series of incoming solar irradiance are recorded at four points in the domain that are sufficiently far apart to ensure statistical independence. The points lie on the corners of a square with edges of 6 km, around the center.

5.2.5 Pre-processing and forecasting

This section describes the data pre-processing steps, and the specific procedure in the training of the machine learning algorithm. A schematic representation of the steps is given in Figure 5.2. The 1-minute irradiance observations are converted into target variables at an hourly interval (section 5.2.5.1). The NWP hourly forecasts are merged as predictive features to this data. The data is split into a train and test set. On the trainset, a ML model (section 5.2.5.2) is trained, using a specific importance weighting scheme (section 5.2.5.3). The trained model is subsequently evaluated on the before-unseen test set using several scoring metrics (section 5.2.5.4)

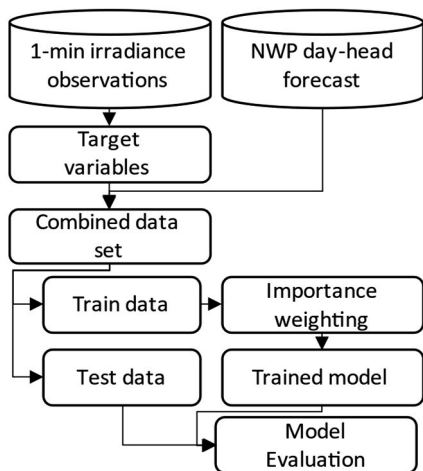


Figure 5.2: Schematic overview of data flow and machine learning procedure. The target variables and NWP day-ahead forecasts have a temporal resolution of 1 hour.

5.2.5.1 Intra-hour irradiance parametrization

This section describes the characteristics which are used to describe hourly irradiance variability. They include: the probability density function (PDF, equation

(5.1)), the 95th percentile (P95) of 1-min GHI and the sum of absolute difference (SAD, equation (5.2)) of 1-min GHI. Additionally, also the hourly mean of GHI is calculated, $\langle G \rangle$. The chosen parametrization of the PDF is known to closely match the PDF of GHI in high-resolution model studies (Gristey, Feingold, Glenn, Schmidt, & Chen, 2020). The PDF assumes a low-irradiance peak described by a normal distribution, and a high-irradiance peak described by a lognormal distribution. Here, the low-irradiance peak corresponds to periods when direct solar irradiance is obstructed by clouds of varying opacity, while high-irradiance relates to clear sky with cloud enhancement. Throughout this work, we will distinguish between the observed PDF, the parametrized PDF (which is the PDF described by the parameters obtained from a least-squares fit to the observations) and the forecasted PDF (which is the PDF described by the parameters obtained from the SPP method). The latter is defined as:

$$\text{PDF}(x) = \frac{w1}{\sigma\sqrt{2\pi}} \exp\left(-\frac{1}{2}\left(\frac{x-\mu}{\sigma}\right)^2\right) + \frac{w2}{(x-\vartheta)s\sqrt{2\pi}} \exp\left(-\frac{\ln^2\left(\frac{x-\vartheta}{m}\right)}{2s^2}\right) \quad (5.1)$$

Here, $w1$ and $w2$ correspond to the area under the low- and high-irradiance distributions respectively, σ is the standard deviation of the low-irradiance distribution, μ is the mean of the low-irradiance distribution, ϑ is a horizontal shift of the high-irradiance distribution, s is the standard deviation of the log of the high-irradiance distribution, which determines the skewness of the high-irradiance distribution and m is the median of the high-irradiance distribution. The fitting procedure of the parametrized PDF to observations consists of creating hourly histograms of GHI and fitting the PDF using least squares optimization implemented in SciPy (Virtanen, Gommers, & Oliphant, 2020). By imposing trivial bounds on the parameter space, physical sensible results are enforced (e.g. $w1$, $w2$ should be greater than 0 and smaller than 1). Alternatively to GHI, using the clear sky index (Marty & Philipona, 2000) was investigated. However, this deteriorated the final results, as this increased weight of moments at the start and end of the day where irradiance is low and therefore of less interest in this study.

To illustrate the comparison between the parametrization and observed PDF, both are shown for two subsequent hours with variable irradiance in Figure 5.3, measured on August 5th, 2016 at the BSRN site Cabauw. For 12-13 UTC, the parametrization matches the observations closely, while for 13-14 UTC, more observations are in

between the high-irradiance and low-irradiance domains. The metric to quantify the resemblance of the PDFs, IQD, will be discussed in section 5.2.5.4, but we note already the median IQD for the entire dataset is 0.019 compared to 0.011 for 12-13 and 0.043 for 13-14 UTC. Observations of GHI between the two irradiance peaks can be attributed to cloud shadows moving over the sensor within the 1-minute observation time, or semi-transparent clouds. While a more complex parametrization, for instance including a third distribution corresponding to medium-irradiance, would be a better fit to the observations, the two-peak parametrization represents the observed distribution well on average while requiring less complexity. Therefore the two-peak distribution is used in this work.

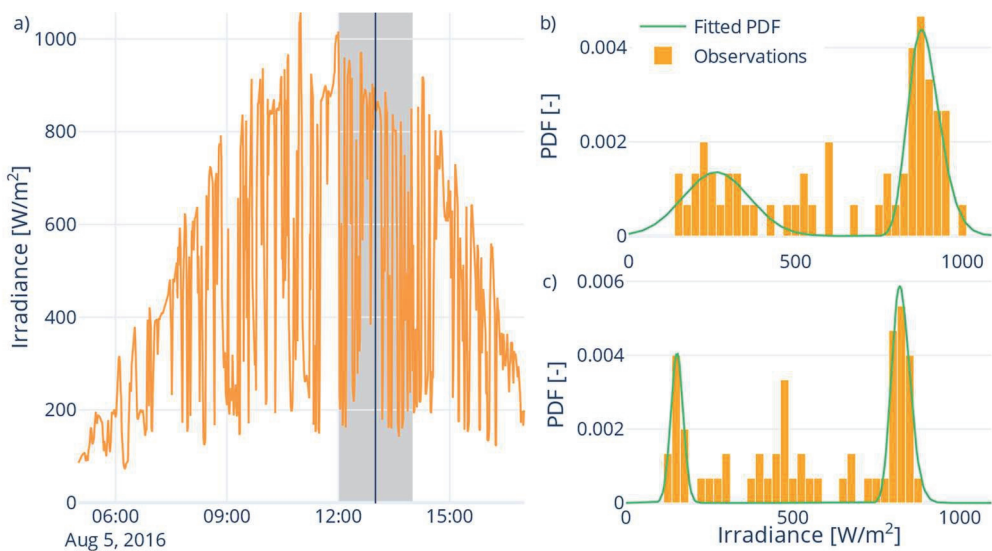


Figure 5.3: Observations of GHI at 1-min resolution are used to fit a PDF. a) daily profile of irradiance at Cabauw, where two hours are marked grey (2016-08-05 12-14 UTC). b,c) Probability density function of observations (orange), compared to the fitted, parametrized PDF (green). b) 12 UTC, c) 13 UTC. For b, the parametrization matches the observations slightly better compared to the average point in the dataset (IQD of 0.011 vs 0.019), while for c it matches a lot worse (IQD of 0.043).

As a measure of intra-hour variability, the sum of absolute difference is calculated as given in equation (5.2). While the PDF provides information on the distribution of intra-hour irradiance observations, the SAD gives information on the fluctuations within that hour. For example, an hour with a single, sharp transition from clouded to clear-sky compared to an hour with broken-clouds and many transitions from clouded to clear-sky have a similar PDF, whereas the SAD is very different.

$$\text{SAD} = \sum_t |\text{GHI}(t) - \text{GHI}(t - 1)| \quad (5.2)$$

In total, for every hour in the dataset, 10 parameters are calculated to describe the intra-hour irradiance observations. These parameters will be the target to predict based on the hourly NWP output. An overview of the parameters and a brief description is given in section 5.3.1, Table 5.3.

5.2.5.2 Machine learning algorithm

The pre-processed dataset is split into a training and test set. A single model is trained for all lead times in the 24-48 hours horizon using this training set. To ensure an appropriate division between test and training set size and for the test set to resemble conditions throughout the year, the test set consists of one week per month. Additionally, we require the test set to include the days selected for the LES case study described in 5.2.4. This resulted in days 13 up to and including 19 of every month to be included in the test set, while the rest is included in the training set. Note that, since the data in this work is a timeseries, ideally all moments in the test set would be at a later moment in time than the training set. Due to the limited data availability a different strategy is chosen. In appendix 5.5.1 we show that the results presented in this work are not influenced by information leakage from training to set, thereby representing the 'true' accuracy of the algorithm.

The added value of accurate estimations of the irradiance PDF is greatest for moments where intra-hour variations are greatest, e.g. sharp and frequent transitions between sun and shade. Such conditions are poorly captured by operationally available NWP models, emphasizing the potential of statistical postprocessing to consider and to reproduce these extreme, but relevant values. However, these bimodal conditions occur less frequently than single-modal conditions for the dataset under research. This can result in a bias towards single-modal conditions, if the postprocessing algorithm is not set up correctly. To mitigate this potential bias, a weight is assigned to hours considered to be bimodal, so the total weight of bimodal training entries matches the total weight of the non-bimodal training entries. For this training dataset, the bimodal weight factor (bwf) was determined to be 8, since the ratio of bimodal to non-bimodal moments in the training dataset is 1:8. Data entries are considered to be bimodal if the area under both the low-irradiance peak and high-irradiance peak exceed 10%, i.e., $w1 > 0.1$ and $w2 > 0.1$.

The relevance of certain target parameters is coupled. For instance, if there is no high-irradiance peak, the parameter describing the skewness of that peak is not important. To incorporate this importance coupling, weights of σ and μ are scaled by w_1 , while weights of s , m and θ are scaled by w_2 during training of the model. An overview is presented in Table 5.2.

Table 5.2: Overview of how sample weight was determined for each target parameter of Eqs. (1) and (2). The bimodal weight factor (bwf) is 8 for bimodal samples and 1 for non-bimodal samples.

Target	Weight
σ, μ	$\text{bwf} * \frac{w_1}{\text{mean}(w_1)}$
s, m, θ	$\text{bwf} * \frac{w_2}{\text{mean}(w_2)}$
$\langle G \rangle, P95, SAD, w_1, w_2$	bwf

The methodology to deliver forecasts of intra-hour irradiance based on NWP model output proposed in this work is agnostic of the machine learning model. This study focuses on the meteorological aspects of the proposed methodology, leaving investigation of the optimum ML model for this task for future work. To predict the intra-hour irradiance parameters, this study uses the ‘LightGBM’ regressor machine learning model (LGB) as a base estimator (Ke, et al., 2017). For each target variable, a dedicated LGB model is trained. These single-output models are combined using the multioutput regressor class defined in scikit-learn (Pedregosa, et al., 2013). The LGB model was chosen since it is computationally inexpensive and allows a relatively high level of interpretability of results, compared to neural networks for example, which have been used in related research (Gristey, Feingold, Glenn, Schmidt, & Chen, 2020). Examining the feature importance provides useful insights in physical drivers for certain model outcomes, as described in section 5.2.5.3.

Ideally, optimal hyperparameters (or “model parameters”) are determined for each single-output model separately. It is to be expected that complexity of the relation between the predictive features and the target parameter is different for each target parameter, and therefore the highest accuracy would be achieved by optimizing the hyperparameters for each target specifically. We found that optimizing over all or a subset of target variables results in under- and overfitting of specific targets. Given the focus of this study, and recognizing that the default hyperparameters yield acceptable results, hyperparameter optimisation is excluded in this work.

5.2.5.3 Feature importance

The feature importance of the forecasted parametrization of intra-hour irradiance is investigated using ‘shapley additive explanations’ (Lundberg, et al., 2020) (Lundberg & Lee, A Unified Approach to Interpreting Model Predictions, 2017). This method allows to assess the impact of individual features on individual model outcomes, as well as provide an overview of the importance of features on the entire dataset.

5.2.5.4 Scoring metrics

To assess the accuracy of the statistical postprocessing method, two metrics are considered. Most metrics in the body of research evaluating irradiance forecasts consider a point-per-point evaluation of the time-series of observations and forecasts, such as mean absolute error and root mean squared error. Since this work concerns estimation of PDFs for which such metrics are unsuitable, other common metrics are used.

The coefficient of multiple determination (R^2) (Draper & Smith, 1981) is calculated for all targets. In addition to how well the individual targets are forecast by the model, the accuracy of the resulting PDF is equally important. Therefore, the integrated quadratic distance (IQD) (Vannitsem, Wilks, & Messner, 2019) is calculated, for which the equation is given in equation (5.3). Here, $F(x)$ is the observed PDF and $G(x)$ is the forecast PDF. Throughout this work, the PDF is discretized in bins of 25 Watt/m², and the integral is calculated as a sum over all elements. The IQD is a proper metric which compares the full distributions, and is a generalization of the continuous ranked probability score (CRPS) (Brown, 1974) (Hersbach, Decomposition of the Continuous Ranked Probability Score for Ensemble Prediction Systems, 2000)

$$\text{IQD} = \int_{-\infty}^{\infty} (F(x) - G(x))^2 dx \quad (5.3)$$

5.3 Results

5.3.1 Intra-hour irradiance forecast, single station

First, the performance of the proposed algorithm is investigated using observations and forecasts at a single location, the BSRN site at Cabauw (NL), as described in section 5.2.1. The SPP method provides a PDF of 1-min irradiance for each hour at a lead-time of 24 hours. Figure 5.4 depicts how the output of the algorithm proposed

in this manuscript relates to 1-minute observations and operationally available NWP output. This day is part of the test-set of the data, unseen by the model during training. The forecast PDF matches the observed 1-min irradiance closely for some hours (e.g. from 13:00 to 18:00), capturing the bimodality of the observations (e.g. 14:00) remarkably. For other hourly intervals the PDF is less accurate, for example between 11:00 to 13:00 the occurrence of high irradiance is overestimated. An investigation to why irradiance is overestimated will be discussed later in the text, referencing Figure 5.5.

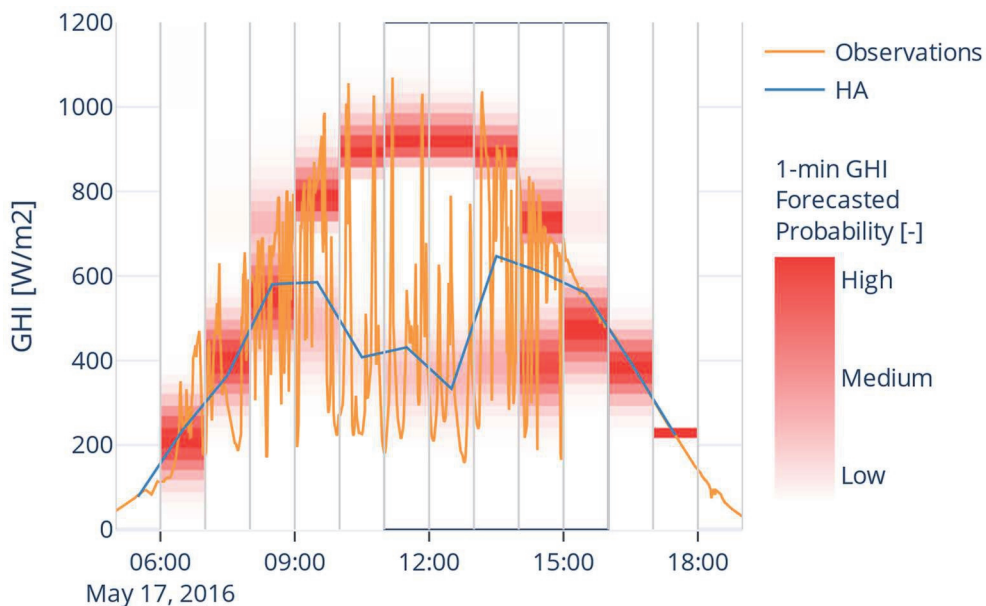


Figure 5.4: Example of day-ahead forecast PDF of 1-min irradiance (red) compared to 1-min observation (orange) and 1-hour NWP output (blue). The rectangle indicates five hours which will be examined in detail in Figure 5.5.

The performance of the proposed algorithm will be quantified on two aspects: in terms of R^2 of each forecasted parameter, and the accuracy of the hourly PDFs resulting from those parameters. Table 5.3 shows the R^2 scores for each target parameter on the test and training sets. As a reference, the R^2 score of the mean hourly GHI forecast of the NWP model is included: $\langle G \rangle_{NWP}$.

Forecasting day ahead 1-minute irradiance variability

Table 5.3: R^2 scores of the algorithm on the training and test set. As a reference, the score of the hourly mean GHI forecast of the NWP model, $\langle G \rangle_{NWP}$, is included.

Target	R^2 train	R^2 test	Description
$\langle G \rangle$	0.94	0.81	Hourly mean of GHI
P95	0.93	0.79	95 th percentile value of GHI
$\langle G \rangle_{NWP}$	0.81	0.77	Hourly mean of GHI as forecasted by the NWP model, included as reference
μ	0.80	0.59	Mean of low-irradiance peak
w2	0.84	0.57	Area of high-irradiance peak
SAD	0.83	0.46	Measure of intra-hour variability
w1	0.69	0.42	Area of low-irradiance peak
σ	0.62	0.31	Standard deviation of low-irradiance peak
θ	0.08	-0.03	Horizontal shift of high-irradiance peak
s	0.03	-0.05	Relates to skewness of high-irradiance peak
m	-0.14	-0.22	Median of high-irradiance peak

Several interesting results can be deduced from the R^2 scores shown in Table 5.3. Firstly, a small difference of the R^2 score of $\langle G \rangle_{NWP}$ on the test and training sets is observed (0.77 vs 0.81 respectively). This indicates that the training set does not resemble the test set perfectly. Secondly, for all targets the difference in performance between the test and training set is significantly greater than the performance difference between these sets for $\langle G \rangle_{NWP}$. This suggests an overfitting of the ML model. Given the focus of this analyses and to limit the complexity of the model training procedure, no further steps are taken to reduce the overfitting. Results could further be improved, for example by using early stopping in combination with cross validation or optimization of hyperparameters, as described in section 5.2.5.2. Thirdly, the R^2 score on the training set greatly differs between targets, ranging from 0.94 to -0.14, with negative values indicating that the mean of the data is a better forecast than the result of the ML model. This can occur if no strong relation exists between the target and inputs or if the ML model was not complex enough to capture the relation between the target and input.

A lack of relation between target and input is to be expected, at least in part. The targets with the lowest R^2 score (θ , s, m) describe the shape of the high-irradiance peak. However, if no high-irradiance peak is present during a certain hour, e.g. during overcast conditions, those parameters are ill-defined. This explains the low and even negative R^2 scores for these parameters. In section 5.2.5.2 it is discussed how to correct for this during training of the model. The coupling between parameters

makes it difficult to assess the performance of the algorithm based on the R^2 score of the model for those parameters. Therefore, the resemblance of three PDFs will be compared; the PDF of the observations, the PDF defined by fitting the parametrization as defined in equation (5.1) to the observations and the PDF obtained from the parameters forecasted by the SPP algorithm.

To explore the PDF resulting from the forecasted parameters, five subsequent hourly intervals are selected from the test set for closer analysis, as shown in Figure 5.5. These hours are selected for detailed depiction based on two criteria. First, a large variability of irradiance is observed, which corresponds to the most difficult conditions for the SPP algorithm to accurately represent in the PDF. Second, some hours are well forecast by the NWP model, whereas other hours are poorly forecast. An evaluation of the performance on the entire test set will be presented later.

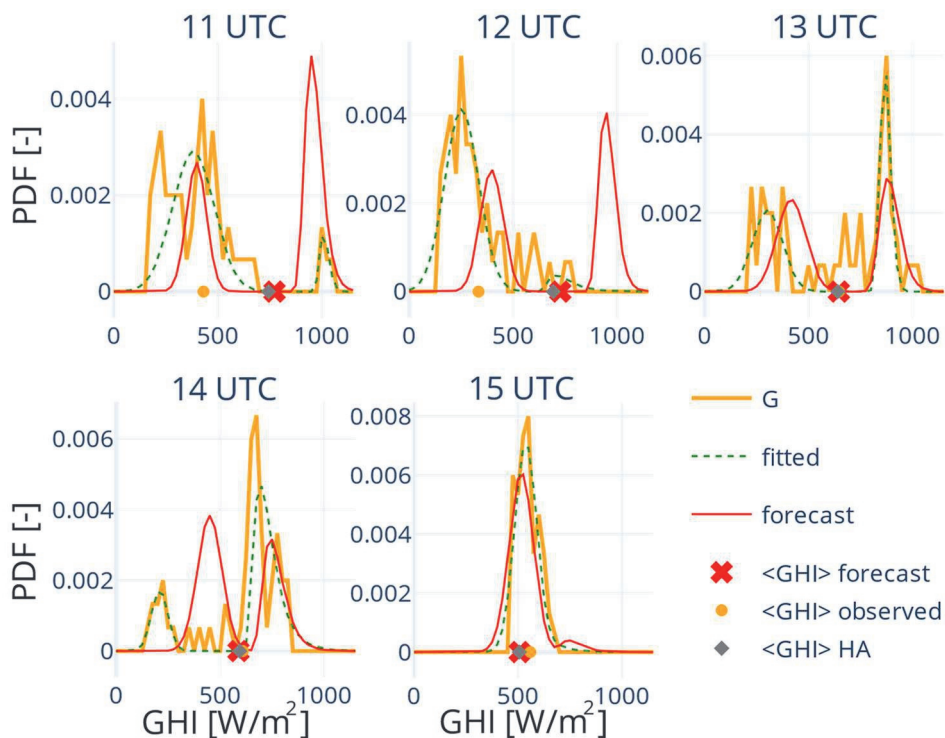


Figure 5.5: Comparison of observed (orange), fitted parametrization (green) and forecast parametrization (red) global horizontal irradiance PDFs for five subsequent hours on 2016-05-17. The hourly mean observed GHI (orange), forecast by the SPP algorithm (red) and NWP input (grey) are shown on the x-axis. The data is part of the test set. The hourly intervals are left-aligned, meaning that hour 11 corresponds to the interval 11:00 – 11:59.

Figure 5.5 shows a detailed inspection of hours 11 to 15 UTC for 2016-05-17, indicated by the rectangle in Figure 5.4Figure 5.3. Here, 'fitted parametrization' refers to the fitting of the parameters describing the PDF using the observations. The ML model is fitted to the training set, and subsequently evaluating the model on the test set yields the 'forecast parametrization'. In addition to the PDFs, the hourly mean of observed GHI, of forecast global radiation by the NWP model and the mean GHI forecast by the algorithm presented in this work are shown on the x-axis.

For 11 and 12 UTC, we find that the algorithm correctly predicted the PDF to be bimodal, but the observations show a much higher probability of low irradiance compared to the model result, and lower for the high-irradiance values. Interestingly, this corresponds to the error in the hourly mean radiation forecast by the NWP model, which is much higher than the observed hourly mean (744 versus 431 W/m²). For hours where the NWP data inaccurately represents the actual weather conditions, a contribution to the error of the PDF derived from statistical post-processing of that data is to be expected. The extent to which errors in the PDF can be attributed to errors in the NWP input will be discussed in section 5.3.2.

For 13 UTC both the hourly mean NWP input as well as the forecasted PDF match the observations closely. The mean of the low-irradiance peak is slightly overestimated, as is the width of the high-irradiance peak. For 13 UTC a small number of irradiance observations occur around 1000 W/m². Interestingly, these observations are not captured by the fitted PDF and are represented by the forecast PDF more accurately. When interpreting the results, it should be noted that the parametrisation of the PDF is a simplification which already introduces inaccuracies.

The results for 14 UTC are comparable to that of 13 UTC, with the exception that the forecast low-irradiance peak is between the actual low-irradiance peak and a section of the high-irradiance peak, which is not covered by the forecast high-irradiance peak. Even though the hourly mean NWP input was accurate, this does not result in a good PDF forecast. A physical interpretation is that in reality, cloud cover existed of small, opaque clouds while the forecast corresponds to larger, less-opaque clouds. Such detailed error attribution to other variables of the NWP input in specific cases should be performed in conjunction with detailed observations of cloud properties, as discussed in existing literature (Nielsen & Gleeson, 2018) (Landelius, Lindskog, Körnich, & Andersson, 2018). Finally, for 15 UTC clear skies are observed and the forecasted PDF matches the observations closely.

To quantify the resemblance of the forecast PDF to the observed PDF, the IQD is calculated as described in section 5.2.5.4. Figure 5.6 shows a boxplot of the individual hourly datapoints, split between the training and test set. As a reference, the IQD of a ‘persistence’ forecast is shown. Here, the observations at day T, hour H are used as a forecast for day T+1, hour H. Two conclusions can be made from this figure. Table 5.3 showed that individual parameters defining the PDF suffered from overfitting. Interestingly, we find that for the SPP results, the performance on the test set is only slightly worse compared to the training set, with a median IQD of 0.084 and 0.12 respectively. This underlines the importance using multiple metrics when evaluating the performance of SPP models. Secondly, results show that the SPP greatly outperforms the persistence forecast, with median IQD values on the test set of 0.12 and 0.25 respectively.

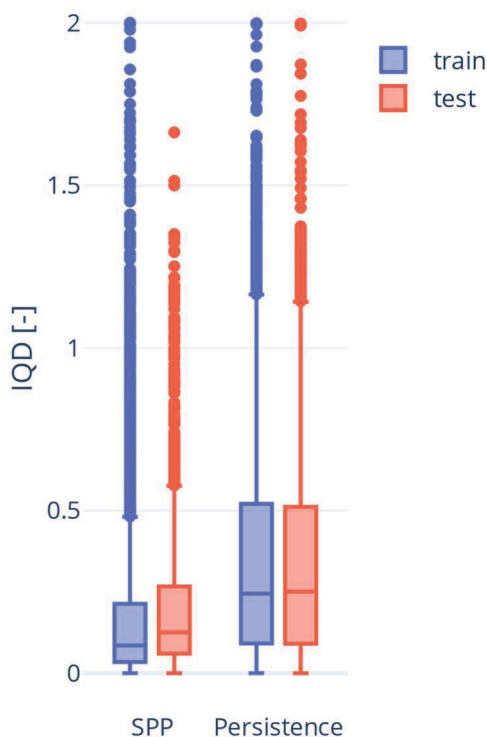


Figure 5.6: Integrated quadratic distance of the forecast PDF to the PDF of the observations. As a reference forecast, the IQD is calculated for a persistence forecast using the observations of one day before.

Next, we consider the 95th percentile of 1-min GHI in detail. In view of applications for grid operators, a forecast of highest intra-hour irradiance is highly relevant. The

95th percentile is considered to be a commonly occurring extreme. We compare results when forecasting the 95th percentile value directly ('Forecasted P95') to forecasting the PDF and deriving the 95th percentile value ('Forecasted PDF'), depicted in Figure 5.7. Additionally, two reference values are included. On the one hand the 95th percentile value is derived from the parametrized PDF ('Parametrized PDF'), which can be considered the smallest possible error using this parametrisation. On the other hand, we include the results obtained using a persistence method, where the 95th percentile value of the observations of today are used as a forecast for tomorrow. We find that for estimating the 95th percentile value of 1-min GHI, forecasting the value directly is more accurate than forecasting the PDF and deriving the 95th percentile value from the PDF. Going left to right, the mean absolute error (MAE) reads 82, 44, 99, 148. Therefore, we recommend including the P95 value explicitly when setting up a SPP routine.

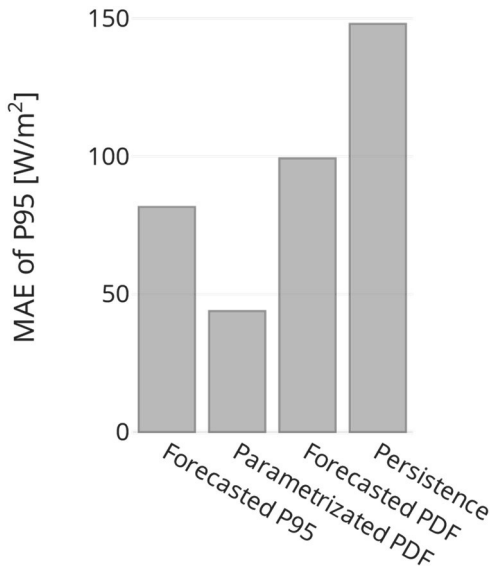


Figure 5.7: Mean Absolute Error of the 95th percentile of 1-min GHI within a 1-hour period. Four methods are compared (left to right): forecasting the P95 explicitly, deriving it from the parametrized PDF (best-case benchmark), deriving it from the forecasted PDF and using a persistence forecast (reference).

5.3.2 Meso-scale NWP forecast versus global scale reanalysis

Next, the suitability of the algorithm on coarse global scale NWP data is tested. The algorithm is applied on the ERA5 global reanalysis model results, of which details are described in section 5.2.3. The results are compared to day-ahead forecasts of the meso-scale HA model, as shown in Figure 5.8.

As a reference, the accuracy of the hourly mean irradiance as computed by HA/ERA5 is indicated by $\langle G \rangle_{\text{nwp}}$. We find that the hourly mean GHI is more accurately computed by ERA5 compared to HA. This is to be expected, as ERA5 is reanalysis data, assimilating observations, whereas HA are day-ahead forecasts.

Interestingly, the forecast PDF using the HA data better corresponds to the observations, as visible from the lower IQD and higher R^2 score of $\langle G \rangle$. Apparently, the higher spatial resolution of the Harmonie data allows for more accurate forecasts of intra-hour irradiance variability, even though the hourly mean is represented less accurate. This could be due to Harmonie resolving larger cloud systems compared to ERA5. These results show the algorithm proposed in this work is suitable to be applied to global scale NWP reanalysis data with an IQD of 0.13 when using ERA5 compared to 0.12 for HA. Validating its performance beyond the geographical scope of this work is recommended for future work to enable estimation of intra-hour irradiance variability on global scales

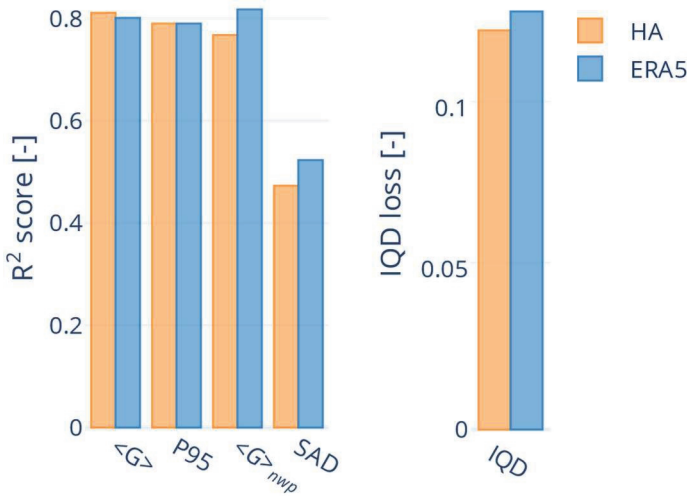


Figure 5.8: Comparison of algorithm results using a meso-scale forecast dataset (HA, orange) and global-scale reanalysis model results (ERA5, blue). (a): R^2 score of most relevant parameters. As a reference, $\langle G \rangle_{nwp}$ indicates the accuracy of the hourly mean GHI as delivered by the NWP model/reanalysis. (b): IQD score of observed PDF versus PDF obtained using the HA or ERA5 as input for the SPP algorithm. Note that for R^2 a higher score indicates better performance, but for IQD this is the opposite.

5.3.3 NWP error attribution

The error in the forecast target parameters is partly due to inaccuracies of the machine learning algorithm, and partly due to inaccuracies of the forecast input values. In this section, we investigate to what extent the error in the output of the SPP is due to errors in the input provided by the NWP model. In particular, we consider inaccuracies of the hourly average GHI forecast for two reasons. Firstly, NWP models are known to show relatively large errors in irradiance forecasts, mainly because that requires detailed knowledge of the instantaneous cloud field. This is indicated by the R^2 of 0.77 in Table 5.3 and well discussed in literature (Larson, 2013). Secondly, the feature importance of GHI is high, which we will describe in section 5.3.5. To attribute the error in the SPP output to inaccuracies of the NWP GHI input, the performance of the SPP procedure is evaluated when the day-ahead forecast of GHI in the HA data is replaced by the observed GHI, while all other inputs remain unchanged. This altered HA model results with a perfect GHI forecast is referred to as HA*.

Chapter 5

The resulting PDF using HA* is compared to the PDF using HA in Figure 5.9, for 4 hourly periods which were also described in section 5.3.1. We find a dramatic increase in performance for hours 11 and 12, which are the cases in which the error in GHI of the NWP input was high. When using HA, a strong overestimation of the weight of the high irradiance peak was found, which is greatly suppressed when using HA*.

For the cases where the error of the forecast GHI was small, results show some differences between using the forecast GHI or the observations, but they are inconclusive in terms of improvement. The height of the high irradiance peak of 13 UTC is predicted less accurately, however, the tail of the PDF (where irradiance exceeds 1000 W/m²) matches the observations even better than the fitted PDF. It is interesting that we find an effect for the hours where GHI was already well-forecast by the NWP model. This can be understood from the fact that when using HA*, the model was also trained on data with the observed GHI instead of the forecast GHI. Therefore, the relations it learned between GHI, other features and the target parameters are different from the original case where forecast GHI was used.

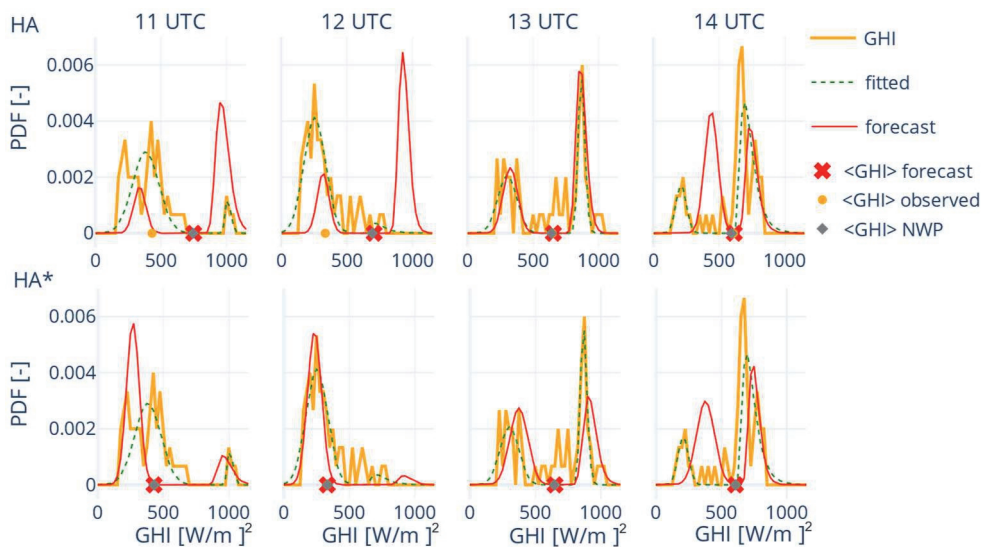


Figure 5.9: Comparison between using the original HA input (top) and the HA* input with perfect radiation forecast (i.e. observed radiation; bottom), for two hours for which the irradiance forecast showed a large error (left), and two hours for which the error is small (right).

Next, the comparison in performance between using forecast or observed GHI is quantified. The R² of P95 and SAD and the median IQD are shown in Figure 5.10. The

R^2 score of GHI is 1 when the observed GHI is given as an input and is therefore excluded from the figure. We find a significant increase in accuracy for all parameters, with an average increase of 0.18 for the parameters shown in Figure 5.10. In particular, the R^2 score of P95 increases from 0.80 to 0.95. Similarly, the IQD is greatly reduced, from 0.12 for HA to 0.063 for HA*. Considering this gain in accuracy is only based on inaccuracies of the GHI forecast, we can conclude that a significant portion of the error in the result of the machine learning algorithm can be attributed to inaccuracies of the input delivered by the NWP (GHI) forecast.

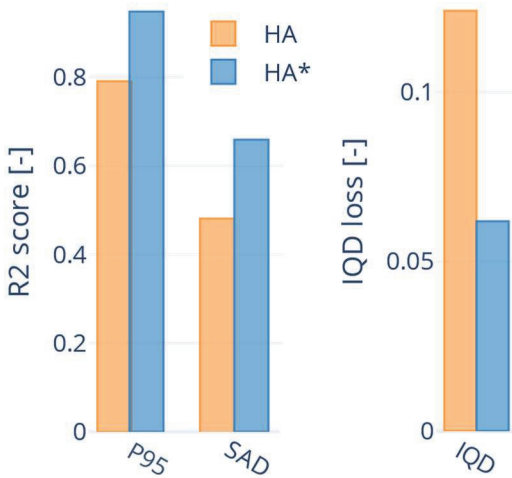


Figure 5.10: R^2 of P95 and SAD (left) and IQD (right), when the original HA input is used compared to HA*, with the GHI forecast replaced by the observed GHI.

5.3.4 Generalizability of result

The generalizability of the proposed algorithm is evaluated in two steps. First, we train the model on data from a single location and apply it to NWP input at different locations. Next, we evaluate the performance of the algorithm after it is trained on data from all locations.

Figure 5.11 shows the median IQD loss of the forecasted PDF on the test set for each station, after the model was trained only on the training data set from the single BSRN station. The differences in IQD loss between stations are relatively small, ranging between 0.11 to 0.15, compared to 0.25 for persistence. Interestingly, we find that accuracy for stations near the coast is lower (the IQD loss is higher), compared to inland stations. This could be due to two reasons, which are

interrelated. The error in the NWP forecast is larger for stations near the coast, for which the meteorological explanations are discussed in section 5.2.2. A larger error in the NWP input can result in a larger error in the SPP output, as shown in section 5.3.3. More fundamentally, the larger error in the NWP forecast indicates that irradiance for these is more difficult to forecast due to local effects. These same effects can also cause the intra-hour variability of irradiance to be more difficult to forecast. An evaluation of the location dependence of the accuracy of the irradiance forecast has been described in detail in previous work (Nielsen & Gleeson, 2018). Summarizing, these small differences between stations for a model trained on a single station imply that the relations learned by the model are similar for the whole of the Netherlands.

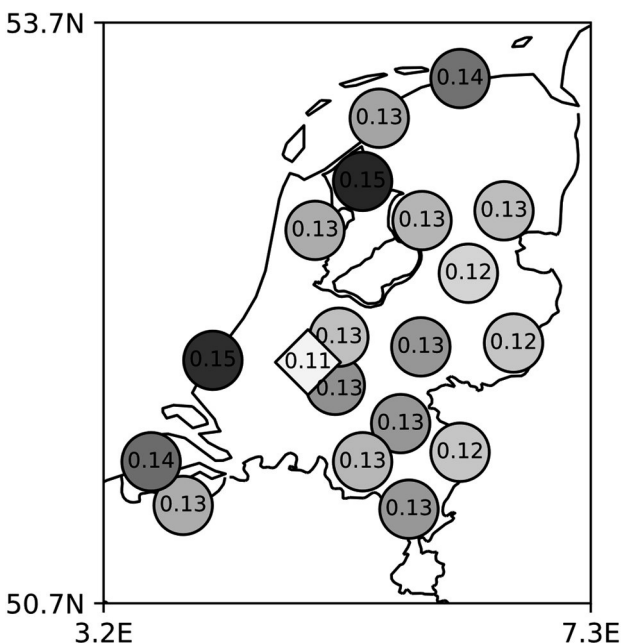


Figure 5.11: Model performance in terms of median IQD loss per station on the test set, with the algorithm trained only on data from the BSRN site. The BSRN station is indicated by the diamond.

Subsequently, the performance of the algorithm is investigated when observations from all stations are included in the training data. This results in a training set with over 12 times as many samples and a geographical span of the entirety of the Netherlands. The resulting R^2 scores and IQD loss for all stations on the test set are depicted in Figure 5.12 as a boxplot. Only targets with a mean R^2 score larger than 0.3 are included in this figure, since the R^2 score is not a suitable metric for all targets

as discussed in section 5.3.1 and for clarity. Interestingly, we find that the impact of including training data from all stations differs strongly between the targets, ranging from an increase of the median R^2 score by 0.06 for μ to a decrease of 0.01 for SAD. A limited increase in model performance can be interpreted as the additional data not providing additional information. This occurs when the training set of the BSRN station for a target is representative for the other stations as well, which could be the case for the P95 target. Additionally, if data from the single station already leads to overfitting for a specific target parameter, e.g. SAD as discussed in section 5.3.1, including even more training data could decrease the performance of the model on the test set. This decrease is also observed for SAD in Figure 5.12. For the median IQD, we find that results improve for each station, with the median of those station medians decreasing from 0.13 to 0.11. Overall, the ML model yields useful results for all stations when trained on just a single station, but accuracy improves when data from all stations is included.

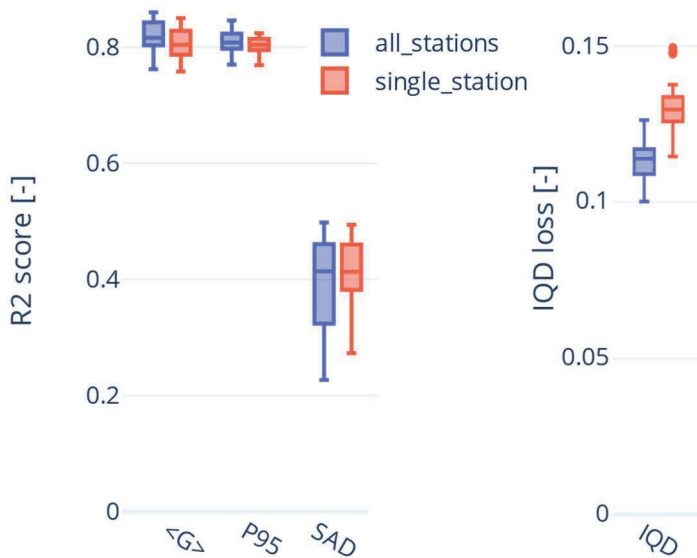


Figure 5.12: Comparison of model performance when the model was trained on a single station (red) or on all stations (blue). The R^2 score (left) is calculated per target, per station, and is depicted for all stations as a boxplot. For clarity only the most relevant parameters are depicted. Similarly, the median IQD per station is depicted as a boxplot for all stations (right).

5.3.5 Predictive value feature analysis

An analysis on predictive feature importance is performed by evaluating the Shapley additive explanation value, as described in section 5.2.5.3. To highlight interesting findings, Figure 5.13 shows the results for the 7 most importance features for targets w1 and w2 during bimodal hours, e.g. when w1 and w2 both exceed 0.1.

We find that the Shapley values are opposite for shared features. This is to be expected from the underlying physics. For example, we find that a high value of NCS decreases the prediction for w1, while increasing the prediction for w2. Since w1 and w2 relate respectively to low-irradiance and high-irradiance observations, it is logical that a higher net clear sky radiation at the surface yields this relation. Similarly, for features positively correlated to clouds, e.g. CW_{total} or CC_{total} , we find an opposite relation.

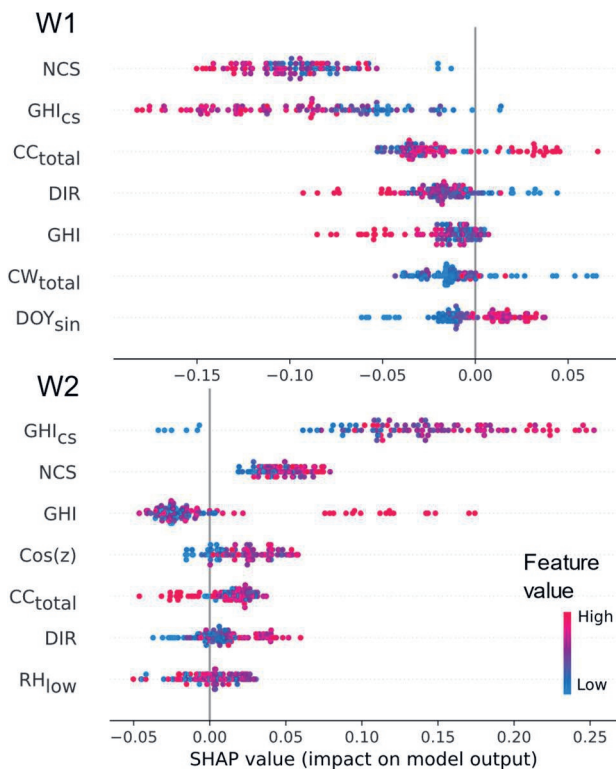


Figure 5.13: Shapley values for the 7 most important features for w1 (top) and w2 (bottom), during bimodal hours. A description of the features is given in Table 5.1.

Using Shapley values, the contribution of each predictor to an individual, forecast datapoint can be examined. The SHAP value indicates the marginal contribution by a feature to the model output, e.g. a SHAP value of 0.1 for a given feature on a given target indicates that the output of the model for that target was increased by 0.1 due to that feature. Figure 5.14 shows the SHAP value for the 6 most important features for target w2, for 2016-05-17 11 UTC. Additionally, it compares the SHAP value when HA* is used as input. As described in section 5.3.3, in HA* the GHI forecast is replaced by the GHI observations. Interestingly, we find that not only the feature weight of GHI itself differs between HA and HA*, but since different paths are taken through the decision trees, also the marginal contribution of other features is changed. Most notably, the contribution of DIR flips from slightly negative to positive. This means that for the original input, where GHI was inaccurately forecast to be high, the value of DIR decreased the forecast for w2, somewhat limiting the error. While when the accurate value for GHI was used, the value of DIR increased the forecast for w2, balancing the contribution of GHI approximately.

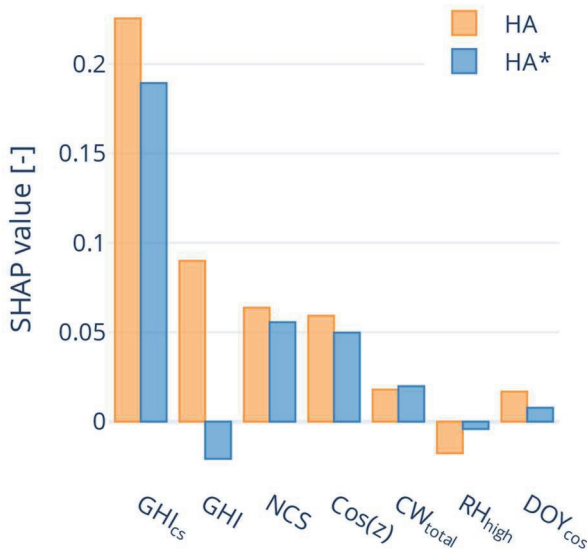


Figure 5.14: SHAP values for the 6 most important features, for target w2 at 2016-05-17 11 UTC, where we compare the original input (HA) versus the experiment when the inaccurately forecasted GHI is replaced by the observed GHI (HA*).

5.3.6 Comparison to LES case study

As a physics-based alternative to using statistical post-processing to enhance NWP output, we investigate the accuracy of computationally expensive, high-resolution LES runs to provide information on intra-hour irradiance variability. Four consecutive days are selected for which both the observations show high variability in surface irradiance and the error of the HA GHI forecast is small: 2016-07-13 to 2016-07-16. A comparison is made in terms of the minute-to-minute irradiance profiles, their hourly PDF, and hourly mean. To give an impression of the processes explicitly resolved in the LES simulation, a horizontal cross section of shortwave downward flux is shown in Figure 5.15. Here, an inverted black-white colour scale is used, so that areas of low shortwave downward flux, which relate to clouds, are indicated as white. To fully appreciate the dynamics which this simulation captures, the reader is referred to the online movie (Kreuwel F. , LES simulation of clouds and radiation for 2016-07-16, at Cabauw, NL [29x29km²], 2022).

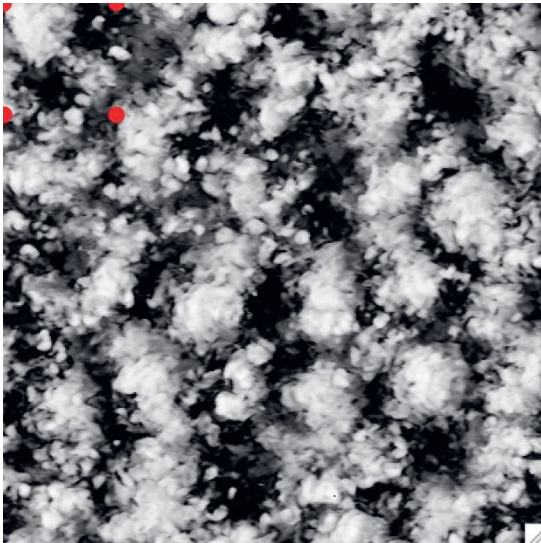


Figure 5.15: Horizontal cross-section of LES simulation at 2016-07-16 10 UTC. The shortwave downward flux is plotted with an inverse, black-white colour scale, so low values are white, resembling clouds. The horizontal size of the domain is 28.8 km, with a horizontal grid spacing of 75 m. The red markers indicate the locations for which individual timeseries of irradiance are shown in subsequent figures.

The resulting time series of shortwave downward flux at two grid points, located 6 km apart, is compared to the observed GHI, as shown in Figure 5.16. From the highly variable irradiance profiles it can be observed that a variety of cloud properties is

present in the case study, with the majority being broken-cloud conditions. Moreover, only small differences exist between the LES profiles at separate locations. The timing of peaks and dips in irradiance is different due to its stochastic nature, but the profiles overall are largely similar.

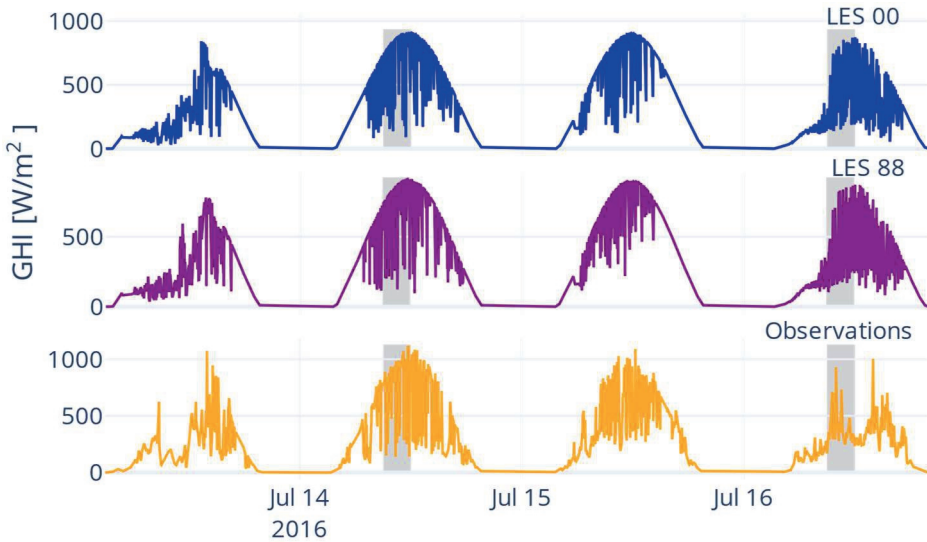


Figure 5.16: Time series of shortwave download flux provided by the LES model for the case study period for two grid points located at top: (0 km, 0 km) and middle: (6 km, 6 km), compared to observed GHI (bottom). Two periods of interest are highlighted in grey. These are depicted in detail in Figure 16.

A more detailed view of the time series and resulting PDF is given in Figure 5.17. For clarity, only a single LES profile is depicted, as the other LES profiles show similar drops and rises, albeit at different moments in time. Two interesting observations can be made related to the absence of 3D radiation effects in the LES simulation. Examining the 14th of July, we find that the LES profile reaches a maximum irradiance corresponding to clear-sky conditions. Opposingly, the observations show higher irradiance before and after each cloud transition, indicating cloud enhancement. However, the PDF clearly shows that high irradiance is captured much less accurately by LES compared to the statistical post-processing method. These findings are in line with previous work on 3d ray tracers (Veerman, Pedruzo-Bagazgoitia, Jakub, Vilà-Guerau de Arellano, & van Heerwaarden, 2020).

Secondly, considering the timeseries for the 16th of July, we observe that irradiance fluctuations in the LES model are much sharper compared to the observations. This can be related to a lack of spatial smoothing of irradiance near edges of cloud

shadows. The PDF shows that for periods of low irradiance, the values are even lower in the LES run compared to the observations, e.g. more dark cloud shadows. For this case, where no irradiance enhancement occurs, the LES model represents the moments of high irradiance very accurately, better than the parametrized PDFs.

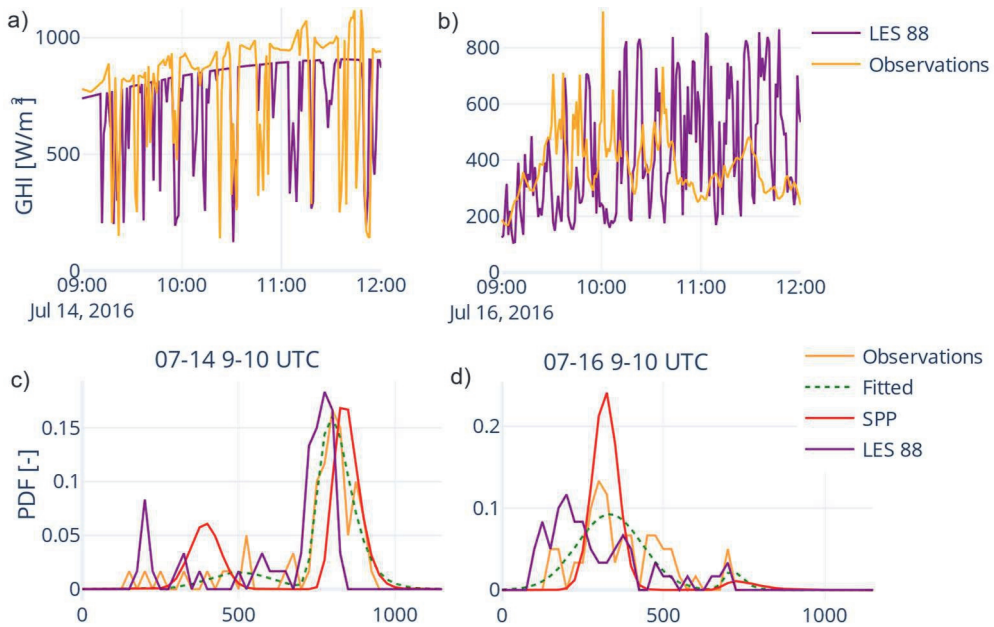


Figure 5.17: Close-up comparison of irradiance timeseries for conditions with few, broken clouds (a) and more and more extended clouds (b). The PDFs for 9 UTC for both days are depicted in c and d, as given by the observations (orange), the fitted parametrisation (red) and the LES simulation for grid point (8, 8) (purple).

In addition to evaluating the time series and PDF of irradiance for selected hours, an analysis is performed on the accuracy of the LES simulation in representing the hourly mean GHI. In addition to the single-grid-point irradiance, also the spatial domain average is calculated. The results are compared to the statistical post-processing algorithm, as well as the Harmonie and ERA5 data, as shown in Figure 5.18. We find that the spatial average GHI of the LES run yields the lowest MAE of 87 W/m^2 , which is very comparable to the MAE of the mean GHI of 4 individual LES grid points of 89 W/m^2 . Interestingly, even for time averages of one hour, the spread of the mean absolute errors at different grid points is substantial, ranging from 83 to 94 W/m^2 . For clarity, the LES results are only shown for a single location. For the other locations results leading to the same conclusions are obtained. While the

timing of drops and rises in irradiance is different between locations, the key statistics concerning irradiance variability are similar.

The statistical post-processing has an MAE in this range, i.e. 92 W/m². The Harmonie GHI forecast and ERA5 GHI are very comparable in MAE of 99 and 100 W/m² respectively. It should be noted that these results are based on a very limited test set of four days, in which the irradiance was highly variable and thereby relatively larger errors are to be expected.

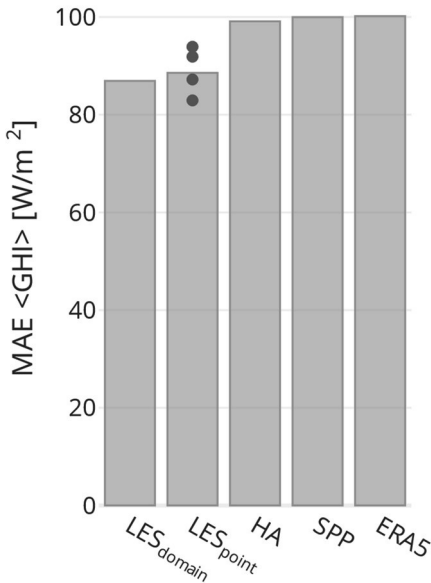


Figure 5.18: Mean Absolute Error of hourly average GHI for the spatial domain average of the LES run, a single grid point of the LES run, the statistical post-processing algorithm, Harmonie forecast and ERA5 reanalysis data. For the single grid point of the LES run, the MAE of the mean of four grid points is indicated by the bar, where the MAE of the individual grid points is indicated by the markers.

5.4 Discussion and Conclusion

Previous, state-of-the-art research showed that it is possible to predict irradiance variability using parametrizations derived from LES simulations (Gristey, Feingold, Glenn, Schmidt, & Chen, 2020) or observed cloud characteristics (Riihimaki, Li, Hou, & Berg, 2021). The work of Gristey et al. (2020) and Riihimake et al. (2021) pioneered predicting day-ahead irradiance variability with the potential to provide a new tool to improve grid operation, planning, and resilience. This work demonstrates a novel

algorithm and methodology capable of delivering day-ahead predictions of 1-minute irradiance variability using operationally available data, thereby moving significantly towards this new paradigm.

5.4.1 Discussion

To further decrease the error of the variability estimation, three pathways are suggested: Improving the NWP forecasts used as input, adding more training data, and/or using alternative ML techniques. These pathways are discussed in detail below.

With respect to inaccuracies in the NWP forecasts used as input, the results in section 5.3.3 show they have a significant contribution to the error of the irradiance variability forecast, increasing the IQD from 0.063 to 0.12. SPP methods are capable of correcting systematic errors in inputs (Bakker, Whan, Knap, & Schmeits, 2019) (Ahmed, Sreeram, & Mishra, 2020). However, the findings discussed in section 5.3.1 confirm that the model cannot correct for errors in the input entirely. Improvements in the accuracy of NWP irradiance products, i.e. forecasts of temporal averages, will therefore in turn improve the estimation of variability within those time periods, as delivered by the algorithm described in this work.

Second, results in section 5.3.4 indicate that accuracy improves when additional training data is used. This can either be resolved using a longer period or increasing the number of stations of which data is used. Third, a different regression or machine learning technique could potentially further reduce the forecasting errors. Comparing different ML techniques was out of scope for this work, as described in section 5.2.5.2. Considering related work on statistical post-processing of NWP output, some researchers report best results using boosting-tree based models similar to the algorithm used in this work, e.g. (Mohammed & Aung, 2016) and (Voyant, et al., 2018). However, others report improved result using different techniques, such as Kalman filtering (Delle Monache, Nipen, Liu, Roux, & Stull, 2011) or neural networks (Pereira, Canhoto, Salgado, & JoãoCosta, 2019). Investigation of alternative ML methods for the forecasting of intra-hour irradiance variability is suggested as a pathway to enhance the accuracy of the algorithm described in this work.

The post-processing results have been compared to a high-resolution LES simulation in section 5.3.6. In this study, no 3-D radiation effects are included. Previous work

has shown the importance of 3-D effects on accurately representing irradiance, in particular in the case of shallow cumulus (Gristey, Feingold, Glenn, Schmidt, & Chen, 2020) (Veerman, Pedruzo-Bagazgoitia, Jakub, Vilà-Guerau de Arellano, & van Heerwaarden, 2020). For future work, including 3-D radiative effects is recommended to provide a more complete comparison between SPP and the next-generation of cloud-resolving weather models.

5.4.2 Outlook

This research has considered variability on a small spatial scale, being a single pyranometer. The applicability of the algorithm can be enhanced by providing forecasts of irradiance variability at larger spatial scales. Fortunately, relations on variability of irradiance or PV generation and spatial scales are known (Lohmann, 2018) (Hinkelman, 2013) (Perez, et al., 2015) (Kreuwel, et al., 2020). Future work could integrate these relations, allowing users of the variability forecasts to tailor the spatial resolution of the output to their specific requirements.

In addition to operational forecasting, estimates of irradiance variability are valuable for reanalysis purposes as well. Short-term irradiance variability events are correlated to voltage problems in the grid (Kreuwel, Mol, Vilà-Guerau de Arellano, & van Heerwaarden, 2021). However, temporal resolutions of 15 minutes to 1 hour are typical for studies on mitigation of PV induced grid issues, for example by means of smart charging of electric vehicles (Fachrizal, Ramadhani, Munkhammar, & Widén, 2021) (Fretzen, Ansarin, & Brandt, 2021) or control of home energy management systems (Javadi, et al., 2020) (Langer & Volling, 2020). Incorporation of minute-to-minute variability in system-integration studies allows for more accurate modelling of the expected grid issues as well as the effectiveness of mitigation strategies. The algorithm described in this paper is equally suited to provide variability metrics for global reanalysis model results, as shown in section 5.3.2.

5.4.3 Conclusion

Accurate day-ahead forecasts of 1-minute irradiance variability are required to enable large scale integration of PV energy generation in terms of grid operation, planning, and resilience. Until now, these predictions at such lead times are not available from operational NWP models. This work presents a novel algorithm capable of predicting 1-minute irradiance variability on a day-ahead horizon, in terms

of its PDF and key statistics. The methodology is based on machine learning to post-process operationally available meso-scale NWP model output. The model is trained using 1-minute irradiance observations. The algorithm is demonstrated to accurately forecast the PDF of 1-minute irradiance variability on a day-ahead lead time using operationally available data. Considering the 95th percentile of the irradiance PDF, most accurate results are achieved by forecasting that value directly, with a MAE of 100 versus 80 W/m² compared to deriving the value from the forecast PDF. We therefore recommend that if a given percentile is of interest, the model is explicitly trained on that parameter as well. Additionally, we find that errors in the irradiance forecast of the NWP model used as an input, have a significant impact on the accuracy of the variability estimation, increasing the IQD from 0.063 to 0.12.

Overall, we find the statistical post-processing procedure to deliver accurate results, which can be generalized throughout the Netherlands. Additionally, the algorithm is shown to deliver similar accuracies when using global re-analysis data as input. In terms of explainability, the algorithm provides comprehensible insights into which features contribute to what extent to the output of the ML model. Integration of this algorithm in existing, operationally available NWP products will facilitate system operators and market parties to proactively balance the grid, thereby effectively increasing its hosting capacity for PV and enabling the next steps in the energy transition.

5.5 Appendix

5.5.1 A: no information leakage due to train/test split

As described in section 5.2.5.2, the training and test split in this study are not strictly temporally separated. This can cause information leakage from the training to the test set, resulting in an overestimation of the performance of the algorithm. Here, we demonstrate that this is not the case for the results presented in this study.

For the BSRN station, almost two years of data is available. The performance of the algorithm is investigated for two cases: for a train/test split with strict temporal separation ('no leakage') and without strict temporal separation ('leakage'), as shown in Figure 5.19. The same test set is used in both cases, days 13 up to and including 19 of every month from March 2017 to February 2018. As a training set, days 1-12 and 20-end of the month are used, either from March 2017 to February 2018 (leakage), or from May 2016 to March 2017 (no leakage).

Forecasting day ahead 1-minute irradiance variability

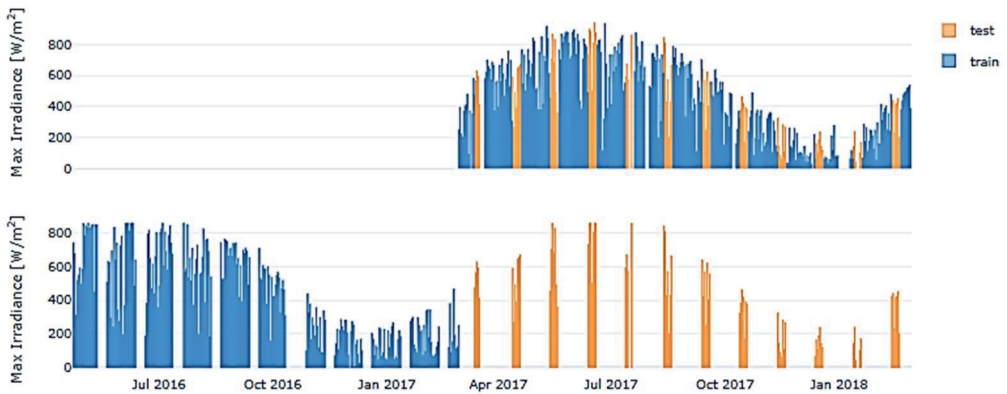


Figure 5.19: Train/test split in the case without strict temporal separation between training and test set (leakage, top) and with strict temporal separation between them (no leakage, bottom).

To test the performance of the algorithm, the IQD is calculated on the test set for both cases. A boxplot of the result is depicted in Figure 5.20, which shows very similar results for the two cases. Based on this comparison we conclude that the method to split the training and test set does not lead to problems due to information leakage or an overestimation of the accuracy of the algorithm.

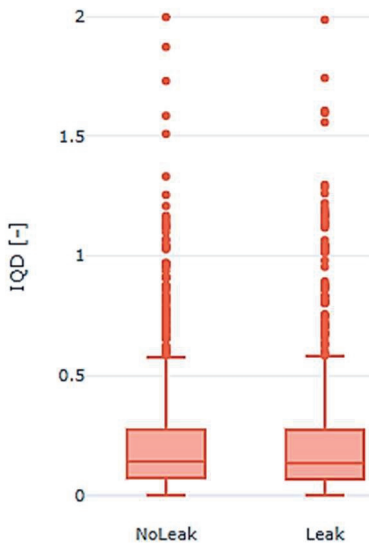


Figure 5.20: Box plot of IQD for the cases with (no leak) and without (leak) strict separation of training and test set.

Chapter 6

Inaccuracy of Meteorological Forecasts in relation to Day- Ahead Congestion Management in the Distribution System

This chapter is based on:

Frank P.M. Kreuwel, Jan Maarten van Doorn, Jordi Vilà-Guerau de Arellano, Chiel C. van Heerwaarden (2022). Inaccuracy of Meteorological Forecasts in relation to Day-Ahead Congestion Management in the Distribution System. In preparation.

Abstract

Accurate predictions are important when grid operators apply congestion management to ensure grid safety. With increasing amounts of renewable generation, the accuracy of the net-load forecast becomes strongly impacted by the accuracy of the underlying weather forecasts. This work presents a novel, generic framework to assess operational predictability of net-load, composed of renewable generation and consumption, on the electricity distribution grid. This framework is applied on a 1-year period of in-service congestion management at day ahead lead times, to quantify to what extent inaccuracies of operational congestion management are caused by inaccuracies of weather forecasts. For the case under investigation, the improvements of wind and solar generation forecasts independently increase the forecasting accuracy. The largest improvement in accuracy is found for perfect wind energy forecasts. Surprisingly, for moments when the grid is under most stress, forecasting accuracy is increased the most by perfect solar generation forecasts. The framework presented here can readily be used by grid operators to determine the predictability of compounded loads in areas of interest and can be used to strategically increase the predictability of a certain resource, for example by installing targeted measurements.

6.1 Introduction

The load on the electricity grid is increasing and becoming more variable. In part due to a growing amount of distributed generation of electricity by renewable resources (International Energy Agency, 2022), and in part due additional electricity consumption due to electrification of demand (IRENA, 2022) and economic growth. For some areas, the electricity grid cannot accommodate these increases and cannot be reinforced quickly enough to keep up with the pace of increase in transport capacity. For these cases, distribution system operators (DSOs) can use alternative solutions to make better use of the existing grid capacity (Hadush & Meeus, 2018).

One of these solutions is active balancing of the load on the grid using flexibility markets (Schittekatte & Meeus, 2020). Here, the DSO forecasts if congestion could occur for a particular contingency. If congestion is anticipated, flexibility is requested from market parties in order to pro-actively mitigate the congestion before it occurs. In case of too high electricity feed-in, market parties can increase their planned consumption, or decrease their planned generation.

An important factor in the cost-effectiveness of day-ahead congestion management is the accuracy of the load forecast. Reducing the forecasting error is the topic of many research studies (Al Mamun, et al., 2020). The net-load consist of the electricity consumption as well as local energy generation. Typically, both the consumption and generation are significantly impacted by the weather, most notably solar radiation in relation to solar PV generation and windspeed in relation to wind energy generation. Meteorological predictions at a local level on a day-ahead timescale are known to be inaccurate (Sánchez, 2022). However, efforts from the forecasting community to reduce the forecasting error ignore inaccuracies of operationally available weather forecasts. Either by using observed weather parameters (Liu, Zhang, & Song, 2020) (Blum & Riedmiller, 2013) or developing implementation-specific weather forecasts based on weather observations (Faraji, Ketabi, Hashemi-Dezaki, Shafie-Khah, & J.P.S., 2020) (Rodríguez, Fleetwood, Galarza, & Fontána, 2018). How inaccuracies of weather forecasts affects the quality of the net-load forecast and cost-effectiveness of congestion management has yet to be researched.

In this work, a novel framework is presented to systematically attribute inaccuracies of congestion management to inaccuracies of meteorological forecasts. This framework is subsequently applied to a one-year case study where operational congestion management was executed on a local level. The case study is located

around a municipality in the Netherlands, with household/commercial demand, generation for solar and generation from wind in the same order of magnitude. For this case we find the error in the windspeed prediction to cause a larger error in the net-load forecast compared to the solar radiation prediction. Moreover, the combination of a perfect wind and perfect solar forecast yields an approximate equal reduction of the error of the net-load forecast to the sum of the individual improvements.

6.2 Data:

The data used in this work spans one full year, from 2021-02-25 to 2022-03-30. During this period, the DSO performed congestion management on the substation under investigation. This section provides a description of the congested region, as well as an overview of the data used in this work. In addition to the data discussed in detail, day-ahead electricity prices (ENTSO-E, 2022) and typical consumption profiles (NEDU, 2022) are used as external predictors.

6.2.1 Operational Congestion Management case description

The congestion area under investigation is located near the municipality of Hallum, the Netherlands (Figure 6.1). The capacity of the substation is 8.2 MVA, while the total installed capacity for power feed-in is 17.3 MW. Congestion only occurs due to excess generation, when the energy generation minus consumption exceeds the capacity of the substation. 4705 Residential customers are connected to this substation, of which 1356 are registered to have small-scale wind (0.6 MWp) or solar PV (7.7 MWp) generation. Also commercial installation of wind (5.7 MWp) and solar (3.3 MWp) are connected to the substation. An overview of the peak load per primary energy source is given in Figure 6.2, with the cut-off between residential and commercial being at a connection capacity of 100 kVA. A full technical specification of the congestion area is given by the DSO (Liander N.V., 2021). Notably, the peak capacity for energy consumption, generation by solar and generation by wind are within the same order of magnitude, resulting in a diverse energy mix. For this substation, congestion occurs when there is both wind- and solar energy generation, in combination with small energy consumption. These conditions can result in voltage variations outside of safety limits at end-users, as well as currents through

grid components exceeding their operational limits. Due to the problem being both voltage and current related, both short as well as long periods of congestion are problematic.

To mitigate foreseen congestion, the DSO has a contract with a commercial wind park with an installed capacity of 5.25 MWp, to curtail a given number of turbines on request. The park operator will receive a fixed compensation for every curtailment action, as well as a compensation based on loss of generation. Mitigation requests are send on a day-ahead basis, and in real-time if grid safety is at risk. Typically, if a mitigation request is send, 1 to 3 of the 7 turbines are curtailed, resulting in a maximum curtailment of 0.75 MW per turbine. The 10kV cable connecting the wind park to the substation has active power measurements at the substation. Since curtailment reduces the yield of the wind park by a fraction, the curtailed energy as well as the load that would have occurred if no curtailment was applied, can be calculated (section 6.2.3).

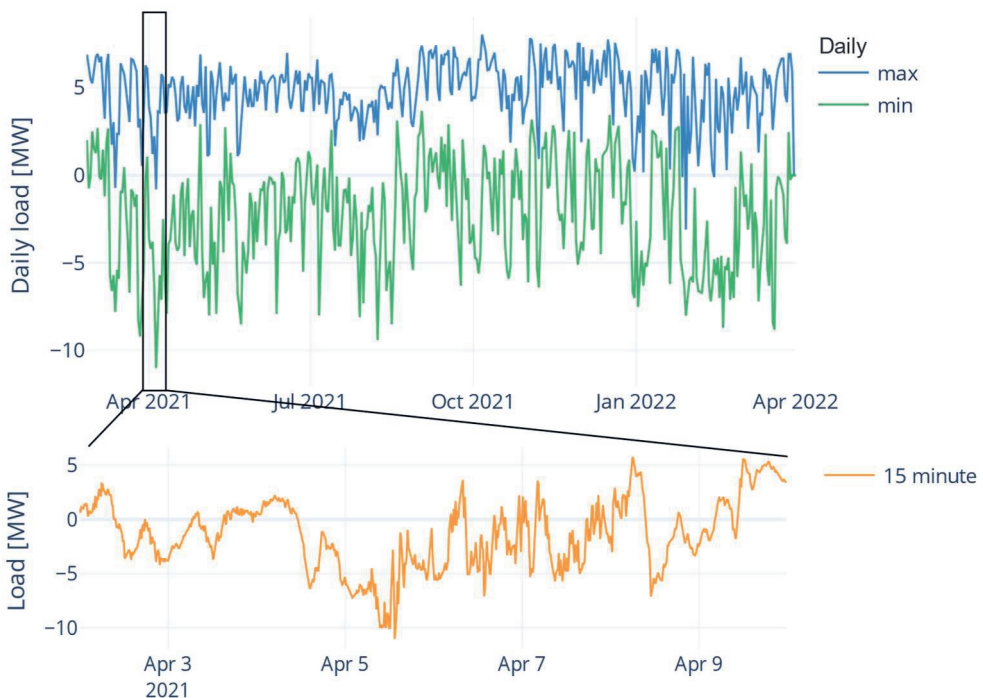


Figure 6.1: Timeseries of daily minimum, maximum observed load on substation Hallum (top), and a detailed overview of the week with the most extreme load (bottom). Negative extremes (net feed-in) can reach the technical limits of the substation from the end of March up to the end of August while positive extremes (net consumption) stay well within the available capacity.

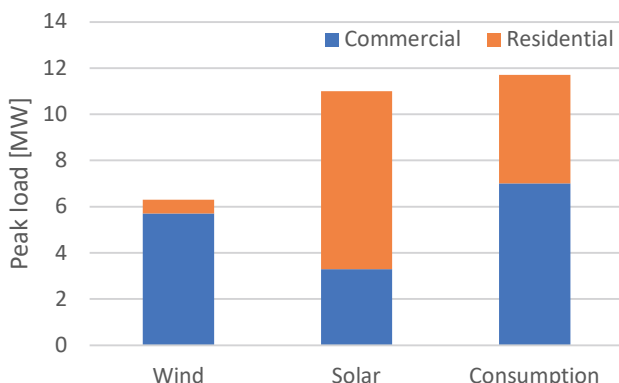


Figure 6.2: Overview of peak load per primary energy component. The cutoff between residential and commercial as at 80A or 100 kVA.

6.2.2 Operational weather forecasts

The Harmonie-Arome (HA) mesoscale weather model (Bengtsson, et al., 2017) delivers operational forecasts at a 1h resolution, with a horizontal resolution of 2.5 km, which will be used as a feature source in this work. The HA model is well-tested, optimized for clouds and under continuous development (de Rooy, et al., 2021). The HA data set consists of 12 parameters such as windspeed, at 100m, global horizontal irradiance and air temperature. For operational reasons, the forecasted value from the latest model run are used, corresponding to a lead-time of 0-6 hours. During this work we will use these weather feature to predict the net-load on a 24 hours lead time. We recognize that during normal operations, the accuracy of the weather predictions at a day-ahead lead time will be lower, however previous work has found that this decrease is small (Sánchez, 2022).

6.2.3 Reference generation profiles (‘perfect forecasts’)

Reference generation profiles of wind and solar energy are constructed, which are used as proxies for perfect meteorological forecasts. The wind generation profile is based on the active power measurement at the substation, on the 10 kV bay of the cable connecting the wind park. To correct for congestion mitigation, which effectively turns off a number of turbines, the observed generation is scaled by the fraction of operational turbines, as given by equation (6.1).

$$P_{wind\ ref} = P_{wind\ obs} * \left(1 - \frac{n_{turbines\ curtailed}}{n_{turbines}}\right) \quad (6.1)$$

Here, $P_{wind\ ref}$ is the reference wind generation, $P_{wind\ obs}$ is the observed wind generation at the substation, $n_{turbines\ curtailed}$ is the number of curtailed wind turbines and $n_{turbines}$ is the total number of wind turbines.

The total solar generation behind the substation is not measured directly. Instead, measurements of a commercial, 4.8 MWp solar park at a distance of approximately 10 km are used. Three imperfections in the references generation profile are noted. First, solar generation profiles of residential PV panels typically differ from commercial solar parks with respect to orientation and inclination. Panels of PV parks are generally oriented due south under ideal inclination angle, whereas the orientation of PV panels on household rooftops is constricted by the orientation of the rooftop itself. Secondly, peaks in generation under broken cloud conditions are more spread-out for residential PV generation over a larger geographical area compared to a single PV plant. Thirdly, the distance of 10 km of the PV park with respect to the area under investigation means brief peaks and dips in PV generation, related to clouds, can occur at different timings. No additional steps to account for these effects are taken in this work.

In order to quantify the inaccuracy of the operationally available weather forecasts at day ahead lead times, the most relevant forecaster meteorological parameters are compared to the reference profiles. Figure 6.3 shows a comparison between the wind and solar reference profiles and windspeed at 100 meters and GHI respectively, for the full dataset under investigation. In first order, a linear relation is expected for PV generation as a function of radiation, while a sigmoid is expected for wind generation as expected for windspeed. These relations are included in the figure, indicate that the current state-of-the-art, operationally available weather forecasts leave room for improvement. The constructed generation profiles provide a best-case reference to what would be achievable using perfect weather forecasts.

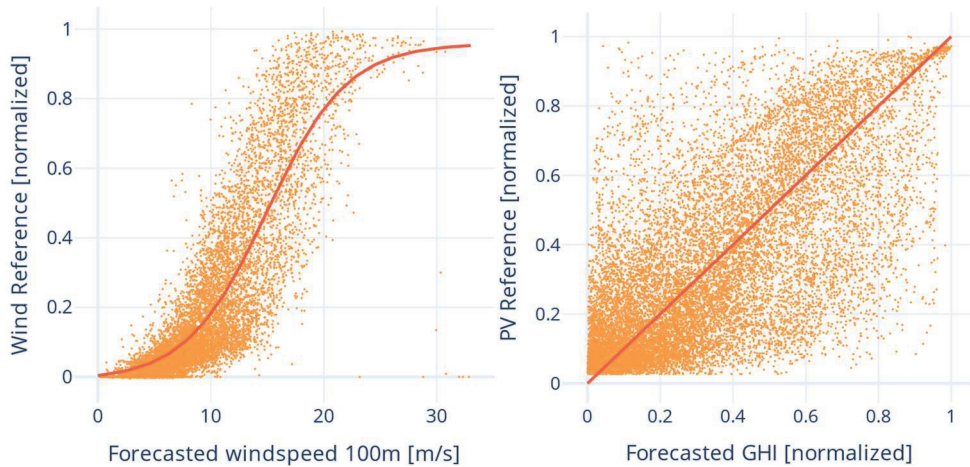


Figure 6.3: Comparison of meteorological forecasts and wind (left) and solar (right) reference generation profiles, using hourly averages. The first order approximations (sigmoid, linear respectively) are fitted in solid.

6.3 Method:

This section presents the methodology used to pre-process the input data, train a machine learning model and generate back-testing results. The steps are outlined in Figure 6.4, which are discussed into more detail in this section. On a high level; the measured load is corrected with the activated mitigations, in order to calculate what the load on the grid would have been if no mitigating actions would have been taken (section 6.3.1). Weather predictors are added (section 6.2.2) and predictive features are generated (section 6.3.2). Depending on the scenario being back tested, one or more reference generation profiles are joined to the data (section 6.2.3). The prepared input is used to generate a back test using 57-fold cross validation (section 6.3.4), using a machine learning algorithm (section 6.3.3). The full code used to perform the analysis performed in this work, as well as the data used, are published as open source (Kreuwel, InaccuraciesMeteorologyCongestionManagement, 2022).

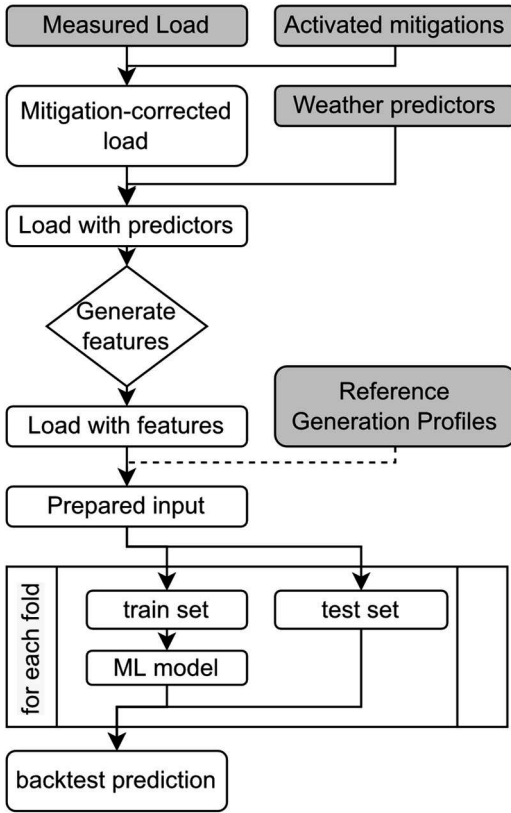


Figure 6.4: Flowchart of procedure used to prepare the data and generate the back-test. Data use as input is marked grey, while intermediate or output data is white.

6.3.1 Correcting load for activated mitigations

For the area under investigation throughout this work, congestion management was performed by the DSO, as discussed in section 6.2.1. Based on day-ahead forecasts, congestion mitigations were performed, resulting in a lower load on the grid. To assess the accuracy of the forecasts and predictability of the load, the observed load has to be corrected for the activated mitigations. Since the curtailment consists of turning off a fixed number of wind turbines but never all wind turbines, the mitigation corrected load by equation (6.2).

$$P_{(mitigation\ corrected)\ load} = P_{obs\ load} - P_{wind\ obs} * \frac{n_{turbines\ curtailed}}{n_{turbines}} \quad (6.2)$$

Here $P_{\text{(mitigation corrected) load}}$ refers to the load of no mitigations would have been performed and $P_{\text{obs load}}$ indicates the load observed at the substation. Since this work mostly considers the mitigation corrected load, this is referred to simple as 'load'. Over the period under investigation, mitigations were activated on 16 days, with curtailments ranging between 1 to 3 out of 7 wind.

6.3.2 Feature engineering

In addition to external predictors, features are generated based on the load time series. In total, 51 features are generated using the 'apply features' module of the open source OpenSTEF python package (OpenSTEF, 2022). These features either relate to calendar information (e.g. holiday, day of week, month), lagged load (e.g. load at T-1 day) or are derived from weather features (e.g. direct normal irradiance or global tilted irradiance, derived from the radiation forecast). A full overview of the used features is available in the data set published with this work.

6.3.3 Machine learning model

To learn the relation between (mitigation corrected) load on the grid and the predictors and features, this work uses the 'XGBoost' regressor machine learning model (Chen & Guestrin, 2016) as a base estimator. Which is a decision tree based model. This type of model is also used by the DSO during operations and was selected since it is computationally inexpensive, allowing for frequent online re-training, and relatively high level of interpretability of results. Since this work focusses on the impact of forecasting errors due to inaccuracies of the meteorological forecasts, finding the optimum type of machine learning model or best set of hyperparameters is placed out of scope and the default values are used.

To prevent overfitting, a dataset used for training the model is split into a train and validation set in a ratio of 0.85:0.15. Training of the model is halted when the performance of the model over the validation set does not improve for 10 subsequent rounds.

6.3.4 Back-testing framework

During normal operations at the DSO, the machine learning model is re-trained at least once every week, and more frequent if forecasting errors surpass a certain threshold. To replicate this frequent online training, K-fold cross validation is used (Geisser, 1975). Here, the total dataset is split into 57 parts, each spanning 1 week. For each fold, 56 weeks are used to train a model, for which part is used as validation. The resulting model is used to make a prediction for the 1 week left out-of-sample. These out-of-sample predictions combined are referred to as the back-testing result. The back-testing procedure is performed using the publicly available `TRAIN_MODEL_AND_FORECAST_BACK_TEST` module of the OpenSTEF package (OpenSTEF, 2022).

This procedure is repeated for four scenarios; incorporating no reference generation profiles (referred to as 'original_weather'), a single reference generation profile ('perfect_solar' and 'perfect_wind') and both reference generation profiles ('perfect_wind_solar').

6.4 Results:

6.4.1 Operations versus back-test

The representativeness of the back-testing framework is assessed by comparing one year of operational forecasts, made at a lead time of at least 24 hours, with the forecasts generated by the backtest framework. Figure 6.5 shows the probability density function of the forecast error for the operational forecasts and back-testing framework.

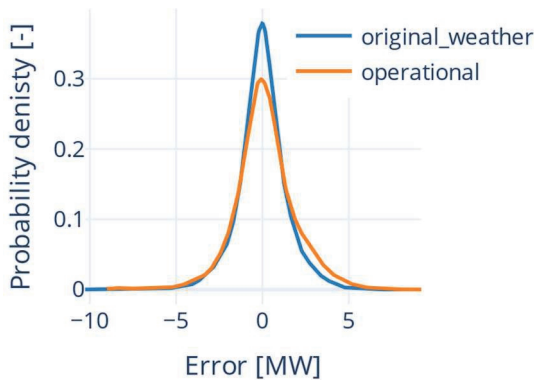


Figure 6.5: Probability density function of the forecasting error of the operational forecasts (orange) and backtest framework (blue).

For negative forecasting errors, e.g. where the realisation is lower than the forecast, we find very similar results. For positive forecasting errors, we find that the back-testing framework achieves a higher accuracy compared to the operational forecasts. A comparison of sections of the timeseries is shown in Figure 6.6. During operations, temporary unavailability of the measurements can lead to structural inaccuracies in the forecast. Section A shows such a period. Interestingly, after the measurement availability was recovered, the forecast matches the observations closely again. Such periods result in positive forecasting errors. As desired, these types of errors are not reproduced by the back-testing framework. For other periods we find that the back-testing framework and operational forecasts closely match each other, alternately achieving the highest accuracy, as depicted in section B of Figure 6.6. Concludingly, while data unavailability leads to additional inaccuracies in operations, the back-testing framework is found to well-represent the accuracies achieved under normal operations.

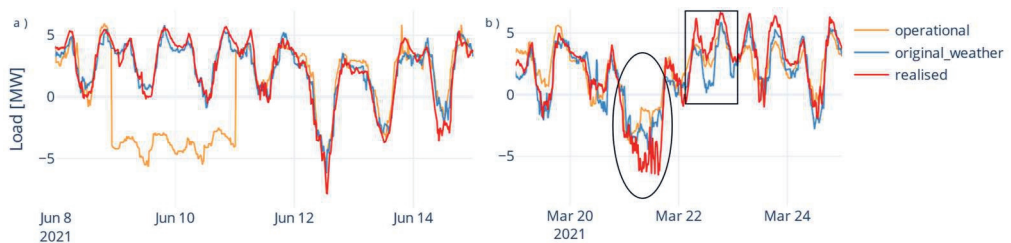


Figure 6.6: Time series of operational forecasts (orange), back-testing results without reference profiles (blue, original_weather) and realised load (red). a): period where a temporary lack of measurements caused inaccuracies in the operational forecasts. b): Section where the operational forecast has a lower (circle) and higher (rectangle) accuracy compared to the back-testing framework.

6.4.2 Improvements due to reference generation profiles

By selectively including the reference profiles, discussed in section 6.2.3, as predictive features to the back-testing framework, it is possible to quantify which amount of the forecasting error is caused by inaccuracies of meteorological forecasts. A comparison is made between the operational forecasts, the original back-testing framework indicated by ‘original weather’, and the back-testing framework including one or both of the reference generation profiles indicated by ‘perfect wind/solar’. The mean absolute error for each case, considering the entire dataset is shown in Figure 6.7. Compared to the original weather, the reduction in MAE of perfect wind is more than double that of perfect solar. This indicates that errors in the meteorological parameters are a much bigger source of inaccuracy compared to the meteorological parameters related to solar energy. Interestingly, reduction in MAE of the combination of perfect wind & solar matches the sum of the individual reductions, suggesting the improvements of including the reference generation profiles to be independent.

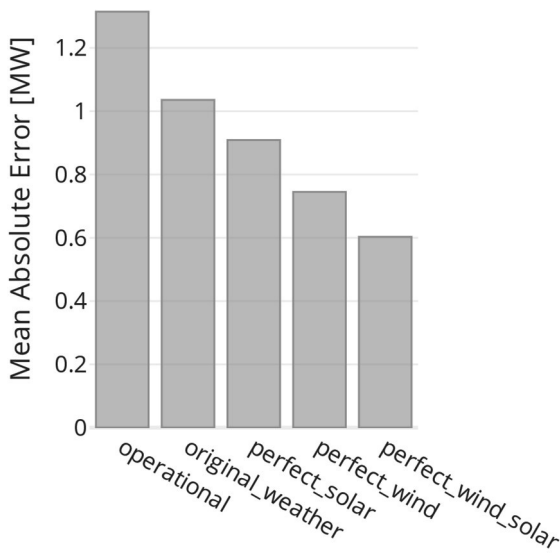


Figure 6.7: Mean Absolute Error of the back-testing framework when selectively including reference generation profiles as predictive features.

6.4.2.1 Error reduction on global scale

Considering the errors resulting from the different feature sets into more detail, Figure 6.8 depicts the diurnal cycle of the mean absolute error. Since the most relevant time-period for this case study is April to August, as described in section 6.2.1, only data from this time period is included in this figure. A number of interesting observations can be made. Firstly, comparing the operational forecasts to ‘original weather’, an almost constant difference is found over the day. This corresponds with the findings of Figure 6.6, where temporary unavailability of measurements results in a constant offset of the forecast. Secondly, the biggest improvement with respect to ‘original weather’ is found at night times for ‘perfect wind’, while at day times the improvement of ‘perfect solar’ slightly exceeds that of ‘perfect wind’. As one would expect, ‘perfect solar’ shows no improvement at night times at all. Thirdly, while the MAE of ‘perfect wind solar’ is greatly reduced compared to ‘original weather’, it remains greatest around noon. This could be a result of the imperfections in ‘perfect solar’ discussed in section 6.2.3, or due to the energy consumption around noon being most uncertain or a combination of both.

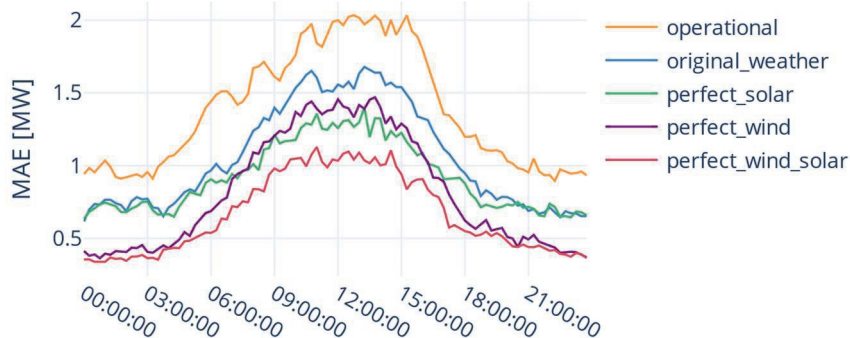


Figure 6.8: Diurnal cycle of mean absolute error during the time range congestion can occur (Apr-Aug).

6.4.2.2 Conditional error reduction

Since the forecasts are used by the DSO in the context of congestion management, investigating the accuracy of the forecasts under two conditions is of particular interest; namely for cases where the forecast error is large, and for cases where the unmitigated load is close to the congestion limit. The forecast errors with an absolute value greater than 2 are defined as large, and unmitigated load lower than -8 are defined as close the congestion limit.

The mean absolute error under the two conditionals for each forecast set is presented in Figure 6.9. Notably, for the condition of large forecasting error, the MAE

of the operational forecasts is found to be lower than the original weather. This can be expected, since the generation of the forecasts, and therefore the forecasting error at any given time, is a stochastic process. Selecting only moments where the original weather yielded large errors, can result in a lower error for the operational forecasts, even though the error over the whole dataset is larger.

Under the condition that the forecast error is large, the reduction in MAE of perfect wind exceeds that of perfect solar. Interestingly, under the condition of load close to the congestion limit, it is the other way around. This shows that even though the highest reduction in forecast error is achieved by improving the wind forecast, the error of the solar forecast is most important for the moments the grid safety is most at risk.

Two explanations for this observation are provided. First, this effect relates to high solar generation being less predictable than high wind generation, as can be seen from Figure 6.3. It is recognized that the load on the grid of the area under investigation is most extreme when there is the most net feed, which requires a combination of high solar and wind energy generation as well as low energy consumption. In other words, only if solar generation is high, the load can be extreme. Meso-scale weather models are known to have difficulty in accurately forecasting broken-cloud conditions, while such conditions can result in high solar energy generation (Kreuwel, Mol, Vilà-Guerau de Arellano, & van Heerwaarden, 2021). Secondly, wind energy generation is known to be high at night and in winter, which are periods for which solar generation is negligible. A large part of the error reduction for the wind energy occurs at moments at which plenty grid capacity is available, as can be seen from Figure 6.8.

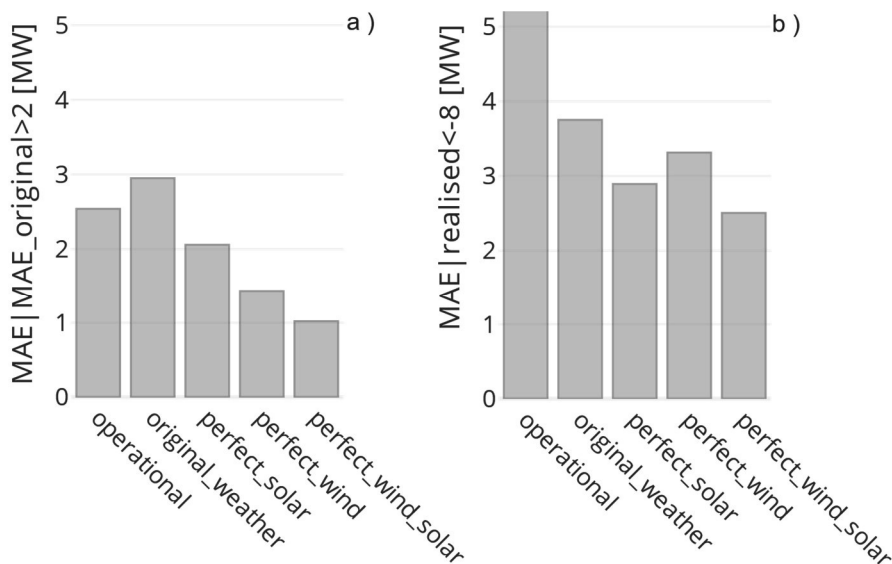


Figure 6.9: Conditional mean absolute error when the forecasting error is large (A) and the unmitigated load is near the congestion limit (B).

6.5 Discussion and outlook

As renewable generation impacts the load on the grid to an increasing extent, there are growing risks to the stability and safety of the grid. It is expected that large amounts of local, renewable generation require active balancing by Transmission and Distribution System Operators on a day-ahead basis. To do this effectively, quantifying and attributing uncertainties in load forecasts is of key importance. This work describes and provides a ready-to-use method to answer exactly these questions. Moreover, the outcome of the analysis can be used to strategically increase the predictability of a certain resource, for example by installing specific additional types of measurements.

The back-testing framework proposed in this work was shown to deliver forecasts closely resembling output during normal operations. Disturbances which can occur during operations and are likely to reduce accuracy, such as unavailability of measurements, predictors or IT infrastructure, are by design not incorporated in this framework.

K-fold cross validation on time-series data, as used in the back-testing framework, has some theoretical flaws relating to information leakage, meaning information of

the test-set is partly available to the model during training. Two design choices in the set-up used for the back-testing framework proposed in this work limit the potential impact is limited. First, only lagged features of historic load are used no higher order features or lagged meteorological forecasts. Secondly, the folds are grouped into consecutive blocks of one week, restricting the potential leakage even further. As a result, no evidence of the theoretical problems is found throughout this work. This finding is in agreement with an extensive review article, which found no consequences of the theoretical flaws for six model selection procedures (Bergmeir & Benítez, 2012). For future work, a blocked-form of cross validation could be used, where only blocks previous to the block under test are used for training the model. This would require a longer time span of data however.

Recognizing that the results presented in this work are highly specific to the dataset under investigation, they do allow to attribute the operationally observed inaccuracies to be attributed to four distinct sources; Operational unavailability of data, inaccuracies in the solar forecast, inaccuracies in the wind forecast and 'other', which consists of at least inaccuracies of the demand forecast and inherent unpredictability. An overview of their relative contributions is shown in Figure 6.10. When considering the inaccuracies of other sources, it would be expected to resemble the predictability of substations without renewable generation. For the substation under investigation, this results in a MAE of 0.6MW, which is 7% of the capacity of the substation. This matches values found in other work on similar levels of aggregation (Peng, et al., 2019).

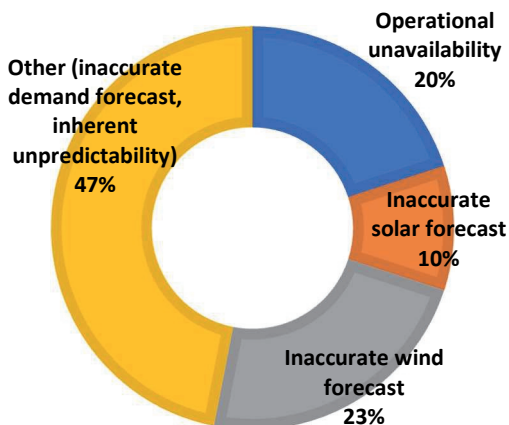


Figure 6.10: Attribution of forecasting error to different sources.

Forecasting errors are of most importance for grid operators when the loads on the grid are extreme, which rarely occurs. Typically, grids are designed robustly with large amounts of excess capacity and availability levels of 99.996% are not uncommon (Alliander N.V., 2022). Many factors impacting the net load are stochastic at best or random at worst. Therefore great care should be taken to relate the impact of conclusions to the size of the sample when analysing a specific subsets of the data. The error analysis under the condition of extreme load, as described in section 6.4.2.2, covers observations from 11 days out of the 401 in total. This work should be considered as the foundation for a more extended analysis, covering a multitude of substations, thereby fortifying the results found in this work.

6.6 Conclusion

Inaccuracy of meteorological forecasts are an important, but overlooked topic in evaluating the predictability of the load on the electricity grid. This work presents a novel framework to attribute the relative contributions of inaccuracies in meteorological forecasts to errors day-ahead forecasts of load on the electricity grid. We show this framework provides results representative of normal operations. Subsequently, the framework is applied to an actual case of day-ahead congestion management on a local scale, over a one-year period. For this case, the largest improvement in accuracy is obtained by using a perfect wind forecast. However, for

moments where the load on the grid is most extreme, the perfect solar forecast delivers the largest improvement. These conclusions are highly location specific and the analysis should therefore be repeated for other areas under active congestion management. The framework presented in this work is published open-source, thereby providing a ready-to-use tool for distribution and transmission system operators to repeat this analysis for other locations. These findings can be used to determine the suitability of day-ahead congestion management for potential locations, as well as indicate the potential improvements in forecasting accuracy by higher quality meteorological forecasts.

Chapter 7

Conclusions and perspectives

7.1 Summary of the most relevant findings

This thesis unites the fields of meteorology and grid operations, with respect to solar PV systems. The central aim of this thesis is to enable optimal integration of solar energy into the electricity grid by advanced understanding of local meteorology. This is key to facilitate the energy transition and move to a renewable based energy system, while also increasing the understanding of cloud-induced irradiance variability. This section summarizes which attributes of irradiance are key in relation to PV induced issues on the grid, to what extent the state-of-the-art weather models can deliver the level of detail required to prevent or mitigate these issues and how inaccuracies of these weather models deteriorate the effectiveness of grid balancing by the grid operators.

7.1.1 The relation between irradiance and PV-induced grid issues

The high-frequency variability of PV generation is expected to be a main source of PV-induced issues on the grid. These fluctuations in PV generation are induced by fluctuations in irradiance, namely passage of clouds, openings in cloud decks and variations in the cloud optical depth. In chapter 3, we investigated the relation between irradiance and solar PV generation, in terms of their variability and commonly observable extremes. Contradicting our hypothesis, we find that peaks in PV generation can even exceed peaks in irradiance. Moreover, peaks in PV generation can exceed typically used values for grid design by over 20%. We show that to accurately represent the conditions where PV integration place the most stress on the grid, a temporal resolution of irradiance in the order of seconds is required. In chapter 4, we related the findings of chapter 3 to over 200.000 detected issues on the electricity grid. These events are combined with ground-based irradiance measurements, satellite observations and power measurements at the substation to analyse and understand the conditions that lead to their occurrence. We show that the main driver of PV-induced issues is the co-occurrence of high PV generation and low energy consumption. This results in overvoltage occurrence on Sundays (not to be confused with sunny days), where energy consumption is low, to be more than double of that on weekdays.

7.1.2 Tailoring weather predictions to PV integration requirements

In chapter 5, we present an algorithm to bridge what is currently available from operational weather models and what is required for PV integration. While clouds in operational weather forecast can effectively only reduce irradiance, we showed in chapter 3 that in reality they result in irradiance enhancement and increased PV generation, only visible at high temporal resolution. We showed that the described algorithm is able to predict 1-minute resolution irradiance at day-ahead lead-times, in terms of its probability density function. This is achieved by post-processing hourly output from KNMI's Harmonie NWP model using machine learning. We show this algorithm can accurately predict when clouds result in irradiance enhancement and its results are generalizable throughout the Netherlands as well as applicable to the global-scale reanalysis model of ECMWF. Furthermore, we provide a method to inspect in high detail which predictive features are key to accurately predict irradiance enhancement and show that half of the forecasting error at 1-minute resolution originates from the forecasting error of the NWP-model used as input.

7.1.3 Application of forecasts to balance the grid in-situ

In chapter 6, we systematically analyse a year-long case study where the grid operator uses day-ahead congestion management to actively balance the load on the grid. Weather forecasts are crucial in forecasting energy generation by wind and solar power system resources, however, these forecasts are not perfect. Quantification of the impact of inaccuracies in the weather forecasts on the net-load forecast is important in grid design and determining operational safety margins during grid balancing. To this end, we developed an open-source machine learning framework, which we apply to this in-situ case study. We show that for the case under investigation, for the whole year, forecasting accuracy is most increased by better forecasts of wind energy. However, when the load on the grid approaches the grid safety limit, improving the solar energy forecast has the greatest effect. The presented framework can be used during the customer integration stage, when investigating the effectiveness of congestion management on any case study.

7.2 Perspectives and recommendations

The progress made during the construction of this thesis has been significant and has opened up new avenues for future research. In this section, four topics are discussed which could greatly benefit the ambition of integrating more solar energy into the grid. These include recommendations on how to improve the grid planning process for solar energy systems, how to leverage smart meters for low-voltage balancing, the added value of using probabilistic forecasts, and a follow-up cross-domain research project.

7.2.1 Grid capacity planning should include fluctuations on the order of seconds

Since irradiance and solar PV generation are highest on the timescale of seconds (chapter 3), and overvoltage event duration strongly agrees with overirradiance duration driven by clouds (chapter 4), grid operators should take these second-scale fluctuations into consideration when performing grid capacity planning calculations. Currently, 15-minute averages are commonly used, whereas this work has shown that this time resolution underestimates the worst-case scenarios by more than 20%. For cases where the grid is constraint due to voltage issues or overcurrent protection, short-lived peaks should be accounted for. Since the number of solar energy systems is expected (and hoped) to greatly increase over the coming years, these short-lived peaks are likely to increase in importance. Luckily, many Sensory Control And Data Acquisition (SCADA) systems offer the possibility to record minimum and maximum values within the selected time averaging period. We highly recommend for grid operators to do three things; A, store these minimum and maximum values to build up a dataset. B, investigate how these extremes depend on solar penetration level. C, account for these short-lived peaks accordingly during grid capacity planning. Future research should be performed to detail the methods required for B and C. The distribution system operators involved in this project has performed step A, for which a screenshot is presented in Figure 7.1, showing a difference of 16% between the maximum of the time-averaged observations versus the maximum of the individual samples.

Additionally, a strong connection between overvoltage duration due to excess PV feed-in and duration of irradiance enhancement is shown in chapter 4, Figure 4.3.

The amplitude of these fluctuations decreases when averaging over time or space. Solar parks have a significantly larger spatial extent compared to household PV systems. Therefore, when calculations are performed by the grid operator for the integration of a new solar park, studies on cloud-size distribution and cloud-shadow transition times as a function of spatial extent (Mol, Stratum, Knap, & Heerwaarden, 2022) can be used to provide estimates of high-frequency fluctuations which should be taken into account.

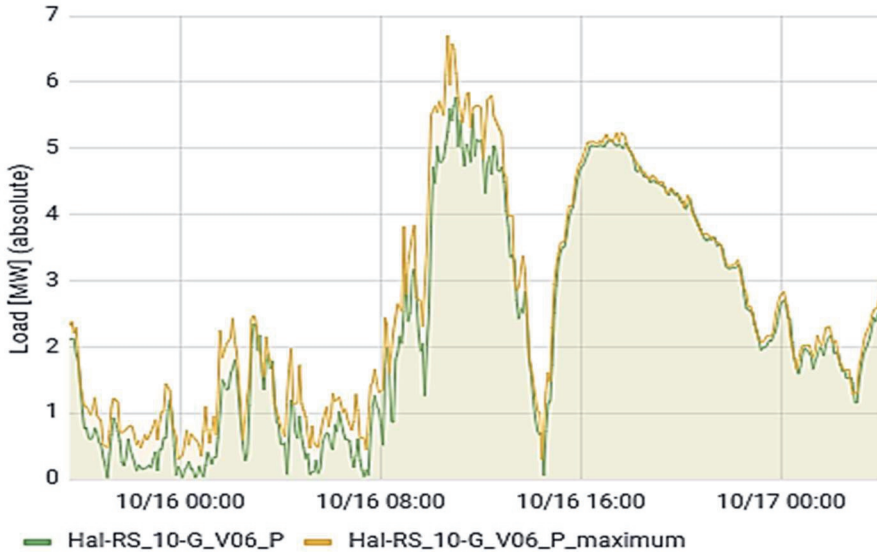


Figure 7.1: Power measurement at the substation Hallum (absolute value), which was the case study under investigation in chapter 6. Typically, for grid capacity planning the 5-minute time-average is used (green), while the maximum of the individual samples (yellow) can be significantly higher. This difference is most profound when there is large renewable feed-in (up to 10/16 15:00). Times are in UTC, which is local time-2hours. Here the maximums of the maximum and average values are 6.70 and 5.77 MW respectively, which is a difference of 16%.

7.2.2 Smart meters enable balancing the low-voltage grid

In this thesis, PV induced grid issues and irradiance variability are studied on the scales of a street or neighbourhood. We show that a strong relation exists between cloud sizes and cloud-shadow transitions, and PV-induced issues on the electricity grid, as detailed in chapter 4. Finally, the application of forecasts to balance the grid is performed at the city scale. A logical extension of this work would be to apply the findings of this thesis to perform grid balancing on the street or neighbourhood level

as well. Lack of sensors, especially in the real-time domain, and privacy restrictions on using smart-meter data inhibited this in the past, as discussed in chapter 4. Two recent developments can cause a major breakthrough for active balancing supply and demand on the low voltage grid. Firstly, the large-scale rollout of the smart meter throughout the Netherlands has completed, potentially providing a new world of data on the quality of the grid (Netbeheer Nederland, 2021), including full time series of voltage on every customer connection of a low-voltage cable for a given overvoltage event. Secondly, as of May 2022, the Dutch Data Protection Authority has accepted a new code of conduct describing when grid operators are allowed to use smart meter data (STAATSCOURANT, 2022). Use cases on capacity planning, congestion management, low-voltage power quality and detection of solar PV generation are among the first to be requested for assessment. We recommend two concrete topics to be placed high on the research roadmap of grid operators. First, the recent availability of large-scale smart meter data should be used to further research the relation of irradiance, PV generation and grid issues. Second, the framework to operate congestion management at the city scale should be tested and where needed adapted to be suitable for the grid on the street and neighbourhood scale, for which smart meter data could prove to be the required data source missing up until now. Additionally, active balancing of the low-voltage grid will benefit from meteorological forecasts at high spatial resolution. Collaboration between the domains of meteorology and grid management, in line with the purpose of this thesis, would help in using advanced metering infrastructure to allow more household-installed solar energy generation.

7.2.3 Adopting probability-based forecasts

The methods proposed in this work to enable optimal integration of solar PV energy, rely on forecasts to actively balance the grid. Forecasts, especially of chaotic systems such as the weather, are both uncertain as well as inaccurate. Examples of inaccuracies of these forecasts are shown in chapters 5 and 6, but readers who occasionally rely on rain forecasts will have plenty of anecdotal evidence. The uncertainty of the weather forecasts depends on the weather conditions. To quantify the uncertainty of a forecast, numerical weather predictions are often performed using slightly different inputs, to generate an *ensemble* of predictions. This allows users of those forecasts to take risk-based decisions, e.g. grid operators during congestion management (chapter 6). If there is a 25% chance of high solar generation, the grid operator could take a different course of action then when that

chance is 1%. Currently, KNMI's Harmonie model, which is the state-of-the-art for the Netherlands, generates ensemble forecasts. However, in the output they publish, the variables relevant for energy forecasting, e.g. windspeed and irradiance, are not included. We encourage operators of ensemble weather forecasting models, such as the KNMI, to include said ensemble members in the operationally available output of their models. Additionally, post-processing methods, like the one proposed in chapter 5, can be used to create confidence estimates of forecasted parameters. While ensemble members address inaccuracies caused by uncertainty of the model input, post-processed confidence estimation can address model inaccuracies as well. Furthermore, all connected parties with a large grid connection in the EU are required to supply their grid operator a forecast of planned energy generation and consumption; the T-prognosis (Netcode elektriciteit, Artikel 13.12, 2022). These forecasts currently do not offer the possibility to provide information on the uncertainty of the forecast. We recommend researchers in the energy sector to investigate how and to what extent sharing uncertainty of planned generation and consumption by end users in their T-prognoses can benefit grid stability.

7.2.4 Expanding forecasting framework over the value chain

The aim of this work is to enable optimal integration of solar energy into the electricity grid by advanced understanding of local meteorology. We recognize however, that achieving large-scale solar PV integration, requires collaboration of the entire value chain; from weather forecasters to accurately predict the weather at spatiotemporal scales that matter for solar energy, to PV park operators to accurately predict their expected generation, and from regional and national grid operators to assess bottlenecks in the distribution and transmission system respectively, to market parties who can provide flexibility by adjusting their planned energy profile when requested to balance the grid. The forecasting frameworks presented in chapters 5 and 6, while important improvements to the state-of-the-art, only consider distinct parts of this value chain. We recommend the findings of this thesis to be used in a larger, cross-domain research project where parties from all links of the value chain collaborate on tackling their challenges together and in a coherent setting. As a start, a proof-of-concept (POC) should be delivered where the distribution and transmission system operators balance an exemplary grid area with significant amounts of renewable generation in a coherent way, leveraging the

flexibility of a single customer based on day-ahead forecasts. This POC should be used to determine what data is required from each party, too what extent existing tooling needs to be expanded and how feedbacks of actions taken based on forecasts need to be incorporated in future forecasts. We expect many of these challenges, e.g. post-processing, forecasting, optimisation, will benefit from using AI. Therefore, together with representative knowledge institutions, market parties and grid operators, we have submitted a joint proposal for a 3-year, 10-million-euro project to the AiNed-programme, originating from the Dutch AI Coalition (AiNed, 2022).

Overall, the progress made during the construction of this thesis has laid the groundwork for exciting new avenues of research on the intersection between the fields of solar energy meteorology and grid integration. By continuing to explore these topics and others, we can help to accelerate the transition to a more sustainable and equitable energy system.

This work in the media



solar magazine.nl/nieuws-zonne-energie/i21852/stroomproductie-zonnepanelen-pekt-juist-op-bewolkte-dagen

SOLAR MAGAZINE
NO. 1 IN NIEUWS & ACHTERGRONDEN

Home Nieuws Industrie

Stroomproductie zonnepanelen peikt juist op bewolkte dagen

De stroomproductie van zonnepanelen kan bij bewolking 20 procent groter zijn dan bij een strakblauwe lucht. Dat blijkt uit een eerste deelstudie van Wageningen University & Research (WUR) en netbeheerder Liander.



Weeronline Weernieuws Populaire plaatsen Mijn Plaatsen 0

Home > Nieuwsoverzicht > Liander: ook bewolkte dagen zorgen voor stroompieken zonnepanelen



Liander: ook bewolkte dagen zorgen voor stroompieken zonnepanelen

Aangemaakt: 26 jun 2020 14:15 uur



TECHNIEK MAAKT JE WERELD

DE INGENIEUR

Niet alleen zeer zonnige bewolkte dagen leiden studie naar de invloed

juist op dagen met bewolking worden de hoogste pieken in de productie van zonne-energie gemeten. Dat is de verrassende uitkomst van onderzoek door onder meer netbeheerder Liander en de Wageningen Universiteit.

Zonneschijn verloopt zelden regelmatig. De intensiteit kan per minuut en per plek verschillen. Verschijnen er wolken, dan is het helemaal gedaan met de zonneschijn. Liander, de Wageningen Universiteit, het KNMI en de Universiteit Utrecht

zonnestraling



Energieia Redactie - Energieia

Archief Trilemma Columns Meer

Zonnepanelen leveren grootste vermogenspieken op bewolkte dagen

Zonnepanelen leveren op afwisselend bewolkte dagen grotere vermogenspieken op dan op zeer zonnige dagen. Dat blijkt uit een onderzoek van netbeheerder Liander, in samenwerking met Wageningen Universiteit, het KNMI en de Universiteit Utrecht.

Voor de duidelijkheid: de meeste energie wordt opgewekt op zonnige dagen. Maar de pieken in de stroomproductiecapaciteit zijn hoger op dagen met stapelwolken, dus dagen met afwisselend bewolking en zon.

Volgens Liander-onderzoeker Frank Kreuwel, die ook in

Hoe kan bewolking pieken in de opwekking van zonne-energie veroorzaken? Dat heeft twee redenen. Ten eerste reflecteren witte wolken extra licht op zonnepanelen als het gedeeltelijk bewolkt is. Daarnaast speelt de temperatuur een rol. Zonnepanelen werken minder efficiënt als ze warm worden. Wanneer de panelen liggen op een schaduw, waardoor ze de kans krijgen te koelen. Als de zon dan weer achter de wolk vandaan komt, dan valt er extra licht op een afgekoeld zonnepaneel. Dat zorgt voor een flinke piek in de opwekking van energie.

newscientist.nl/nieuws



IDEËN DIE DE WERELD VERANDEREN



Nieuwsoverzicht

02-07
Commissie kraakt rol
Amsterdam bij crisis
AEB

Appendix : dissemination of project results at the grid operator

The aim of this PhD project is to enable optimal integration of solar energy into the local electricity grid. In addition to advancing the body of scientific knowledge, this also requires acceptance of and willingness to apply the results produced in this work by relevant parties, in particular grid operators. To aid the ambition of this project, blogs have been posted to the intranet of Alliander detailing findings described in or related to this work. A selection of these is included here, in Dutch, as they were posted originally.

8.1 Ook bewolkte dagen zorgen voor stroomopwekpieken

Niet alleen zeer zonnige dagen, maar juist ook bewolkte dagen, zorgen voor veel pieken in de opwek van zonne-energie. Dat laat een deelstudie naar de impact van zonne-energie op het elektriciteitsnet zien, die we met onder meer het KNMI uitvoeren.

Hoe moeten we in de toekomst omgaan met de inpassing van grootschalige opwek uit zonne-energie? Dat is wat Liander momenteel onderzoekt. Het aantal zonneweides en zonnepanelen op daken neemt de komende jaren immers flink toe. Er wordt zelfs rekening gehouden met een groei naar 6 gigawatt, zes keer zoveel als nu. De 6 gigawatt is vergelijkbaar met het elektriciteitsverbruik van ongeveer 4 miljoen huishoudens.

8.1.1 Veranderende patronen

Bij zonne-energie is sprake van veranderende patronen: de zon schijnt niet op ieder moment van de dag en de intensiteit verschilt sterk van plek tot plek. Samen met het KNMI en de universiteiten van Wageningen en Utrecht wordt geanalyseerd welke effecten verschillende weertypes hebben op de veranderingen. Inzicht in stroompieken is voor Liander belangrijk om het elektriciteitsnet veilig te besturen.

8.1.2 Ook stroompieken bij bewolking

Uitkomst van het eerste deelonderzoek: niet alleen zeer zonnige dagen zorgen voor een piek aan opwek. Sterker nog; gedeeltelijke bewolking kan de pieken versterken. “Zonnepanelen wekken meer energie op als er meer licht op valt én als ze koeler zijn,” zegt onderzoeker en collega Frank Kreuwel. “Wolken zijn wit, omdat ze veel licht reflecteren. Op dagen met veel stapelwolken, zorgen de wolken ervoor dat er op sommige momenten extra licht op de panelen valt.”

8.1.3 Meer opwek bij afkoeling

“Verder zorgen de wolken ervoor dat de zonnepanelen af en toe in de schaduw liggen,” gaat Frank verder. “Op een heldere dag kan een paneel wel 60°C worden. Kunnen ze even afkoelen? Dan kunnen de panelen, als ze weer in de zon komen, een hogere efficiëntie behalen waardoor ze meer energie kunnen opwekken. En dan valt er nog eens extra licht op de panelen door reflecties van de wolk die net voorbijdrijft. We hebben

onderzocht dat de stroomopwekpiek voor een zonnepaneelsysteem voor een gemiddeld huis wel 22% hoger kan zijn.”

8.1.4 Inzichten van belang voor efficiënt netbeheer

De inzichten uit het onderzoek zijn van belang om een zo goed mogelijk inzicht te krijgen in de effecten van zon op het net. De meeste energie wordt opgewekt op heldere dagen. De hoogste stroompieken zijn juist op dagen mét bewolking. Steeds meer huishoudens en (boeren)bedrijven hebben zonnepanelen en vooral op het laagspanningsnet (de kabels die naar huizen lopen) ontstaan steeds meer spanningsproblemen. Met de uitkomsten van het onderzoek kunnen we als netbeheerder de elektriciteitsnetten beter benutten en dragen we bij aan de betrouwbaarheid van de toekomstige energievoorziening.

Meer weten? Lees de wetenschappelijke publicatie.

8.2 Voorspel een gat in de lucht

Congestie management wordt steeds vaker toegepast om bij (tijdelijke) bottlenecks in het net toch alle klanten van spanning te voorzien. Bij congestie management wordt elke dag een inschatting gemaakt van wat er gaat gebeuren op het net. Deze voorspellingen zijn essentieel, maar ook erg lastig. Eén van de gebieden waar congestie management wordt toegepast is station Hallum. In deze blog een kort inkijkje hoe we een satelliet op 36.000 km hoogte gebruiken om twee dagen van tevoren te voorspellen of er wel of niet gedurende 4 seconde een stroom 660 Ampère gaat lopen.

8.2.1 Regelstation Hallum

Achter regelstation Hallum (Friesland) kan door klanten meer capaciteit gevraagd worden dan het net aankan. Specifiek gaat het hier om een overschot aan duurzame opwek; Opname Door Net (ODN). Achter RS Hallum zit een combinatie van (huishoudelijk) energieverbruik, teruglevering door wind en teruglevering door zon. Op dagen dat het hard waait, én de zon flink schijnt, én er weinig energieverbruik is, kan

het net in de problemen komen. Daarom is hier sinds vorig jaar een afspraak met het windpark, om op verzoek minder te produceren. Zo kan de energievoorziening in de regio worden gegarandeerd.

8.2.2 Buiten de band

Omdat de kans op overbelasting in het weekend het grootst is, bepalen collega's van System Operations vóóraf of de komende dagen momenten zijn waarop het windpark verzocht moet worden minder energie terug te leveren. Dit gebeurt in de regel op vrijdagochtend. Nauwkeurige voorspellingen van energieverbruik en duurzame opwek zijn dus erg belangrijk om tot een goede prognose te komen. Team Korte Termijn Prognoses ontwikkelt een applicatie die op basis van o.a. weerdata, marktprijzen, en feestdagen voorspelt wat de belasting op het station gaat zijn. Meestal gaat dit goed, maar soms zit er een flinke afwijking tussen de prognose en de daadwerkelijke belasting. Zie onderstaande afbeelding van 23 mei.

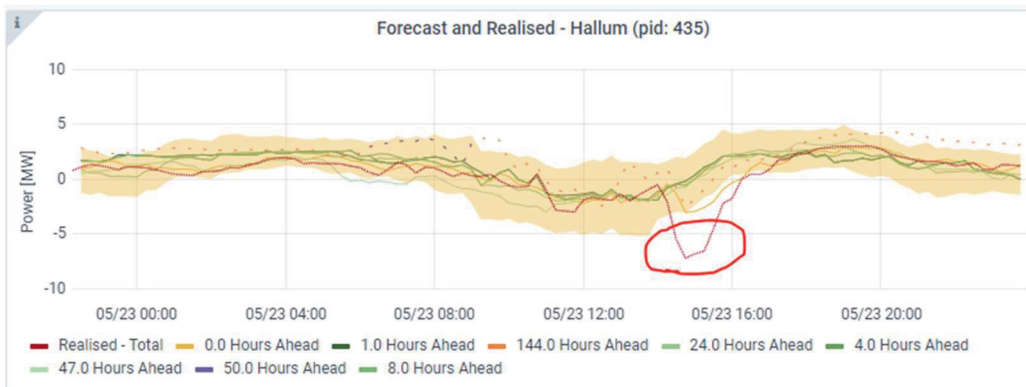


Figure 8.1: Realisatie (rood) en prognose (groen) van de belasting op RS Hallum op 23 mei. Geel geeft een 98% betrouwbaarheidsband aan. + = energieverbruik (LDN), - = teruglevering (ODN). Rond 14:30 (UTC-tijd) was de realisatie een stuk negatiever dan voorspeld.

8.2.3 Weermodellen

Midden op de dag zien we een flinke terugleverpiek die het prognosemodel had gemist. Grote kans dat dit komt door zonne-energie. Voor het maken van de belastingsprognoses zijn weermodellen een belangrijke input. Wij maken gebruik van m.n. het Harmonie weermodel van het KNMI. Dit is het *state-of-the-art* weermodel als het gaat om prognoses boven Nederland. Op haar beurt rust dit model op een grootschalig, Europees weermodel. Hiervoor worden metingen van meetstations (van het KNMI en van particulieren), satellietopnames (op 36.000 km hoogte), radarbeelden en sensoren in

vliegtuigen gebruikt om tot twee weken vooruit een prognose van het weer te maken.

Ontzettend knap. Maar ook soms ontzettend lastig. Als de weersituatie instabiel is, kan een kleine verandering nu grote impact hebben op het weer van over twee dagen. En dan is op de schaal van weermodellen Nederland eigenlijk maar klein. En het gebied rond Hallum al helemaal.

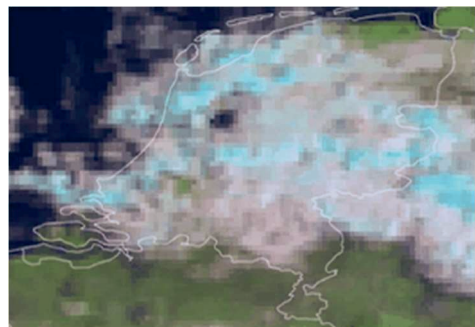


Figure 8.2: Satellietopname (EUMETSAT) van het wolkenbeeld in tijdstappen van 15 minuten.

In bovenstaande animatie is de satellietopname van 23 mei te zien, in stapjes van een kwartier, met een versnelling van een uur per seconde.

Je ziet dat precies om 14:30 een opening in het wolkendek ontstaat boven Noord-Friesland; precies het gebied rond Hallum. En je ziet ook dat deze opening net zo snel weer verdwenen is als hij verscheen. Dit soort weercondities zijn ontzettend lastig te voorspellen. Niet alleen voor ons, maar ook voor de 350 man uit 30 landen die bij het Europese weerbureau werken aan de weermodellen die als basis voor de rest dienen.

8.2.4 Zekere onzekerheid

Sturen op basis van prognoses vereist een hele goede risico-afweging. Als je maar lang genoeg stuurt op basis van prognoses, weet je zeker dat zich een

keer de situatie voordoet dat de prognoses niet kloppen. Door goed ons huiswerk te doen, kunnen we dat aantal keer tot een minimum beperken, maar het gaat een keer gebeuren.

Dat is ook een voordeel; omdat je weet dat het gaat gebeuren, kan je je er op voorbereiden. Bijvoorbeeld door beveiligingen aan te passen, alerting te configureren of klantafspraken te maken om direct in te grijpen. Al deze opties worden dan ook toegepast in congestiegebieden. En van de keren dat de prognose afwijkt, is het meestal op momenten dat het niet erg is. Bijvoorbeeld op 23 mei, hier bleef ook de hoge terugleverpiek ruim binnen de netcapaciteit.

8.3 Meteodata en productie-/verbruiksprognoses

Na een riante zomer is het inmiddels weer koud en vroeg donker. Dat zien we aan de sjaals, mutsen en autoruitkrabbende buurtbewoners. En aan de belasting op ons net. Kou en donker betekent een toename in het energieverbruik. Netmanagement gebruikt slimme computermodellen voor een aantal kritische netgebieden te voorspellen wat de netbelasting de komende dagen gaat worden. Sinds deze week worden daar ook ruim 50 weersimulaties van het KNMI voor gebruikt. Een hele prestatie!

In het gebied Nijmegen-Noord is afgelopen jaar géén extra kabel aangelegd. Wel worden er veel huizen bijgebouwd en neemt de belasting toe. Om congestie op het net te voorkomen, is op deze locatie een *flexmarkt* actief ([lees meer](#)). Hierbij wordt aan marktpartijen gevraagd om even wat minder energie te verbruiken, als de ruimte op het net beperkt is. Hiervoor moeten we als netbeheerder vooraf aan kunnen geven óf en hóveel congestie we op het net verwachten. Op deze manier dragen korte-termijn prognoses bij aan de netveiligheid.

8.3.1 Interessante mix

De illustratie hiernaast geeft een beeld van Nijmegen-Noord, het

gebied wat wordt gevoed door regelstation de Waalsprong. Naast de ongeveer 8000 huishoudens, waarvan een relatief groot deel zonnepanelen heeft, staan er 4 windturbines van 2,5MWp per stuk. Voorlopig kan er in dit gebied alleen congestie optreden als het energieverbruik hoog is, terwijl er géén windenergie wordt geproduceerd. In de praktijk is dit alleen 's winters tussen 17 en 21 uur. Erg belangrijk dus om voor deze interessante mix van energiestromen de belasting nauwkeurig te kunnen voorspellen, en ook om vooraf al te kunnen inschatten hoe betrouwbaar je voorspelling is.

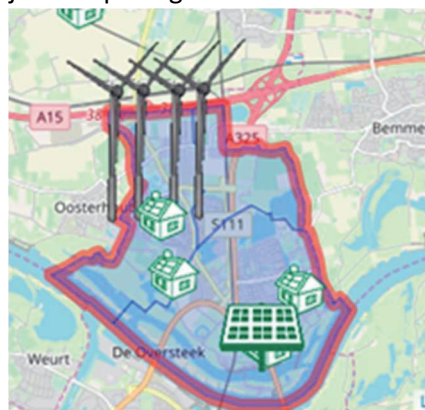


Figure 8.3: Overzicht Nijmegen-Noord NB: De impact van zonne-energie op het net wordt óók steeds groter. En net als wind is dit ook erg lastig te voorspellen. In deze blog laten we zon buiten beschouwing, daarover volgende keer meer.

8.3.2 Wel wind, geen opwek

Twee factoren maken het voorspellen van de windenergie lastig. De basis is simpel; hoe harder het waait, hoe meer windenergie er wordt opgewekt. Alleen, soms waait het best hard, maar worden de turbines toch stilgezet. Bijvoorbeeld als het té hard waait, of als er kans is op ijsvorming aan de bladen van de turbines.

8.3.3 Niet exact voorspelbaar

Bij de beslissing of en hoeveel flex we willen inkopen om mogelijke congestie te voorkomen, willen we ook met de onzekerheid van de windverwachting rekening houden. Op basis van de 52 simulaties van het KNMI berekenen we wat de kans is dat er geen windopwek zal zijn. Als die groter is dan een bepaalde grens, gaan we ervan uit dat er geen windenergie wordt opgewekt bij het bepalen van de mogelijke congestie. Ook het energieverbruik van de huishoudens is niet exact voorspelbaar. De modellen die we gebruiken geven niet alleen een verwacht verbruik, maar ook een instelbaar betrouwbaarheidsinterval. Zie de afbeelding hieronder. De rode stippellijn geeft het moment aan waarop het screenshot is gemaakt.

Daarnaast kan de windsnelheid sterk afwijken van wat er vooraf werd verwacht. Naarmate je langer in de toekomst kijkt, hoe groter deze onzekerheid wordt. Het KNMI rekent 52 weersimulaties door om een zo goed mogelijk beeld te krijgen van de te verwachten windsnelheid, en dat herhalen ze 4 keer per dag. Het plaatje hieronder geeft een weergave van de individuele weersimulaties voor wat betreft windsnelheid.

8.3.4 Bredere toepassing

De korte-termijn prognoses van netbelasting worden gebruikt binnen de flexmarkt. Maar dezelfde methodes helpen ons ook bij andere uitdagingen. Bijvoorbeeld het *flexnet*, waarbij belasting via iMSR'en naar omliggende onderstations kan worden verschakeld. Ook moeten we als netbeheerder nauwkeurige *Delfor T-prognoses* afgeven aan TenneT, zodat zij voor de stabiliteit op het landelijke net kunnen zorgen. En helpen de prognoses bij het matchen van lokale vraag en aanbod, zoals *smart charging* van elektrische auto's wanneer de zon (niet) schijnt.

8.3.5 Weerdata

Weerdata wordt steeds belangrijker binnen Alliander en het wordt op steeds meer plekken gebruikt. Maak jij hier ook gebruik, of zou je dat graag

willen? Neem gerust contact met ons op! We hebben hier inmiddels aardig wat ervaring in opgebouwd, en een

samenwerking lopen met de meteorologie groep van de Wageningen universiteit.

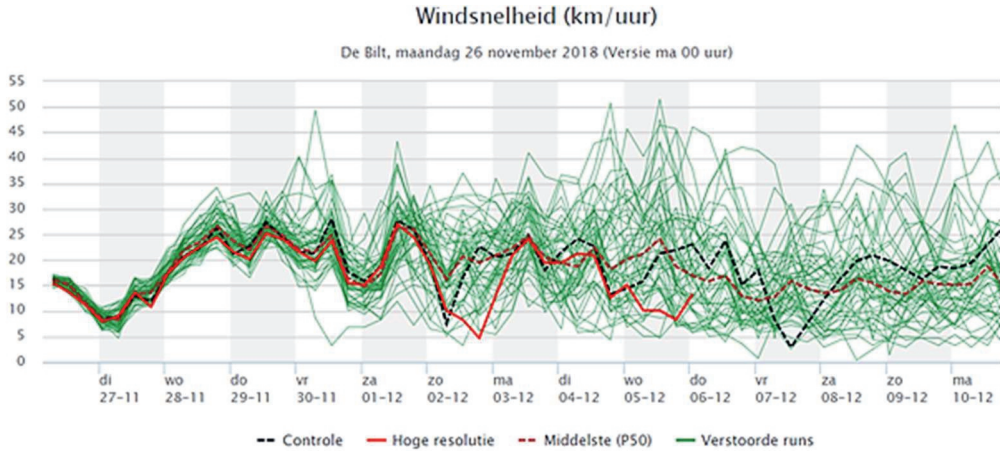


Figure 8.4: Weersimulaties KNMI

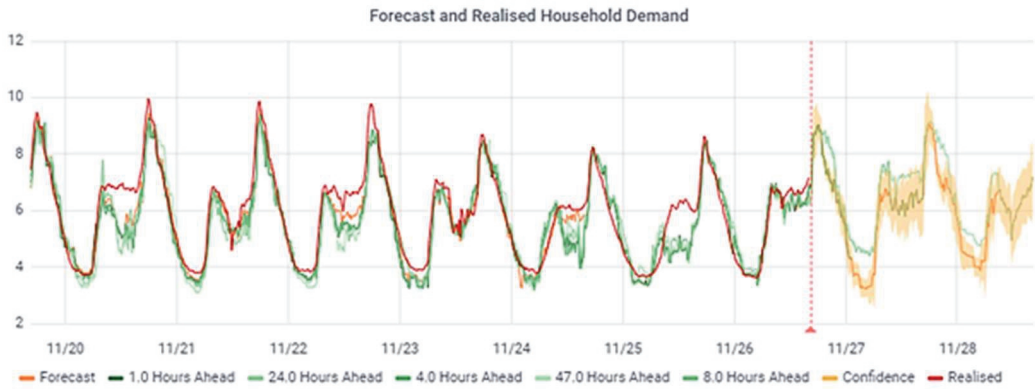


Figure 8.5: Gerealiseerde (rood) en voorspelde belasting (groen) van het huishoudelijke energieverbruik. De verticale rode stippellijn geeft het moment van het screenshot aan, met rechts daarvan in geel het betrouwbaarheidsinterval.

8.4 Alliander Checkt: “Zonnepanelen werken niet/wel op de warme zomerdagen”

In navolging van populaire nieuwsrubrieken wordt in Alliander Checkt een recente bewering over energie gecontroleerd. Deze keer is het onderwerp het al dan niet presteren van zonnepanelen bij zomerse temperaturen.

8.4.1 De aanleiding

Wellicht is het je opgevallen; dit jaar kent een uitzonderlijk warme zomer. Nieuwsberichten over hittegolven en neerslagtekorten volgen elkaar in rap tempo op. Maar, niet alleen de planten hebben moeite met zulke omstandigheden, ook zonnepanelen zouden baat hebben bij een wat gematigdere zomer. Sterker nog, in een recente LinkedIn post wordt gesteld: “Zonnepanelen werken niet op de warme zomerdagen” (<https://www.linkedin.com/feed/update/urn:li:activity:6428546968250777600/>)

We checken deze bewering.

8.4.2 Waar is het op gebaseerd?

Alexander Suma, schrijver van de post en producent van de PowerNEST (een systeem om zonnepanelen te koelen), schrijft in een reactie onder zijn post: “Het klopt inderdaad dat “niet” een te

grote uitspraak is. Het maakt veel los; begrijpelijk. Toch is het jammer dat de panelen tot 15% minder produceren op een warme zomerdag wanneer er het meeste zonnestraling is en er het meeste airco koeling wordt gebruikt. Ik zie PowerNEST dan als een goede oplossing hiervoor”

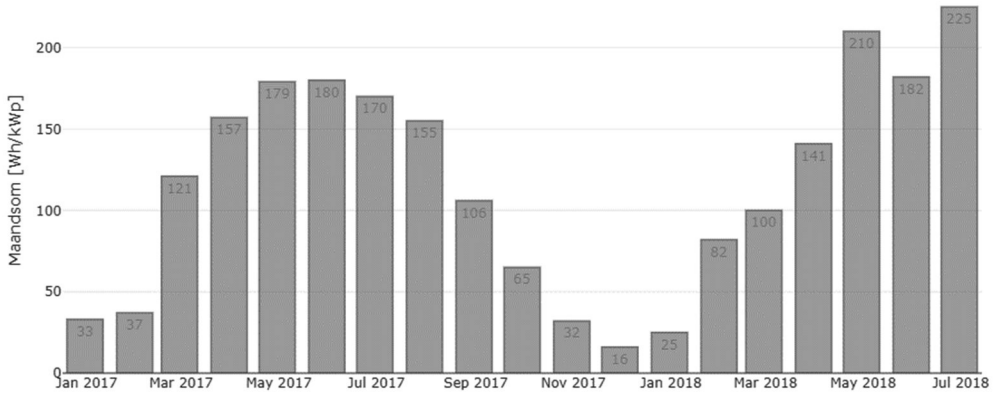
Maar hoe komt het dat nou? Professor Wim Sinke van TNO legt uit: hoe warmer een zonnepaneel is, hoe minder goed het werkt. En op dagen als deze wordt zo'n paneel bloedheet: rond de 65 graden, 30 graden hoger dan de omgevingstemperatuur. Dat komt doordat er weinig wind is en de zon fel schijnt. Die hitte helpt niet mee: zonnepanelen leveren in dit weer per zon-uur 15 procent minder op dan wanneer de zon even fel zou schijnen in de winter, met een buitentemperatuur van rond het vriespunt. (Bron: NOS-artikel waar Suma naar refereerde: <https://nos.nl/artikel/2243431-zonnepanelen-zijn-blij-met-de-zon-niet-met-de-hitte.html>)

8.4.3 En, klopt het?

Afgelopen week kwam een vraag binnen van een media partij bij het Liander DataLoket. Gevraagd werd naar de hoeveelheid zonne-opwek op

onze netten in de gemeente Alphen aan de Rijn, van 2017 en 2018 voor zover bekend. Vanuit het project iCarus wordt data ontvangen van de opwek van zonnepaneelsystemen van participerende huishoudens,

ongeveer 2500 in Nederland, en ongeveer 60 in de gemeente Alphen aan de Rijn. We gebruiken de gegevens van deze 60 systemen van de afgelopen anderhalf jaar om de bewering te checken.



In de figuur hierboven staat de totale hoeveelheid energie die de systemen gemiddeld hebben opgewekt, uitgedrukt in Wh per kWp geïnstalleerd vermogen (ter referentie; gemiddeld was het geïnstalleerd vermogen 2.3 kWp). We zien voor afgelopen juli een uitzonderlijk hoge opbrengst ten opzichte van een jaar eerder; 225 Wh ten opzichte van 170 Wh een jaar eerder. Terwijl de opwek in juni 2018 vergelijkbaar is met de opwek in juni 2017.

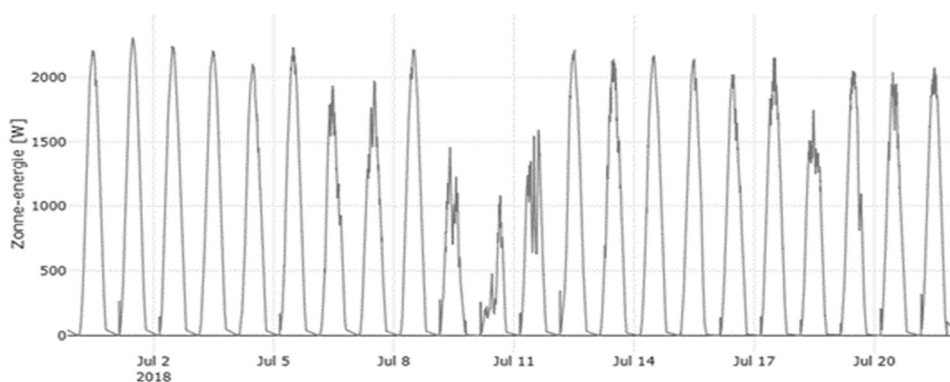
Ook als we kijken naar het gemiddelde opwekprofiel per dag (bovenstaande afbeelding), zien we dat de piek voor een dag in juli inderdaad lager ligt dan een dag in juni. Echter, we zien ook dat er op een bewolkte dag, bijvoorbeeld 10 juli, veel minder energie wordt opgewekt dan op een onbewolkte dag. De hogere temperaturen leiden tot een

vermindert rendement van de zonnepanelen, maar in warme maanden zijn er meer uren zonneshijn die dit ruimschoots compenseren.

8.4.4 Conclusie

We checken de uitspraak bij een LinkedIn bericht dat “Zonnepanelen ... niet [werken] op de warme zomerdagen”. Afgelopen juli wekten zonnepaneelsystemen in de gemeente Alphen aan de Rijn gemiddeld 32% meer op dan een jaar eerder en 24% meer dan juni van dit jaar. Weliswaar vermindert het rendement van zonnepanelen bij in warme zomermaanden, maar dit wordt ruimschoots gecompenseerd door meer uren zonneshijn waardoor er in totaal meer zonne-energie wordt opgewekt. We beoordelen de stelling als **onwaar**.

Gemiddeld opwekprofiel per dag



References

- Abur, A., & Expósito, A. (2004). *Power system state estimation: theory and implementation*. Boca Raton: CRC Press.
- Ahmed, R., Sreeram, V., & Mishra, M. (2020). A review and evaluation of the state-of-the-art in pv solar power forecasting: techniques and optimization. *Renew. Sustain. Energy Rev.*, 109792.
- AiNed. (2022, 11 18). *Informatiebrochure_AiNed_Ketenproject*. Retrieved from Ontwikkeling AiNed Ketenproject gestart: https://ained.nl/wp-content/uploads/2022/08/Informatiebrochure_AiNed_Ketenproject_juni-2022.pdf
- Al Mamun, A., Sohel, M., Mohammad, N., Sunny, M., Dipta, D., & Hossain, E. (2020). A Comprehensive Review of the Load Forecasting Techniques Using Single and Hybrid Predictive Models. *IEEE Access*, pp. 134911-134939.
- Alboaouh, K., & Mohagheghi, S. (2020). Impact of Rooftop Photovoltaics on the Distribution System. *journal of renewable energy*.
- Alliander N.V. (2022, 9 16). *Jaarverslag 2021*. Retrieved from Alliander.com: https://www.alliander.com/content/uploads/dotcom/Alliander_Jaarverslag_2021.pdf
- Alliander, N.V. (2020, April). *Factsheet kerngegevens Alliander*. Retrieved July 31, 2020, from Alliander N.V.: <https://www.alliander.com/content/uploads/dotcom/ALL200040-Factsheet-Alliander-2020.pdf>
- Ari, A., Arregui, N., Black, S., Celasun, O., I. D., Mineshima, A., . . . Zhunussova, K. (2022). *Surging Energy Prices in Europe in the Aftermath of the War: How to Support the Vulnerable and Speed up the Transition Away from Fossil Fuels*. International Monetary Fund.
- Arrillaga, J., Vilà-Guerau de Arellano, J., Bosveld, F., Klein Baltink, H., Yagüe, C., Sastre, M., & Román-Cascón, C. (2018). Impacts of afternoon and evening sea-breeze fronts on local turbulence, and on CO₂ and radon-222 transport. *Q J R Meteorol Soc.*, 990–1011.
- Bakker, K., Whan, K., Knap, W., & Schmeits, M. (2019). Comparison of statistical post-processing methods for probabilistic NWP forecasts of solar radiation. *Solar Energy*, 138-150.
- Barnes, W., Xiong, X., & Salomonson, V. (2003, december). Status of terra MODIS and aqua modis. *Advances in Space Research*, pp. 2099-2106.

References

- Bengtsson, L., Andrae, U., Aspelien, T., Batrak, Y., Calvo, J., De Rooy, W., & Gleeson, E. (2017). The Harmonie-Arome model configuration in the Aladin-Hirlam NWP system. *Mon. Weather Rev.*, 1919-1935.
- Bergmeir, C., & Benítez, J. (2012). On the use of cross-validation for time series predictor evaluation. *Information Sciences*, 192-213.
- Blum, M., & Riedmiller, M. (2013). Electricity demand forecasting using Gaussian processes. *15th AAAI Conference on Trading Agent Desing and Analysis* (pp. 10-13). AAAIWS'13-15.
- Bollen, M., & Hassan, F. (2011). *Integration of Distributed Generation in the Power System*. Wiley.
- Brooks, H., Doswell, C., & Maddox, R. (1992, march 01). On the use of mesoscale and cloud-scale models in operational forecasting. *Weather and Forecasting*, pp. 120-132.
- Brown, T. A. (1974). *Admissible scoring systems for continuous distributions*. Santa Monica: The Rand Corporation.
- Centraal Bureau voor de Statistiek. (2018, 12 06). *bevolking-en-huishoudens-4-cijferige-postcode-1-1-2018*. Retrieved 08 06, 2020, from Centraal Bureau voor de Statistiek: https://www.cbs.nl/-/media/_excel/2018/49/bevolkingperpostcode_1januari2018.xls
- Chen, T., & Guestrin, C. (2016). XGBoost: A Scalable Tree Boosting System. *In Proceedings of the 22nd ACM SIGKDD International Conference on Knowledge Discovery and Data Mining* (pp. 785–794). New York, NY, USA: ACM.
- Chu, Y., Li, M., Coimbra, C., Feng, D., & Wang, H. (2021). Intra-hour irradiance forecasting techniques for solar power integration: A review. *iScience*, 24(10).
- Cobben, S., Gaiddon, B., & Laukamp, H. (2008). Impact of Photovoltaic Generation on Power Quality in Urban areas with High PV Population: Results from Monitoring Campaigns. *Intelligent Energy Europe*. Brussels.
- Cohen, M., & Callaway, D. (2016). Effects of distributed PV generation on California's distribution system, Part 1: Engineering simulations. *Solar Energy*, 126-138.
- David, J., Elphick, S., & Crawford, M. (2017). Cause and effect of overvoltage on the LV network. *Australasian Universities Power Engineering Conference* (pp. 1-6). University of Wollongong.
- De Brabandere, K., Woyte, A., Belmans, R., & Nijs, J. (2004). Prevention of inverter voltage tripping in high density PV grids. *19th EU-PVSEC*. Paris.
- de Rooy, W., Siebesma, P., Baas, P., Lenderink, G., de Roode, S., de Vries, H., . . . van't Veen, B. (2021). Model development in practice: A comprehensive update to the boundary layer schemes in HARMONIE-AROME cycle 40. *Geoscientific Model Development Discussions*, 1-48.

- Delle Monache, L., Nipen, T., Liu, Y., Roux, G., & Stull, R. (2011). Kalman filter and analog schemes to postprocess numerical weather predictions. *Monthly Weather Rev.*, 3554-3570.
- Diagne, M., David, M., Lauret, P., Boland, J., & Schmutz, N. (2013). Review of solar irradiance forecasting methods and a proposition for small-scale insular grids. *Renewable & Sustainable Energy Reviews*.
- Draper, N., & Smith, H. (1981). *Applied Regression Analysis*. Wiley .
- Driemel, A., Augustine, J., Behrens, K., Colle, S., Cox, C., Cuevas-Agulló, E., . . . Mimouni, M. (2018). Baseline Surface Radiation Network (BSRN): structure and data description (1992-2017). *Earth Syst. Sci. Data*, 10, 1491-1501.
- ECMWF. (2015). IFS Documentation CY41R1 - Part III: Dynamics and Numerical Procedures. In ECMWF, *IFS Documentation CY41R1* (p. 29).
- Elsinga, B., & van Sark, W. (2017). Short-term peer-to-peer solar forecasting in a network of photovoltaic systems. *Applied Energy*(206), 1464-1483.
- ENTSO-E. (2022, 9 14). *ENTSO-E Transparency Platform*. Retrieved from ENTSO-E Transparency Platform day ahead prices: <https://transparency.entsoe.eu/transmission-domain/r2/dayAheadPrices>
- Etling, D., & Brown, R. A. (1993). Roll vortices in the planetary boundary layer: A review. *Boundary-Layer Meteorology*, 215–248.
- European Union. (2016). *General Data Protection Regulation 2016/679*. Retrieved from <http://eur-lex.europa.eu/eli/reg/2016/679/oj>
- Fachrizal, R., Ramadhani, U., Munkhammar, J., & Widén, J. (2021). Combined PV–EV hosting capacity assessment for a residential LV distribution grid with smart EV charging and PV curtailment. *Sustainable Energy, Grids and Networks*, 100445.
- Faraji, J., Ketabi, A., Hashemi-Dezaki, H., Shafie-Khah, M., & J.P.S., C. (2020). Optimal Day-Ahead Self-Scheduling and Operation of Prosumer Microgrids Using Hybrid Machine Learning-Based Weather and Load Forecasting. *IEEE Access*.
- Freris, L., & Infeld, D. (2020). *Renewable Energy in Power Systems*. John Wiley & Sons.
- Fretzen, U., Ansarin, M., & Brandt, T. (2021). Temporal city-scale matching of solar photovoltaic generation and electric vehicle charging. *Applied Energy*, 116160.
- Geisser, S. (1975). The Predictive Sample Reuse Method with Applications. *Journal of the American Statistical Association*, 320-328.
- Glahn, H., & Lowry, D. (1972). The use of model output statistics (MOS) in objective weather forecasting. *J. Appl. Meteorol*, 1203-1211.
- Goyle, G. (2012). *Renewable Electricity and the Grid: The Challenge of Variability*. Routledge.

References

- Gristey, J., Feingold, G., Glenn, I., Schmidt, K., & Chen, H. (2020). On the Relationship Between Shallow Cumulus Cloud Field Properties and Surface Solar Irradiance. *Geophysical Research Letters*.
- Gueymard, C. (2017). Cloud and albedo enhancement impacts on solar irradiance using high-frequency measurements from thermopile and photodiode radiometers. Part 1: Impacts on global horizontal irradiance. *Solar Energy*, 153, 755-765.
- Haaren, R. v., Morjaria, M., & Fthenakis, V. (2014). Empirical assessment of short-term variability from utility-scale solar PV plants. *progress in photovoltaics: research and application*, 22(5), 548-559.
- Hadush, S., & Meeus, L. (2018). DSO-TSO cooperation issues and solutions for distribution grid congestion management. *Energy Policy*, pp. 610-621.
- Haque, M., & Wolfs, P. (2016). A review of high PV penetrations in LV distribution networks: Present status, impacts and mitigation measures. *Renewable and Sustainable Energy Reviews*, 1195-1208.
- Heinze, R., Dipankar, A., Henken, C., Moseley, C., Sourdeval, O., Trömel, S., & al., e. (2016, October 22). Large-eddy simulations over Germany using ICON: a comprehensive evaluation. *Quarterly Journal of the Royal Meteorological Society*.
- Hersbach, H. (2000). Decomposition of the Continuous Ranked Probability Score for Ensemble Prediction Systems. *Weather and Forecasting*, 559-570.
- Hersbach, H. (2020). The ERA5 global reanalysis. *QJRMS*.
- Hersbach, H., Bell, B., Berrisford, P., Biavati, G., Horányi, A., Sabater, J., . . . Thépaut, J.-N. (2018). *ERA5 hourly data on single levels from 1979 to present*. Copernicus Climate Change Service (C3S) Climate Data Store (CDS). Retrieved 6 24, 2021, from <https://cds.climate.copernicus.eu/cdsapp#!/dataset/reanalysis-era5-single-levels?tab=overview>
- Hinkelman, L. (2013). Differences between along-wind and cross-wind solar irradiance variability on small spatial scales. *Solar Energy*(88), 192-203.
- Hunta, J., Nascimento, A., Nascimento, N., Vieira, L., & Romero, O. (2022, 5). Possible pathways for oil and gas companies in a sustainable future: From the perspective of a hydrogen economy. *Renewable and Sustainable Energy Reviews*, p. 112291.
- International Energy Agency. (2022, 10 20). *Renewables*. Retrieved from IEA: <https://www.iea.org/reports/renewables>
- IRENA. (2021). *Renewable Energy Statistics 2021*. Abu Dhabi: The International Renewable Energy Agency.
- IRENA. (2022). *Smart Electrification with Renewables: Driving the Transformation of Energy Services*. Abu Dhabi: International Renewable Energy Agency.

- Javadi, M., Gough, M., Lotfi, M., Nezhad, A.E., Santos, S., & Catalão, J. (2020). Optimal self-scheduling of home energy management system in the presence of photovoltaic power generation and batteries. *Energy*, 118568.
- Jenkins, N., Allan, R., Crossley, P. K., & Strbac, G. (2000). Embedded Generation. *The Institution of Electrical Engineers, IEE Power and Energy Series*.
- Karagiannopoulos, S., Roald, L., Aristidou, P., & Hug, G. (2017, august 27). Operational planning of active distribution grids under uncertainty. *Bulk Power Systems Dynamics and Control Symposium*.
- Ke, G., Meng, Q., Finley, T., Wang, T., Chen, W., Ma, W., . . . Liu, T. (2017). LightGBM: A Highly Efficient Gradient Boosting Decision Tree. *Advances in Neural Information Processing Systems*.
- Khorasanizadeh, H., Mohammadi, K., & Jalilvand, M. (2014, November). A statistical comparative study to demonstrate the merit of day of the year-based models for estimation of horizontal global solar radiation. *Energy Conversion and Management*, pp. 37-47.
- Knap, W. (2015, 09 7). *KNMI Cabauw Observations*. Retrieved 07 11, 2019, from <http://projects.knmi.nl/cabauw/bsrn/>
- Knap, W. (2022, 02 03). *Basic and other measurements of radiation at station Cabauw (2005-02 et seq)*. Retrieved from PANGAEA: <https://doi.org/10.1594/PANGAEA.940531>
- KNMI. (2009, 7 21). *KNMI - Daggegevens van het weer in Nederland*. Retrieved 10 09, 2020, from projects.knmi.nl/klimatologie/daggegevens/index.cgi
- KNMI. (2013, 4). *Klimaatdata en -advies, Metadata KNMI-stations, Deelen (06275)*. Retrieved 8 30, 2019, from <http://projects.knmi.nl/klimatologie/metadata/deelen.html>
- Kreuwel, F. (2022, 11 30). *Inaccuracies Meteorology Congestion Management*. doi:10.5281/zenodo.7382724
- Kreuwel, F. (2022, 02 18). *LES simulation of clouds and radiation for 2016-07-16, at Cabauw, NL [29x29km²]*. Retrieved from Vimeo: <https://vimeo.com/679111602>
- Kreuwel, F., Knap, W. H., Visser, L. R., van Sark, W. G., de Arellano, J. V., & van Heerwaarden, C. C. (2020). Analysis of high frequency photovoltaic solar energy fluctuations. *Solar Energy*, 381-389.
- Kreuwel, F., & van Heerwaarden, C. (2022, 3 1). *Data of manuscript "Forecasting day-ahead 1-minute irradiance variability from Numerical Weather Predictions" submitted to Solar Energy*. Retrieved from Zenodo: <https://zenodo.org/record/6320613#.YrBafaJBxPZ>
- Kreuwel, F., Knap, W., Visser, L., van Sark, W., Vilà-Guerau de Arellano, J., & van Heerwaarden, C. (2020). Analysis of high frequency photovoltaic solar energy fluctuations. *Solar Energy*, 381-389.

References

- Kreuwel, F., Mol, W., Vilà-Guerau de Arellano, J., & van Heerwaarden, C. (2021). Characterizing solar PV grid overvoltages by data blending advanced metering infrastructure with meteorology. *Solar Energy*, 312-320.
- Lamer, K., & Kollias, P. (2015). Observations of fair-weather cumuli over land: Dynamical factors controlling cloud size and cover. *Geophysical Research Letters*, 8693-8701.
- Landelius, T., Lindskog, M., Körnich, H., & Andersson, S. (2018). Short-range solar radiation forecasts over Sweden. *Adv. Sci. Res.*, 39-44.
- Langer, L., & Volling, T. (2020). An optimal home energy management system for modulating heat pumps and photovoltaic systems. *Applied Energy*, 115661.
- Larson, V. (2013). Chapter 12 - Forecasting Solar Irradiance with Numerical Weather Prediction Models. In V. Larson, *Solar Energy Forecasting and Resource Assessment* (pp. 299-318). Academic Press.
- Lau, N.-C., & Crane, M. (1997, Dec 1). Comparing Satellite and Surface Observations of Cloud Patterns in Synoptic-Scale Circulation Systems. *Monthly Weather Review*, pp. 3172–3189.
- LEM. (2014, 7 18). *lem rt 500*. Retrieved 9 4, 2019, from https://www.lem.com/sites/default/files/products_datasheets/rt_500.pdf
- Liander N.V. (2021, 12 9). *20211209 Vooraankondiging verwachte congestie verdeelstation Hallum v1.9*. Retrieved from Liander N.V.: <https://www.liander.nl/sites/default/files/20211209%20Vooraankondiging%20verwachte%20congestie%20verdeelstation%20Hallum%20v1.9.pdf>
- Liu, X., Zhang, Z., & Song, Z. (2020). A comparative study of the data-driven day-ahead hourly provincial load forecasting methods: From classical data mining to deep learning. *Renewable and Sustainable Energy Reviews*, p. 109632.
- Lohmann, G. (2018). Irradiance Variability Quantification and Small-Scale Averaging in Space and Time: A Short Review. *Atmosphere*, 9(7), 264-286.
- Lorenzo, A., Holmgren, W., & Cronin, A. (2015). Irradiance forecasts based on an irradiance monitoring network, cloud motion, and spatial averaging. *Solar Energy*(122), 1158-1169.
- Lundberg, S., & Lee, S. (2017). A Unified Approach to Interpreting Model Predictions. *Advances in Neural Information Processing Systems*.
- Lundberg, S., Erion, G., Chen, H., DeGrave, A., Prutkin, J., Nair, B., . . . Bansal, N. L. (2020). From local explanations to global understanding with explainable AI for trees. *Nature Machine Intelligence*, 56-67.
- Luo, K., & Shi, W. (2020). Comparison of Voltage COnTrol by Inverters for Improving the PV Penetration in Low Voltage Networks. *IEEE Access*, 161488-161497.
- Mahesh, B. (2020). Machine learning algorithms-a review. *International Journal of Science and Research*, pp. 381-386.

- Marcos, J., Marroyo, L., Lorenzo, E., D. Alvira, & Izco, E. (2011). From irradiance to output power fluctuations: the PV plant as a low pass filter. *Progress in Photovoltaics: Research and Applications*, 19(5), 505-510.
- Marquez, R., & Coimbra, C. (2013). Intra-hour DNI forecasting based on cloud tracking image analysis. *Solar Energy*(91), 327-336.
- Marty, C., & Philipona, R. (2000, September 1). The clear-sky index to separate clear-sky from cloudy-sky situations in climate research. *Geophysical Research Letters*, pp. 2649-2652.
- Mathijssen, T., Bijma, J., & Knap, W. (2018). *Traceability of CM-11 pyranometer calibrations at KNMI*. De Bilt: Royal Netherlands Meteorological Institute (KNMI).
- Matsukawa, H., Koshiishi, K., Koizumi, H., Kurokawa, K., Hamada, M., & Bo, L. (2003). Dynamic evaluation of maximum power point tracking operation with PV array simulator. *Solar energy materials and solar cells*, 537-546.
- Miller, S., Rogers, M., Haynes, J., Sengupta, M., & Heidinger, A. (2018). Short-term solar irradiance forecasting via satellite/model coupling. *Solar Energy*(168), 102-117.
- Mills, A., Ahlstrom, M., Brower, M., Ellis, A., George, R., Hoff, T., & Kroposki, B. (2011). Dark Shadows. *IEEE Power and Energy Magazine*, 33-41.
- Mohammed, A., & Aung, Z. (2016). Ensemble learning approach for probabilistic forecasting of solar power generation. *Energies*.
- Mol, W., Stratum, B. v., Knap, W., & Heerwaarden, C. v. (2022). *Reconciling observations of solar irradiance variability with cloud size distributions*. arXiv. doi:10.48550/ARXIV.2209.10284
- NEDU. (2022, 09 14). *Verbruiksprofielen*. Retrieved 10 15, 2020, from <https://www.nedu.nl/documenten/verbruiksprofielen/>
- Neggers, R. A., Jonker, H. J., & Siebesma, A. P. (2003). Size Statistics of Cumulus Cloud Populations in Large-Eddy Simulations. *Journal of Atmospheric Sciences*, 1060-1074.
- Netbeheer Nederland. (2021, 07 15). *Hoe is de kwaliteit van energiemeters gewaarborgd?* Retrieved from Slimme Meter: https://www.netbeheernederland.nl/_upload/Files/Slimme_meter_15_4b03da07a4.docx
- Netcode elektriciteit, Artikel 13.12*. (2022, 11 18). Retrieved from Netcode elektriciteit: Artikel 13.12 Netcode elektriciteit
- Nie, Y., Sun, Y., Chen, Y., Orsini, R., & Brandt, A. (2020). Pv power output prediction from sky images using convolutional neural network: the comparison of sky-condition-specific sub-models and an end-to-end model. *J. Renew. Sustain. Energy*.

References

- Nielsen, K., & Gleeson, E. (2018). Using Shortwave Radiation to Evaluate the HARMONIE-AROME Weather Model. *Atmosphere*, 163.
- OpenSTEF. (2022, 9 14). *Github.com/openstef*. Retrieved from `Openstef/apply_features.py` at `main`: https://github.com/OpenSTEF/openstef/blob/main/openstef/feature_engineering/apply_features.py
- OpenSTEF. (2022, 09 14). *openstef/train_create_forecast_backtest.py at main*. Retrieved from `OpenSTEF/openstef`: https://github.com/OpenSTEF/openstef/blob/main/openstef/pipeline/train_create_forecast_backtest.py
- Pedregosa, F., Varoquaux, G., Gramfort, A., Michel, V., Thirion, B., Grisel, O., . . . Duchesnay, E. (2013). Scikit-learn: Machine Learning in Python. *Journal of Machine Learning Research*, 108-122.
- Pelland, S., Galanis, G., & Kallos, G. (2013). Solar and photovoltaic forecasting through post-processing of the Global Environmental Multiscale numerical weather prediction model. *Progress in Photovoltaics*, pp. 284-296.
- Peng, Y., Wang, Y., Lu, X., Li, H., Shi, D., Wang, Z., & Li, J. (2019). Short-term Load Forecasting at Different Aggregation Levels with Predictability Analysis. *IEEE Innovative Smart Grid Technologies - Asia (ISGT Asia)* (pp. 3385-3390). IEEE.
- Pereira, S., Canhoto, P., Salgado, R., & JoãoCosta, M. (2019). Development of an ANN based corrective algorithm of the operational ECMWF global horizontal irradiation forecasts. *Solar Energy*, 387-405.
- Perez, R., David, M., Hoff, T. E., Jamaly, M., Kivalov, S., & Kleissl, J. (2015). Spatial and temporal variability of solar energy. *Foundations*, 1-44.
- Pincus, R., Mlawer, E., & Delamere, J. (2019). Balancing Accuracy, Efficiency, and Flexibility in Radiation Calculations for Dynamical Models. *Journal of Advances in Modeling Earth Systems*, 3074-3089.
- Riihimaki, L., Li, X., Hou, Z., & Berg, L. (2021). Improving prediction of surface solar irradiance variability by integrating observed cloud characteristics and machine learning. *Solar Energy*, 275-285.
- Rodríguez, F., Fleetwood, A., Galarza, A., & Fontána, L. (2018, October). Predicting solar energy generation through artificial neural networks using weather forecasts for microgrid control. *Renewable Energy*, pp. 855-864.
- Roebeling, R., Feijt, A., & Stammes, P. (2006). Cloud property retrievals for climate monitoring: Implications of differences between Spinning Enhanced Visible and Infrared Imager (SEVIRI) on Meteosat-8 and Advanced Very High Resolution Radiometer (AVHRR) on NOAA-17. *Journal of geophysical Research*, 148-227.
- Sánchez, C. J. (2022). Evaluation of HARMONIE-AROME cycle 43h2. 1 at AEMET.

- Schalkwijk, J., Jonker, H., Siebesma, A., & Bosveld, F. (2015, March 1). A Year-Long Large-Eddy Simulation of the Weather over Cabauw: An Overview. *Monthly Weather Review*, pp. 828–844.
- Schittekatte, T., & Meeus, L. (2020). Flexibility markets: Q&A with project pioneers. *Utilities Policy*, p. 101017.
- Seifert, A., & Beheng, K. (2006). A two-moment cloud microphysics parameterization for mixed-phase clouds. Part 1: Model description. *Meteorology and Atmospheric Physics*, 45-66.
- Shah, R., Mithulananthan, N., Bansal, R., & Ramachandaramurthy, V. (2015). A review of key power system stability challenges for large-scale PV integration. *Renewable and Sustainable Energy Reviews*, 1423-1436.
- Sharma, V., Aziz, S., Haque, M., & Kauschke, T. (2020). Effects of high solar photovoltaic penetration on distribution feeders and the economic impact. *Renewable and Sustainable Energy Reviews*.
- STAATSCOURANT. (2022, 5 3). Besluit inzake de verklaring omtrent gedragscode Slim Netbeheer van Vereniging Netbeheer Nederland. *STAATSCOURANT*, pp. z2021-00382.
- Stein, J., Hansen, C., & Reno, M. (2012). *The variability index: a new and novel metric for quantifying irradiance and pv output variability*. Sandia National Laboratories.
- Stein, J., Hansen, C., & Reno, M. J. (2012). The variability index: a new and novel metric for quantifying irradiance and pv output variability. No. SAND2012-2088C.
- Student. (1908). The Probable Error of a Mean. *Biometrika*, 1-25.
- Swain, P., & Hauska, H. (1977). The decision tree classifier: Design and potential. *IEEE Transactions on Geoscience Electronics*, pp. 142-147.
- Tan, Y. T., & Kirschen, D. S. (2007). Impact on the Power System of a Large Penetration of Photovoltaic Generation. *IEEE Power Engineering Society General Meeting*, (pp. 1-8). Tampa, FL.
- U.S. International Trade Commission. (2014, 06). *Global Market for Smart Electricity Meters: Government Policies Driving Strong Growth*. Opgeroepen op 08 26, 2020, van https://www.usitc.gov/publications/332/id-037smart_meters_final.pdf
- Upp Energy. (2013). Retrieved 07 05, 2019, from <http://www.uppenergy.nl/product/details/1f>
- van Heerwaarden, C., Stratum, B., Heus, T., Gibbs, J., Fedorovich, E., & Mellado, J. (2017). MicroHH 1.0: a computational fluid dynamics code for direct numerical simulation and large-eddy simulation of atmospheric boundary layer flows. *Geoscientific Model Development*, 3145-3165.

References

- Vannitsem, S., Wilks, D., & Messner, J. (2019). *Statistical Postprocessing of Ensemble Forecasts*. Elsevier.
- Vasquez, J., Mastromauro, R., Guerrero, J., & Liserre, M. (2009). Voltage support provided by a droop-controlled multifunctional inverter. *IEEE Transactions on Industrial Electronics*, 4510 - 4519.
- Veerman, M., Pedruzo-Bagazgoitia, X., Jakub, F., Vilà-Guerau de Arellano, J., & van Heerwaarden, C. C. (2020). Three-Dimensional Radiative Effects By Shallow Cumulus Clouds on Dynamic Heterogeneities Over a Vegetated Surface. *Journal of Advances in Modeling Earth Systems*, 1924-2466.
- Vergara, P. P., Salazar, M., Mai, T., Nguyen, P., & Slootweg, H. (2020). A comprehensive assessment of PV inverters operating with droop control for overvoltage mitigation in LV distribution networks. *Renewable Energy*, 172-183.
- Virtanen, P., Gommers, R., & Oliphant, T. e. (2020). SciPy 1.0: fundamental algorithms for scientific computing in Python. *Nat Methods*, pp. 261–272.
- Voyant, C., Motte, F., Notton, G., Foulloy, A., Nivet, M., & Duchaud, J. (2018). Prediction intervals for global solar irradiation forecasting using regression trees methods. *Renewable Energy*, 332-340.
- Voyant, C., Notton, G., Kalogirou, S., Nivet, M., Paoli, C., Motte, F., & Foulloy, A. (2017). Machine learning methods for solar radiation forecasting: A review. *Renewable Energy*, pp. 569-582.
- Westering, W., & Hellendoorn, H. (2020). Low voltage power grid congestion reduction using a community battery: Design principles, control and experimental validation. *International Journal of Electrical Power & Energy Systems*, p. 105349.
- World Meteorological Organization. (2016). *International Pyrheliometer Comparison (IPC-XII) (28 September - 16 October 2015; Davos, Switzerland)*. WMO.
- Zarco, P., & Expósito, A. (2000). Power system parameter estimation: a survey. *IEEE Transactions on Power Systems*, 216-222.

Acknowledgements

Thank you for reading my entire thesis and making it to the end! Or if you skipped (immediately) to this part, that must mean you were important in making my PhD project a success and/or a joyful experience. Should you not find your name on these pages, know that it is in my hearth nonetheless.

Chiel, heel erg bedankt voor je geweldige steun tijdens mijn PhD. Met vragen kon ik altijd bij je terecht en met ideeën hielp je deze beter te maken. Je stelde me in staat deze naar een hoger niveau te tillen. Ook buiten dit project heb ik veel plezier van wat ik hierbij van je heb geleerd tijdens onze samenwerking. Trots en blij kijk ik terug op hoe we samen het hele traject van idee, naar aanvraag, naar project, naar thesis hebben doorlopen. Ik kijk benieuwd en vol vertrouwen er naar uit om deze samenwerking voort te zetten.

Jordi, thank you for providing a broad meteorological perspective on my work. You have challenged me to move out of my grid-operator comfort zone and pushed me to build the bridge between disciplines further into meteo territory than I would have dared on my own. You always gave me the feeling of being available when needed, providing concrete and actionable feedback while leaving me in charge of my journey. The perfect second promotor if you'd ask me.

I would like to extend my sincere thanks to **Wouter, Robin, Menno, Martin, Esther, Imme, Sjoerd, Mirjam, Raquel and all other colleagues at the Meteorology and Air Quality department** for providing a warm and welcome environment during my times at the department, keeping to invite me for all social activities and participating in helpful discussions during this 'rollercoaster ride'.

Jan Maarten, bedankt voor het jarenlang intensief met mij willen samenwerken. Kijk met veel plezier terug op onze wetenschappelijke en niet-wetenschappelijke discussies, het samen dingen naar een hoger niveau tillen en praten over alles wat met fermenteren, vergisten en vet te maken heeft. Zou het erg leuk vinden als we dit op een manier voort kunnen zetten. Ook alle anderen die hebben bijgedragen aan het succes en de sfeer van team KorteTermijnPrognoses wil ik ontzettend bedanken: **Frederik, Martijn, Robbert, Bram, David, Jeroen, Bart, Luuk, Jurriaan, Patrick, Guus, Enrico, Charlotte, Maria, Denise, Jonas, Esteban, Marjolein, Ronald, Eireen, Berend, Kasper**. Door jullie heb ik ontzettend veel plezier gehad in mijn werk, en werd de combinatie van Alliander en PhD mij nooit te veel.

Bedankt **Arjan, René en Hiltjo**, dat jullie hebben geholpen ervoor te zorgen dat ik tijdens mijn reguliere werk mijn PhD heb kunnen volbrengen. Waardeer het vertrouwen, de ruimte en de motivatie die jullie mij hierin hebben gegeven enorm.

Hans, Koen, Peter, Mark, Marco, Alex, Fedja, Roy, Aditya, Sander, Petra, Robert-Jan, and all other colleagues of System Operations, thank you for teaching me the ins and outs of the distribution grid and working together towards an autonomous and dynamical energy system.

Bedankt Brabantse Vrienden **Lientje, Daniel, Marijn, Simone, Milou, Fleur, Rianne, Wei-Wei en +1's**, voor jullie interesse, steun en initiatieven om leuke dingen te doen gedurende de afgelopen jaren. En alvast bedankt voor wat jullie ongetwijfeld de komende jaren daarop blijven geven. Ik kijk uit naar de vele Laatstevrijdagen, bachelor(rette) feestjes, BVOT's, bruiloften, babyshowers en promotiefeestjes die nog gaan komen.

Bedankt 'Nijmeegsche' vrienden **Erik, Kim, Bram, Marloes**, voor het samenwonen, tennissen, chillen, dansen, nieuwsjaarsfeesten, helpen verhuizen, *hele klijppen* en nog veel meer. Hoop dat we hier nog lang mee door mogen gaan (NB: qua verhuizen help ik alleen maar mee als mensen dichterbij komen wonen).

Bedankt mannenmaandagmannen **Giel, Martijn, Rik, Stefan en vriendinnetjes van**, voor de (her-)adoptie in de groep. De kook/eet/spelletjes avonden staan als feestjes in mijn agenda. Fijn dat we er voor elkaar kunnen zijn. Ook voor jullie geldt dat ik alleen mee help verhuizen als je dichterbij komt wonen.

Bedankt jongens van **Aquila**, voor het aanwakkeren van interesse in andere vakgebieden en onderstrepen van student in PhD-student.

Als klap op de vuurpijl wil ik mijn familie bedanken. **Papa, mama en Carlien**, bedankt voor het zijn van een superfijn gezin en stabiele basis in Schijndel waar ik weet dat ik altijd terecht kan. Jullie zorgden voor een veilige omgeving om in op te groeien, stimuleerden mijn nieuwsgierigheid en gaven alle ruimte om mijn interesses te volgen. Jullie hebben er voor gezorgd dat voor mij ontzettend veel niet-vanzelfsprekende dingen wel vanzelfsprekend voelen.

En in het bijzonder **Esmee**, voor alle liefde en aandacht die je me afgelopen jaren hebt gegeven. Hand-in-hand heb je mij mijn PhD laten doorlopen en me onderweg op alle leuke dingen geweest. Ben heel blij dat dit boekje af is, en tegelijkertijd dankbaar dat het slechts een hoofdstuk is in het boek van ons.



*Netherlands Research School for the
Socio-Economic and Natural Sciences of the Environment*

D I P L O M A

for specialised PhD training

The Netherlands research school for the
Socio-Economic and Natural Sciences of the Environment
(SENSE) declares that


Frank Peter Maria Kreuwel

born on 2nd December 1991 in Rheden, Netherlands

has successfully fulfilled all requirements of the
educational PhD programme of SENSE.

Wageningen, 11 April 2023

Chair of the SENSE board



Prof. dr. Martin Wassen

The SENSE Director



Prof. Philipp Pattberg

The SENSE Research School has been accredited by the Royal Netherlands Academy of Arts and Sciences (KNAW)



K O N I N K L I J K E N E D E R L A N D S E
A K A D E M I E V A N W E T E N S C H A P P E N



The SENSE Research School declares that Frank Peter Maria Kreuvel has successfully fulfilled all requirements of the educational PhD programme of SENSE with a work load of 40.4 EC, including the following activities:

SENSE PhD Courses

- o Environmental research in context (2019)
- o Research in context activity: 'Opensourcing Short Term Forecasting' (2022)

Other PhD and Advanced MSc Courses

- o Advanced Analytics, Micompany (2019)
- o Scientific publishing, Wageningen Graduate Schools (2019)
- o Statistical Uncertainty Analysis of Dynamic Models, PE&RC and WIMEK (2022)

Management and Didactic Skills Training

- o Chairman Technical Steering Committee OpenSTEF, Linux Foundation Energy (2022-)
- o AI workshop for professionals – development and hosting (2019-2022)
- o Organising a stakeholder workshop – Irradiance variability for the distribution grid operator (2019)
- o Organising a stakeholder workshop – Forecasting for the distribution grid operator (2021)
- o Supervising two BSc students (2020) and three MSc students (2020-2021) with thesis
- o Leadership training, in company training by Phoenix University (2022)

Oral Presentations

- o *Energy Forecasting*. ETIP-SNET, 11-12 October 2018, Brussels, Belgium
- o *Sunlight under the microscope*. Alliander Technische Dag. 13 February 2020, Ede, The Netherlands
- o *Operational Short Term Forecasting*. Smartgrid forums – AI/ML, 9 September 2020, London, United Kingdom
- o *Forecasting the energy grid*. AI ML Innovate, 23 March 2022, Nijmegen, The Netherlands

SENSE coordinator PhD education

Dr. ir. Peter Vermeulen

The research described in this thesis is part of the research programme 'Industrial Doctorates' with project number NWA.ID.17.051, which is financed by the Dutch Research Council (NWO), Alliander N.V. and Wageningen University & Research.

Financial support from Wageningen University for printing this thesis is gratefully acknowledged.

Cover design by Frank Kreuwel using AI (GPT-3), based on the description:

"A painting in the style of Jacob van Ruisdael of scientists studying clouds and sunshine"

Printed by proefschriftmaken.nl

